Mechanisms of Radiation Embrittlement of Nuclear Reactor Pressure Vessel Steels

（和訳　原子炉圧力容器鋼材の照射脆化機構）

Takeo IWAI

岩井　岳夫

(1)

Mechanisms of Radiation Embrittlement of Nuclear Reactor Pressure Vessel Steels

（和訳　原子炉圧力容器鋼材の照射脆化機構）

Takeo IWAI

岩井　岳夫

Contents

ABSTRACT

Radiation embrittlement of nuclear reactor pressure vessel steels may lead to brittle fracture of pressure vessels under severe conditions like pressurized thermal shock events. This problem dominates the reactor safety and the plant life, therefore precise estimation and prediction of radiation embrittlement is necessary for keeping the safety and evaluating the plant life. Although empirical methods have been employed for the evaluation and the prediction of embrittlement, advanced methods based on physical understandings about embrittlement mechanisms are required because of the need to predict embrittlement in the extended plant life where no empirical data are available from the view of the plant life extension. It needs further understandings about embrittlement mechanisms, and this thesis is written with the intention of contributing to the further understandings and developing a new method to approach the embrittlement mechanisms. In chapter 1, these backgrounds and the objectives of this study are described in some details containing the brief explanation of radiation embrittlement of nuclear reactor pressure vessel steels, problems for plant life extension, current understandings of the embrittlement mechanisms, and basic modeling methods for radiation embrittlement.

The radiation embrittlement is believed to result from formation of fine features in matrix that impede dislocation motion. The fine features are so small (several nm or below) that sensitive detection techniques for the features are required. Positron annihilation technique has advantage in high sensitivity for detecting vacancy type defects. In chapter 2, the variable energy monoenergetic positron beam technique is successfully applied to ion irradiated iron based model alloys to investigate vacancy cluster formation by ion irradiation and effect of additional elements on the formation.

It is essential to know how microstructural features cause hardening, and the hardening trend and the thermal recovery behavior are expected to provide information on microstructural features that cause the hardening. In chapter 3, the hardening trend and the thermal recovery behavior are obtained for ion irradiated model alloys. They are

compared with the positron annihilation results and the transmission electron microscopy observation.

In chapter 4, the nature of the hardening features that form under ion irradiation in the model alloys is discussed. It is also discussed how the evolution of the features is modeled and how the obtained understandings for the ion irradiated model alloys are applied to the neutron irradiated practical steels. Then this thesis is concluded in chapter 5.

1. Introduction

1-1 Radiation embrittlement of nuclear reactor pressure vessel steels

1-1-1 Profile of Pressure Vessels

The reactor pressure vessel (RPV) of the light water reactor (LWR) confines a reactor core in pressurized water (Pressurized Water Reactor: 150-160kg/cm^2, Boiling Water Reactor: 70-72kg/cm^2) at high temperature (typically 290 °C). Examples of the pressure vessels are shown in fig.1-1 (PWR) and fig.1-2 (BWR) [1-1]. Technical features of the RPVs are 1) large dimension and thickness, 2) openable top for the exchange of fuel assemblies, and 3) large nozzles. Comparison of their dimension is shown in fig.1-3 [1-1]. The typical dimensions of the RPVs are in the following; the height is about 12 m (PWR) and 18 m (BWR), and the inner diameter is about 4 m (PWR) and 6 m (BWR). The required thickness for such a large dimension of the RPVs is as much as 20 cm (PWR) and 15 cm (BWR). The RPV cannot be exchanged and is the most important component which needs absolute integrity throughout the plant life, because it is the last barrier against the defense in depth for the reactor safety. Fracture of the RPVs leads to the most severe accident like a loss of coolant accident or release of fission products to the air. This concern with safety is exemplified by the attention devoted to design, materials selection, fabrication, inspection, overall quality assurance and continuing in-service inspection for each RPV. Continuous improvements have been carried out to get the absolute integrity on the whole aspects. For example, early pressure vessels were made of rolled plates as a whole and they required weldment even around the core region (fig.1-4) [1-2]. However due to the significant development of the steel fabrication processes, ring forgings have been used around the core region for the recent RPVs to reduce the welded parts since 1970's (fig.1-5) [1-2].

1-1-2 Pressure Vessel Steels (Chemical Composition, Heat Treatment, Microstructure)

Materials for the RPVs must have sufficient toughness in any possible conditions. Si-Mn low alloy steels such as A212B were used as the pressure vessel steels of early LWRs. Then, Mo-added steels such as A302B Mn-Mo low alloy steels were used for the improvement of the strength at high temperature. As reactors had become larger, the

fracture toughness of A302B became insufficient. Then nickel was added to A302B steels. However, reactors became even larger, and the toughness of the improved A302B became insufficient again. The heat treatment of the steels was improved from normalizing - tempering to quenching - tempering. This kind of steels is called A533B, and it is now used as the RPV steel most generally in the West. The A533B plate shows bainitic structure, but the steels for the RPVs generally have large varieties of microstructure between weld, heat affected zone (HAZ), and plate/forgings [1-1, 1-3, 1-4]. In Eastern Europe and Russia different kinds of steels are used for the VVER type reactors and the major difference exists in the addition of Cr and V to the VVER type steels [1-1, 1-3]. Table-1.1 shows the typical steel composition for the Western and Eastern types of the RPVs [1-3].

Table 1-1. Typical steel composition [a] (wt.%) from various studies [1-3].

	C	Mn	Si	P	S	Ni	Cr	Mo	Cu	V
VVER										
15Ch2MFA	0.18	0.6	0.37	0.025	0.025	0.4	3.0	0.8	0.15	0.35
15Ch2NMFA grade AA	0.17	0.5	0.28	0.009	0.011	1.26	2.1	0.58	0.04	0.08
BWR/PWR										
A533B	0.2	1.37	0.24	0.007	0.006	0.62	0.14	0.53	0.07	_
A302B	0.24	1.34	0.23	0.011	0.023	0.18	0.11	0.51	0.1	_

a) Balance Fe.

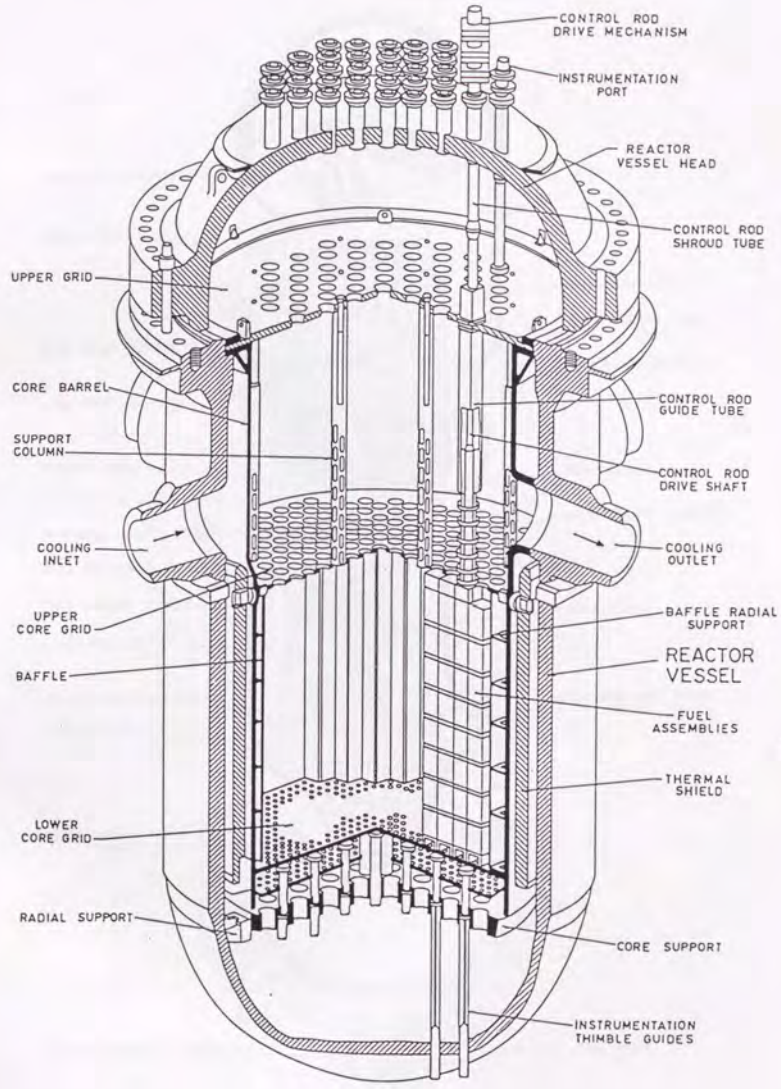

Fig.1-1 An example of reactor pressure vessel for PWR [1-1]

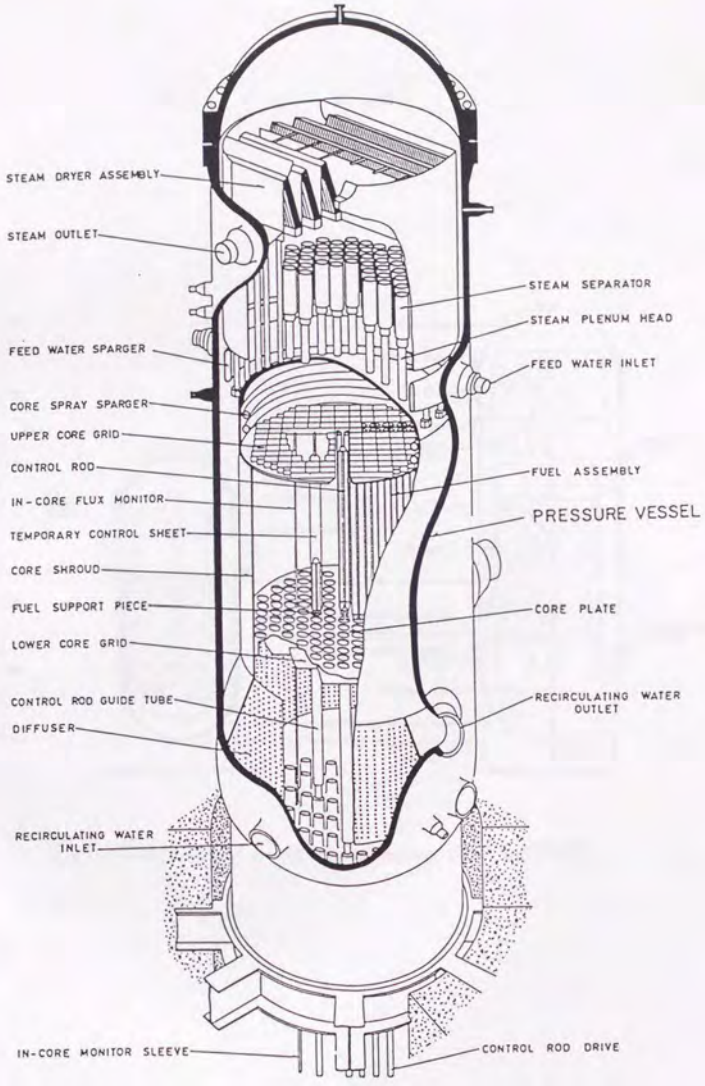

Fig.1-2 An example of reactor pressure vessel for BWR [1-1]

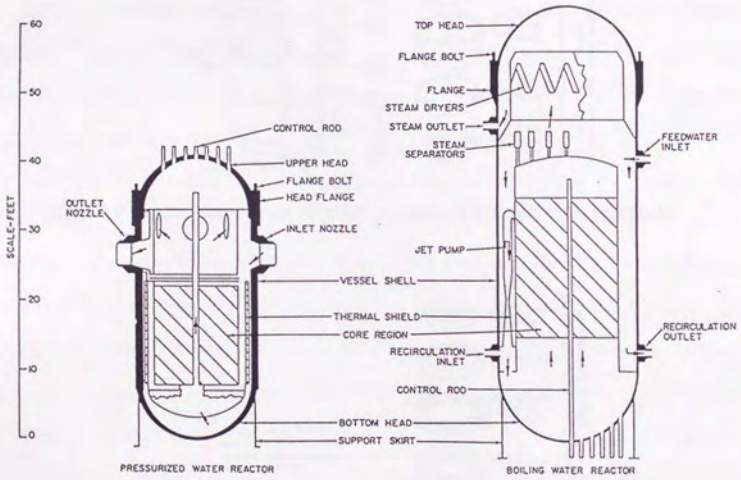

Fig.1-3 Comparison of the dimension between PWR and BWR [1-1]

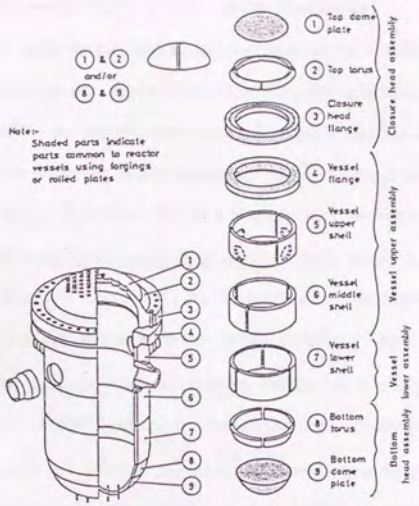

Fig.1-4 Pressure vessel made of rolled plates for PWR and each part [1-2].

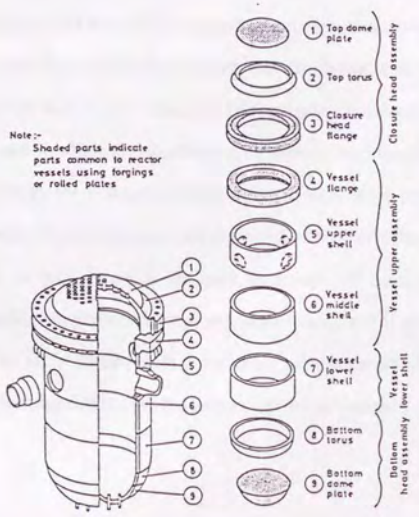

Fig.1-5 Pressure vessel made of forgings for PWR and each part [1-2].

1-1-3 Radiation Embrittlement of Pressure Vessel and its Monitoring

Aging of the RPVs, in particular, degradation of toughness of the RPV steels is one of the most critical problems on the reactor safety. Since the degradation is mainly due to neutron exposure to the RPV, the phenomenon is called radiation embrittlement of RPV.

The requirements for avoiding brittle fracture of the RPVs from the deterministic fracture mechanics are $K_{IC} \geq K_I$ where K_{IC} is a fracture toughness and K_I is a stress intensity factor, and sufficiently large upper shelf energy (USE), which is measured with Charpy V-notch impact test. The K_{IC} and K_I are functions of temperature, therefore it is necessary for avoiding brittle fracture to keep the condition of $K_{IC} > K_I$ over the possible temperature range for the pressure vessels. Neutron irradiation to the pressure vessel steels shift the K_{IC} curve to higher temperature, and the shift in temperature of the curve is generally evaluated from the shift in nil-ductility transition temperature (NDTT) measured with drop weight tests or the shift in ductile-brittle transition temperature (DBTT) measured with Charpy V-notch impact tests. Figure 1-6 shows the above concept schematically. Therefore, it is necessary for the judgment of the RPV integrity to evaluate precisely the shift in NDTT or DBTT caused by neutron irradiation as well as the possible stress and temperature conditions under the accidental events. Nowadays surveillance test data and prediction formulas derived from statistical analysis of the data on the surveillance test and irradiation experiments in material test reactors (MTR) are complementarily employed for the evaluation of the embrittlement at the present time or in the near future. An example of configuration and direction of the surveillance capsules is shown in fig.1-7 [1-5]. A lead factor is defined as a ratio of neutron flux at the surveillance capsule position to neutron flux at the vessel wall, and it generally ranges from 1.5 to 4 [1-6]. The surveillance data have been accumulated with increasing operating plants enough to form a data base for further statistical analyses.

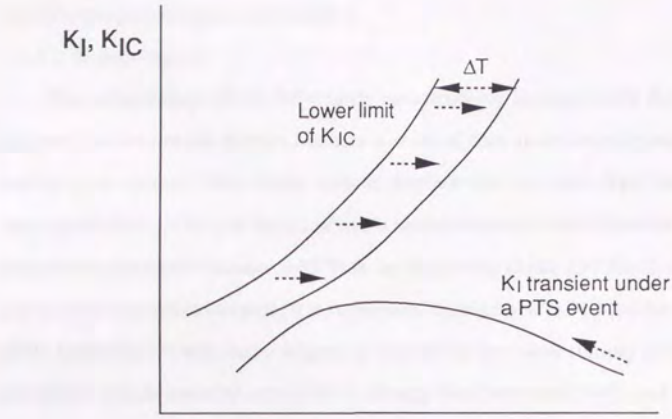

Fig.1-6 A schematic figure of the shift of K_{IC} curve caused by irradiation.

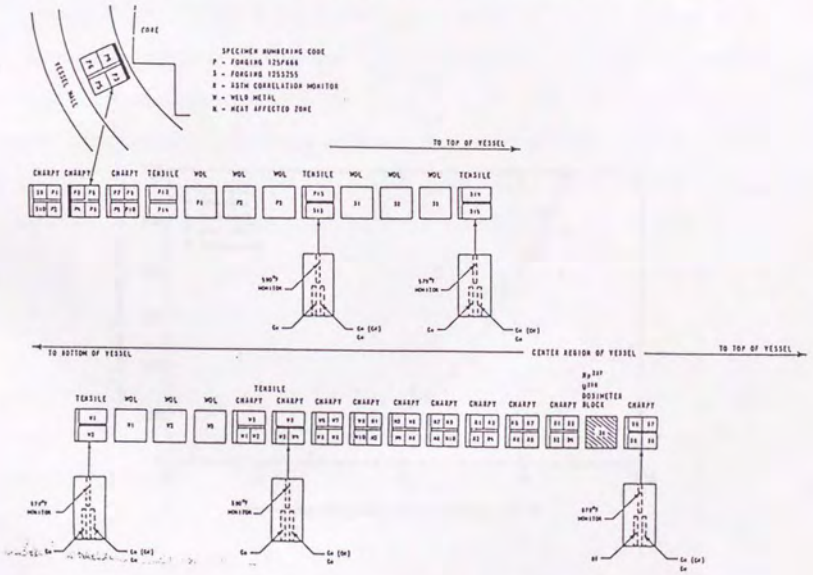

Fig.1-7 An example of configuration and direction of the surveillance capsules [1-5].

1-1-4 Factors controlling the embrittlement

1-1-4-1. Neutron fluence

The embrittlement of the RPV steels monotonously increases with the neutron fluence. The fast neutron fluence has been a scale of dose since the early days of the nuclear power plants. Other scales such as displacement per atom (dpa) have been investigated since 1970s, and the use of dpa is recommended for the estimation of depth dependence of radiation damage in RPVs in the Regulatory Guide 1.99 Rev.2. Based on physico-based model calculation, it was proposed by Heinisch [1-7] from the study of HFIR embrittlement that freely migrating interstitials per atom (fmipa) gives better correlation of embrittlement among HFIR, Omega West Reactor (OWR) and Rotating Target Neutron Source (RTNS-II) than dpa (fig.1-8).

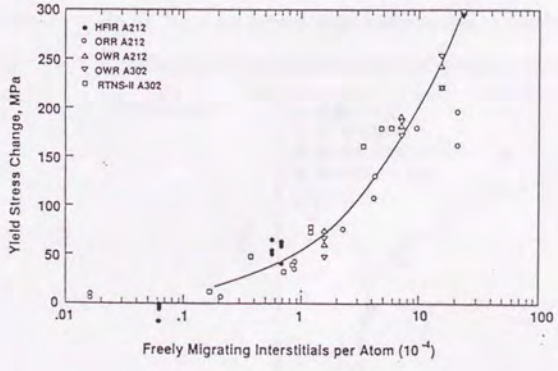

Fig.1-8 Change in 0.2% offset yield stress of A302B and A212B pressure vessel steels as a function of freely migrating interstitials per atom (fmipa) [1-7].

1-1-4-2. Chemical composition of the steels

It has been well-known that the embrittlement of RPV steels is sensitive to their copper content [1-8, 1-9]. Figure 1-9 shows an example of the copper effect [1-8]. However, when the early nuclear reactors were constructed, this fact was unknown to result in the pressure vessel steels containing considerably large amount of the copper (approximately 0.4wt.%). Until 1970's phosphorus was believed to have a great effect on embrittlement. In 1974 American Society for Testing and Materials (ASTM) added the limitation to the copper and phosphorus content of the A533B steels. Now the copper content of the A533B steels is limited to less than 0.1 wt.%.

The nickel content was considered to have little effect on embrittlement until the middle of 1970's, but the effect of nickel content has been realized and it is now adopted to the prediction formula of the embrittlement (Regulatory Guide 1.99 Rev.2). In general nickel is considered to have the combined effect with the copper content [1-10]. But Odette et al. adopted the independent nickel enhancement of the embrittlement to his prediction formula [1-8] (Fig.1-10). It is not clear whether nickel has the independent effect on the embrittlement or not.

The effect of the other elements such as phosphorus or sulfur has appeared to be less important. However, in Japan the effects of phosphorus and silicon have recently been adopted for the prediction of the embrittlement of plates and weld metals, respectively (to be discussed later).

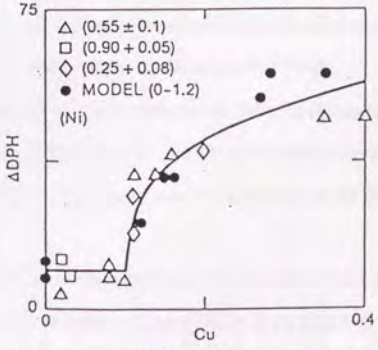

Fig.1-9 The effect of copper on the embrittlement of RPV steels and model alloys. The numbers in the brackets show the nickel content for each symbol [1-8].

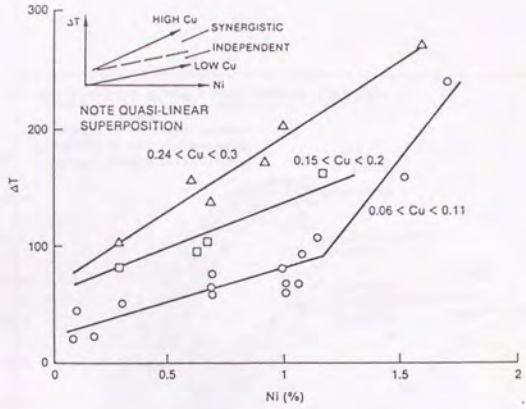

Fig.1-10 The effect of nickel on the embrittlement of RPV steels. [1-8].

1-1-4-3. Microstructure

The microstructure of steels is controlled by their chemical composition and the heat treatment. It is generally said that low temperature transformation structure such as tempered martensite or bainite is more insensitive to neutron irradiation embrittlement than high temperature transformation structure such as ferrite or pearlite [1-6].

With respect to the effect of grain size, it was reported that the embrittlement of steels which consist of larger grains was greater than that of steels which consist of smaller grains [1-11]. However the effect of the grain size is considered to be smaller than that of impurity or microstructure.

Weld and heat affected zone (HAZ) have quite different microstructure from plates. In addition, weld metal have so different amounts of impurities and so different stress conditions from that of plates that DBTT of weld is higher than that of plates before

irradiation, and that increase of DBTT caused by neutron irradiation for weld was larger than that for plates (fig.1-11) [1-12].

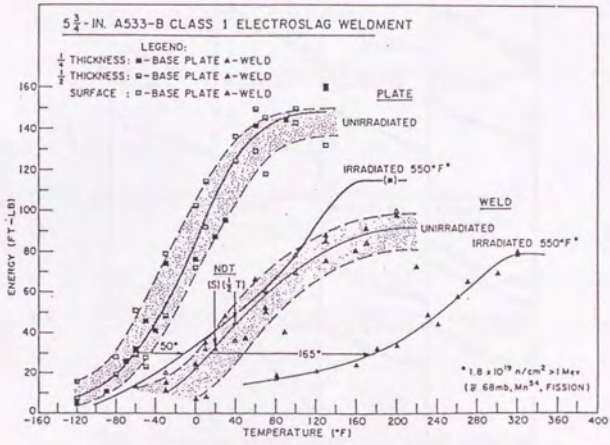

Fig.1-11 A comparison between radiation-induced change of Charpy curves for plate and weld [1-12].

1-1-4-4. Irradiation temperature

The effect of irradiation temperature on the embrittlement is considerably great (Fig.1-7). The embrittlement decreases with increasing irradiation temperature, and this fact suggests that thermal recovery of radiation-induced defects occurs during irradiation.

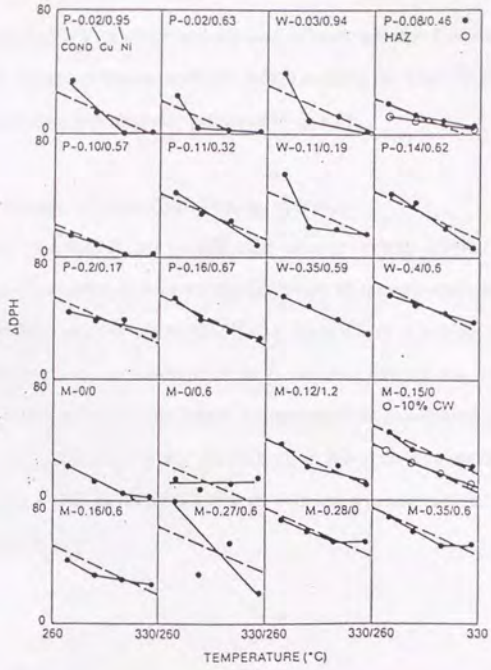

Fig.1-12 Variation of hardness change with irradiation temperature (P: plate, W: weld, M: model alloy and CW: cold-worked) [1-8].

1-1-4-5. Neutron flux

Neutron flux was considered to have little effect on embrittlement in the early days of the embrittlement study, but the effect has been gradually recognized. The general theory of the dose rate effect proposed by Kiritani [1-13] is the following; if the reaction rate R for a particular reaction can be expressed as a function of flux Ø in the form of $R = K\emptyset^n$, the reaction is enhanced by accelerated irradiation in the case of $n > 1$, unchanged in the case of $n = 1$, and suppressed in the case of $n < 1$. Since the radiation embrittlement of RPV steels results from multiple radiation-induced reactions, its dose rate dependence might not be expressed as such a simple form. The embrittlement of

RPV steels in practical LWRs which are exposed to lower neutron flux than MTRs tend to saturate [1-6]. Some prediction methods which include the flux effect on radiation enhanced diffusion have been recently proposed [1-8, 1-9].

1-1-4-6. Primary Knock-on Atom (PKA) energy spectrum

Since PKA spectrum is not so different among various LWRs, PKA energy spectrum had been less pronounced until the discovery of the extraordinary accelerated embrittlement of HFIR reactor vessel [1-14] (fig.1-13) which is subject to neutrons of much larger thermal - fast flux ratio than LWRs. It was once thought that the difference in PKA energy spectrum is the most probable interpretation of accelerated embrittlement. However, it became clear recently that the thermal to fast ratio was overestimated, and atomic displacement by the gamma field of very high energy is considered as the current interpretation of the discrepancy.

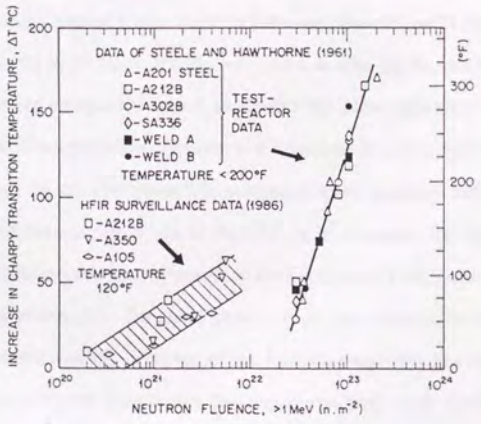

Fig. 1-13 Accelerated radiation embrittlement of HFIR reactor vessel [1-14].

1-2 Problems for Plant Life Extension

1-2-1 Needs for Plant Life Extension

Demand of electric power is getting larger and it will continue growing all over the world. Therefore nuclear power is expected to supply more electricity than ever because of the limit of the fossil fuels and their CO_2 problem. However, construction of nuclear power plants is globally getting more difficult due to the anxiety of the public for such serious accidents like TMI or Chernobyl so that the annual number of newly constructed plants is decreasing. It may result in the shortage of electric power when many nuclear power plants reach their operation limit and shut down. Therefore it is important to utilize the existing plants as long as possible from the view of the global energy problem.

Operation limit of a nuclear power plant varies among the countries. In US, licensing limit of operation of nuclear power plants has been defined as forty years. This licensing limit will come in the near future for the plants which have been in service since 1960's. Several years before power plants reach the licensing limit, power companies have to make decision among following three ways; 1) shutdown and decommission of the reactor, 2) construction of a new plant to substitute the old, or 3) extension of the operation period in 10 to 20 years. It costs very much to take the former two ways, so it is natural that power companies intend to extend the plant operation with keeping sufficient integrity. Thus, plant life extension is also needed from the view of economy.

It is needless to say that plant life extension must be done with keeping the sufficient safety of nuclear power plants. In USA, it is necessary for the extension of service life of nuclear power plants to convince the Regulatory Authorities and the public of the plant safety thoroughly. For some plants which have been in service for a long time, precise evaluation of the decrease of the fracture toughness has been needed in order to prove the integrity even under the severe accidents such as the pressurized thermal shock events.

Surveillance tests and prediction formulas are currently used complementarily in order to estimate embrittlement of vessels. There are various prediction formulas among countries derived from the statistical analyses of mechanical property data collected

through the surveillance tests and material test reactor irradiations. In the following section, various prediction formulas are shown.

1-2-2 Empirical Methods for Predicting Embrittlement

The prediction formulas of the embrittlement are generally expressed in the form of the product of the chemistry factor and the fluence factor, the former is a function of chemical composition of the steels and the latter is the function of fast neutron fluence. In the following, the embrittlement is expressed as the shift of reference temperature (ΔRT_{NDT}) which is roughly equal to the shift of nil-ductility transition temperature, chemical symbols in formulas are the content of the element in wt.%, and f is the fast neutron fluence in $10^{19} n/cm^2$ (E > 1MeV). These formulas are derived based on statistical analyses of the data from the irradiation experiments in the material test reactor (MTR) and/or from the surveillance tests.

USA

● Regulatory Guide 1.99 Rev.1 (1977)

Regulatory Guide 1.99 Rev.1 was presented by Nuclear Regulatory Committee in US. in 1977. At that time, copper and phosphorus were believed to have the dominant effect on the embrittlement, therefore the chemistry factor was expressed as the function of copper and phosphorus content. The formula is;

$$\Delta RT_{NDT} = [40 + 1000\,(Cu - 0.08) + 5000\,(P - 0.008)]\, f^{0.5}.$$

● Guthrie's formula

The synergistic effect of copper and nickel was adopted to the Guthrie's formula. The effect of phosphorus was not adopted in the formula because of the relative insensitivity of embrittlement to phosphorus content. The formula is;

$$\Delta RT_{NDT} = (-10 + 470Cu + 350CuNi)\, f^{0.270}.$$

This formula was used in 10CFR50.61 published by NRC in 1985.

● Regulatory Guide 1.99 Rev.2 (1988)

Regulatory Guide 1.99 Rev.2 is currently effective in US. This is basically a combination of two correlations given by Guthrie [1-15] and by Odette [1-16]. Its characteristics are (1) the chemistry factor is derived from the table using copper and nickel content, (2) the table is different for plate or weld, (3) the saturation of embrittlement is adopted to the power of f. It is also remarkable that the use of dpa was recommended for the first time for the evaluation of embrittlement in the thick wall. The formula is;

$$\Delta RT_{NDT} = [\text{chemistry factor}]\ f^{0.28-0.10\log f}$$

This formula can be applied in the case of 0.1 to 0.4 wt.% Cu, 0.1 to 1.0 wt.% Ni, fast neutron fluence in the range of $2x10^{18}$ to $10^{19}n/cm^2$ (E>1MeV), neutron flux less than $5x10^{11}n/cm^2$, and irradiation temperature between 280 and 305 °C.

Japan

● JEAC 4201-1991

In Japan, many efforts have been made to develop the vessel material properties and their irradiation sensitivity. It results in the excellent level of Japanese steels, and the prediction formula should reflect such improvement. Then Ishino et al. analyzed the domestic PWR surveillance data, foreign surveillance data, and accelerated irradiation data at test reactors to derive the prediction formulas [1-17]. Moreover, domestic BWR data were added to modify the formula. It is currently utilized as JEAC 4201-1991 and the form is as follows;

$$\Delta RT_{NDT} = \{-16+1210P+215Cu+77CuNi\}f^{0.29-0.04\log f} \quad \text{for plates}$$

$$\Delta RT_{NDT} = \{26-24Si-61Ni+301CuNi\}f^{0.25-0.10\log f} \quad \text{for weld.}$$

It is unique compared with other prediction formulas to consider the effect of silicon for weld.

1-2-3 Problems of empirical methods and Needs for physico-based methods

The integrity of RPVs has ever been ensured with such empirical methods, however, the necessity to ensure the integrity with the methods based on the physical basis has been proposed recently. The background of this concept is shown as follows;

(1) As described in 1-2-1, in US licensing limit of operation is forty years. This limit of license will come in the near future for the plants which have been in service since 1960's. Due to the difficulty of the construction of a new nuclear power plant, plant life extension has been proposed and the necessary R & D has started since 1975. In US it is necessary for the extended service life to convince Regulatory Authorities and the public of the plant safety thoroughly. For some plants which have been in service for a long time, precise evaluation of the decrease of the fracture toughness has been needed in order to prove the integrity even under the severe accident such as pressurized thermal shock events.

(2) In Japan, the current concern is to estimate how long the recent improved materials will have been safely usable in the future. It is necessary for this to accurately predict the limit of the service life for each product based on the mechanisms of the degradation.

(3) Recently, there have been several cases which show difference between the prediction of embrittlement based on the statistical analysis and the measured value. For example, in KRB-A reactor, a BWR at Gundremmingen in Germany, some of the data on embrittlement obtained from trepan specimens taken along specific orientation from the actual RPV were found to be worse than expected from trend curves of evaluation Code [1-18]. Another example is the shift in DBTT of the RPV steels of the High Flux Isotope Reactor (HFIR) at Oak Ridge National Laboratory (ORNL) in US. The surveillance data were found to be greater than those predicted from research reactor irradiation data (fig.1-13). In order to investigate the possible cause for this discrepancy the service of the reactor had to be interrupted for the period of 1986 -1989. These examples evoke needs for the improved prediction methods beyond the empirical methods. Mechanistic modeling which is based on physical insights about the

embrittlement is currently considered as the possible improved prediction method for the radiation embrittlement . The difference between the empirical methods and physico-based methods are schematically shown in fig.1-14.

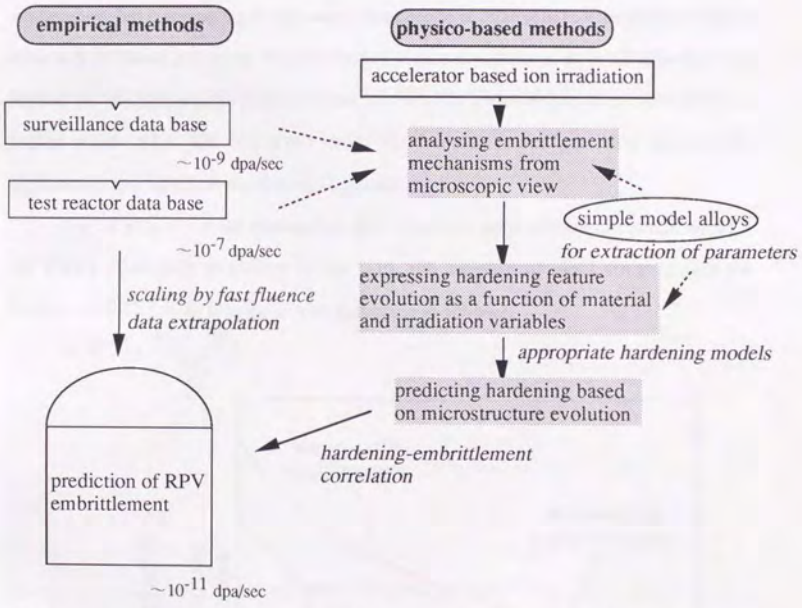

Fig.1-14 Integration of two different approaches to the prediction of RPV embrittlement.

1-3 Current Understandings of the embrittlement mechanisms

1-3-1 Radiation embrittlement and radiation hardening

It is commonly recognized that matrix hardening mainly contributes to the radiation embrittlement of pressure vessel steels. How matrix hardening causes embrittlement is explained in Fig.1-15 [1-19]. Yield stress of body-centered cubic (bcc) metals such as iron has as weak temperature dependence as elastic constant at relatively high temperature, but it has strong temperature dependence at relatively low temperature due to thermally activated processes. The increase of yield stress induced by irradiation does not depend on test temperature in most cases, so the yield stress-temperature curve shifts to higher yield stress. On the other hand, the fracture stress has little temperature dependence and hardly changes due to irradiation.

The temperature at the intersection point between yield stress and fracture stress is the DBTT. Therefore as shown in Fig.1-15, the increase of yield stress causes the increase of DBTT. This relation can be expressed as follows;

$$\Delta DBTT = \frac{\Delta\sigma_y - \Delta\sigma_f}{\frac{d\sigma_y}{dT}}$$

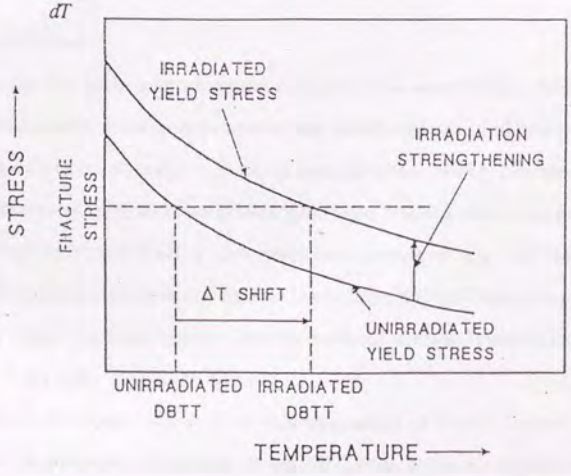

Fig.1-15 Schematic diagram showing how irradiation hardening results in a transition temperature shift [1-19].

where σ_y is yield stress and σ_f is fracture stress. Assuming $\Delta\sigma_f = 0$ and $d\sigma_y/dT$ = constant, ΔDBTT is roughly proportional to $\Delta\sigma_y$. Because the proportionality has been confirmed in some irradiation experiments, radiation embrittlement is considered to result from matrix hardening by irradiation. For example, the proportionality constant is reported to be 0.65 ± 0.15 °C/MPa for weld and 0.5 ± 0.2 °C/MPa for plate in the cases of the RPV steels irradiated in power reactors [1-20].

1-3-2 Hardening mechanisms

Although transmission electron microscopy (TEM) has been generally applied to the investigation of microstructural evolution, there have been little TEM-visible evidences of microstructural evolution in the irradiated RPV steels to which the radiation hardening of pressure vessel steels can be attributed. Therefore the radiation hardening is considered to be due to formation of fine microstructural features below the TEM resolution limit acting as dispersed obstacles to dislocation motion. Hardening models will be discussed later.

1-3-3 Copper rich clusters

Nature of the fine scale microstructural changes is the main interest about the embrittlement mechanisms. Since copper impurity significantly enhances embrittlement at low and intermediate fluences, copper rich precipitates have been widely considered to form during irradiation through radiation enhanced diffusion. Various techniques such as small angle neutron scattering (SANS), atom probe field ion microscopy (APFIM) and field emission gun/scanning transmission electron microscopy (FEG/STEM) indicate the presence of fine copper rich clusters (below 2nm) in irradiated steels and model alloys [1-21, 1-22, 1-23, 1-24, 1-25, 1-26, 1-27, 1-28].

Precipitation of copper atoms from supersaturation of Fe-Cu system was investigated with thermal aging experiments above 500°C from 1960s. A schematic view of thermal aging behavior and the contribution of each factors are shown in fig.1-16 [1-21, 1-22]. Copper precipitates continue growing up to several tens of nm during thermal

aging, and the hardness shows a peak value when the precipitates become 2 ~ 4 nm in diameter. Then the hardness decreases with increasing precipitates' size to show overaging. In the overaged condition with precipitate diameter above 15nm, the structure of precipitates has been found to be fcc that is inherent to copper. Recent high resolution electron microscopy (HREM) indicates the precipitates have twinned 9R structure when their size is within 6 ~ 15 nm [1-29]. Smaller precipitates are coherent with matrix and have been proposed to have bcc structure [1-22].

The precipitation is controlled by diffusion of copper atoms. Since diffusion of copper atoms occurs with vacancy mechanism, supersaturated vacancies introduced by neutron irradiation enhance diffusion to assist the copper precipitation. However, precipitation behavior in the irradiated iron alloys is different from that in the thermally aged alloys. There is no observation that find overaged fcc copper precipitates in the irradiated alloys, instead, they remain at ~ 4 nm diameter in simple alloy systems, which is similar in size of peak hardness condition. Moreover, precipitates in the irradiated materials tend to contain more other elements such as nickel and manganese than in the thermally aged materials. It is not clear why such differences occur between the thermally aged and the irradiated. There are still many problems to be solved on the copper precipitation in the irradiated materials such as nucleation process and effect of displacement cascades on the nucleation, precipitate composition and effect of matrix chemical composition on it, structure or atomic configuration in a precipitate including vacancies, diffusion constant at various vacancy concentrations, effective copper concentration in solid solution, and so on.

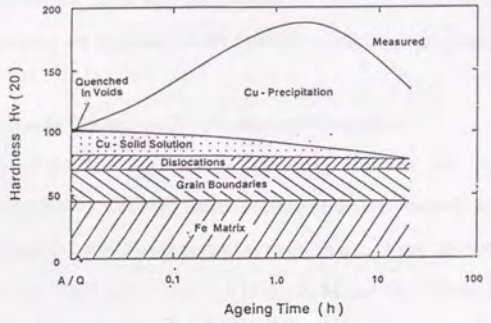

Fig.1-16 The various microstructural components making up the measured hardness response of a Fe-Cu alloy following thermal aging at 550°C [1-21, 1-22].

1-3-4 Matrix defects

There must be the other hardening features than copper rich clusters because the irradiation hardening occurs even in the case of very low copper steels. Such features are generally called "matrix defects", however, the nature of them is not clear. They may be "sponges" (vacancy-rich regions), microvoids, dislocation loops (vacancy or interstitial), or solute-point defect clusters. Although evidence of microvoids and dislocation loops has been observed in the irradiated simple model alloys, TEM technique cannot detect such evidences in complex practical steels irradiated to typical RPV doses.

1-3-5 Nonhardening embrittlement

As discussed above, hardening mainly induces embrittlement in the dose range of the current plant life. However, there might be potential for nonhardening embrittlement

in some RPV materials in the dose range of the extended plant life. Non hardening embrittlement is generally associated with intergranular failure resulting from grain boundary segregation. Elements such as P, S, As, Sn and Sb are known to segregate to the grain boundaries under thermal conditions [1-3]. Irradiation might assist the segregation but there are little data on the irradiation-induced segregation in RPV steels.

1-3-6 Various Special Techniques for the mechanism research

Because of the fine scale of the hardening features, use of various special techniques is required for characterization of microstructural and microchemical features. Phythian and English compiles the techniques available to characterize the microstructure / chemistry of the material in Table 1-2 [1-3]. P, M and G in Table 1-2 represent the availability of each techniques to precipitates, matrix and grain boundaries, respectively. In addition to this table, tomographic APFIM has recently become a powerful method for investigation of precipitates [1-30]. This technique can produce a 3D image of copper precipitates in simple model alloys.

Table 1-2 Techniques available for the characterization of RPV steels [1-3].

Technique application Precipitate, Matrix, Boundary Example references	Information available Limitations/comments
Transmission electron microscopy (TEM) P, (M), B Example refs. [29,30,34,38,40,43,44,45,46,52,59,68, 95,97,104,105,123]	Strain field of small precipitates and defect clusters. Number density, size and structure of features with diameter above the visibility limit of 2 nm. In-situ experiments on dislocation pinning and precipitation kinetics. Standard sample geometry 3 mm diameter 0.05 mm thick discs. Analysis limited to relatively small areas ($\sim mm^2$) less than 0.1–0.5 μm thick. Microchemical information by electron energy dispersive X-ray (EDX) and electron energy loss spectroscopy (EELS). Resolution may be adversely affected by magnetic nature of material or oxide formation on the surface
Field emission gun scanning transmission electron microscopy (FEGSTEM) P, B Example refs. [29,30,34,46,52,104,107,119]	Microchemical information on the spatial distribution of (embrittling) elements, i.e., composition of small precipitates or precipitate free regions of the matrix, and grain boundaries Beam size $\sim$ 1.5 nm, positioned with nm resolution to give P,B elemental composition by (EDX) or (EELS), typically can give concentrations (Cu) above $\sim$ 0.05 wt%
Electron probe micro analysis (EPMA) P, B Example refs. [122,123]	Chemical analysis of the bulk composition by EDX or X-ray wavelength spectroscopy. Sample volume analysed $\sim \mu m^3$. Elemental mapping of bulk composition changes across weld runs, etc. Analysis of inclusions and second phase particles
High resolution electron microscopy (HREM) P, M, B Example refs. [26,27,30]	Lattice imaging thin regions containing precipitates and/or matrix defects such as dislocation loops. Size and structure of the precipitates/defects. Limited to extremely thin samples < 20 nm thick, requires very clean samples, gun damage can be a problem in the identification of lattice defects
Field ion microscopy and 3D atom probe (FIM) (POSAP or OAP) P, M, B Example refs. [29,30,32,59,69,71,91,98,127,130]	Atomic resolution and atomic composition of small regions of the matrix, precipitates and grain boundaries. Very high spacial resolution, chemical composition isotope sensitive, can be both an advantage and a disadvantage. Relatively small volume analysed, typically only $\sim 5\ \mu m^3$
Small angle neutron scattering (SANS) Diffuse elastic neutron scattering (DENS) P, (M) Example refs. [29,30,33,36,37,39,52,62,63,64,65,67, 72,100,101,102,105,126]	Size and number density of precipitates in bulk specimens. Typically 10×10×2 mm. Magnetic A ratio measurements also permit some insight into the chemical composition of the scattering centres. Resolution $\sim$ 1 nm
Anomalous small angle X-Ray scattering (ASAXS) P Example refs. [93,94]	Size and number density of precipitates, elemental specific. Technique similar to SANS but with limited depth penetration
Extended X-Ray absorption fine structure (EXAFS) P Example refs. [30,73,99,125]	Provides data on the average atomic environment of embrittling species such as copper and nickel. Currently limited to simple model alloys as data interpretation difficult in complex steels. Bulk sampling technique

Table 1-2 (continued)

Technique application Precipitate, Matrix, Boundary Example references	Information available Limitations/comments
Positron annihilation (PA) P, M Example refs. [34,55,70,84,89,92,96,100,105,116,117, 128,129]	Lifetime, Doppler broadening and angular correlation techniques. Information on both matrix defects and precipitates. Association of vacancy clusters and contribution of vacancies to the precipitate kinetics. Non destructive bulk sampling technique, samples typically 10×10×2 mm. Full mechanistic understanding currently limited to model alloys, as data interpretation difficult in complex steels. Increasingly being used in an empirical way to correlate with mechanical properties data. Can also be employed in ND testing of plant components
Internal friction (IF) P, M Example refs. [18,29,74,112,113,114]	Low frequency: gaseous impurities C, N and O in or out of solution (Snoek effect). Orientation changes in point defect complexes related to elastic anisotropy. High frequency: dislocation interactions (Granato–Lucke effect)
Mössbauer spectroscopy (MS) P, M Example ref. [54]	Recoiless nuclear resonance absorption of gamma radiation. Bulk analysis technique, average environment of the Mössbauer nucleus. Precipitation of copper, carbon in solution or in carbides. Interpretation difficult in complex steels
Muon spin rotation (μSR) P, M Example ref. [87]	Bulk technique requiring high energy particle accelerator. Point defects, defect clusters and precipitation kinetics followed by changes in depolarisation, commencement of ppt ripening detected by changes in precession frequency. Application to complex steels not fully understood
Barkhausen emission and magneto acoustic emission (BE, MAE) P, M Example refs. [66,38,76,77,78,79,88]	Related nondestructive bulk analysis techniques. Detect interactions between moving magnetic domain walls and pinning points (copper precipitates?). Currently lacks sensitivity in application to RPV steels
Molecular dynamics (MD) P, M, B Example refs. [3,4,13,14,15,30,42,75]	Computer simulation of the atomic interactions in materials. Understanding of the properties and transformation of bcc copper. Used in the study of irradiation-induced defect complexes. Good elemental potentials but currently no realistic Fe alloy potentials as yet available. Limited to small volumes due to computer and memory intensive calculations
Scanning Auger microscopy (SAM) B Example refs. [80,107]	Analysis of the fracture surface providing surface specific microchemical information on embrittling species such as P. In-situ fracture of specimen required to avoid surface contamination
Static/dynamic secondary ion mass spectroscopy (SSIMS/ DSIMS) P, B Example refs. [81,82,83]	Microchemical information on materials provided by spectral analysis of sputtered ions. In principle SSIMS can be used for assessment of segregation to grain boundaries (fracture surface), requires good time-of-flight detector. DSIMS good qualitative elemental mapping, grain boundary segregation on cross section samples. Through thickness composition of large inclusions and precipitates. Diffusion kinetics can be followed due to isotopic sensitivity
Scanning tunnelling microscopy (STM) P, (M) Example refs. [108,109,110]	Surface structural assessment with atomic resolution. May provide information on large overaged precipitates, offers possibility to identify subsurface features by magnetic anomaly when used in conjunction with a magnetic tip. Sensitive to any oxide layer and/or surface contamination giving rise to problems in data interpretation

Table 1-2 (continued)

Technique application Precipitate, Matrix, Boundary Example references	Information available Limitations/comments
Electrical resistivity P, M Example refs. [85,86,103]	Bulk sampling technique used in the assessment of point defect and defect complexes. Interpretation more difficult in the complex steels
Lattice parameter measurements P, M Example refs. [60,124]	Changes in lattice parameter associated with solute additions, precipitates and matrix defects. Requires further work to validate the technique and its application to model alloys and RPV steels
High precision dilatometry/density P, M Example ref. [120]	Accurate assessment of volume changes associated with the production of matrix defects. Currently unknown capability in the area of RPV steels. Considerable data and expertise exists in applying the technique to other systems, i.e., irradiation induced growth and void swelling
Computer modelling P, M, B Example refs. [20,21,22,23,24,49,50,47,48,106,111, 115,118,129]	A range of modelling codes are available to assist in a wide range of RPV embrittlement issues, these range from codes designed to help interpret experimental data, predictions of irradiation induced phenomena, through to modelling of the emmbrittlement behavior of vessels. Examples include: dosimetry, recoil spectra, segregation, precipitation, TEM image simulation, positron lifetimes, SANS maximum entropy, rate theory etc. All models require a degree of experimental input for validation

1-4 Modeling of Radiation Embrittlement

The radiation embrittlement of RPVs that occurs over several decades originates from atomic displacements induced by neutron bombardment in a very short time (~ ps). In order to establish the mechanistic modeling of the radiation embrittlement such modeling should cover the phenomena that occurs in very wide time scale (from ps to decades) and in very wide dimensions (from sub nm to several tens of meters). In this section, the basic flow linking from atomic displacements to embrittlement is discussed along the time scale. Such sequential reactions are schematically shown along time scale in fig.1-17 [1-31], which is a common concept over any problems on radiation damage .

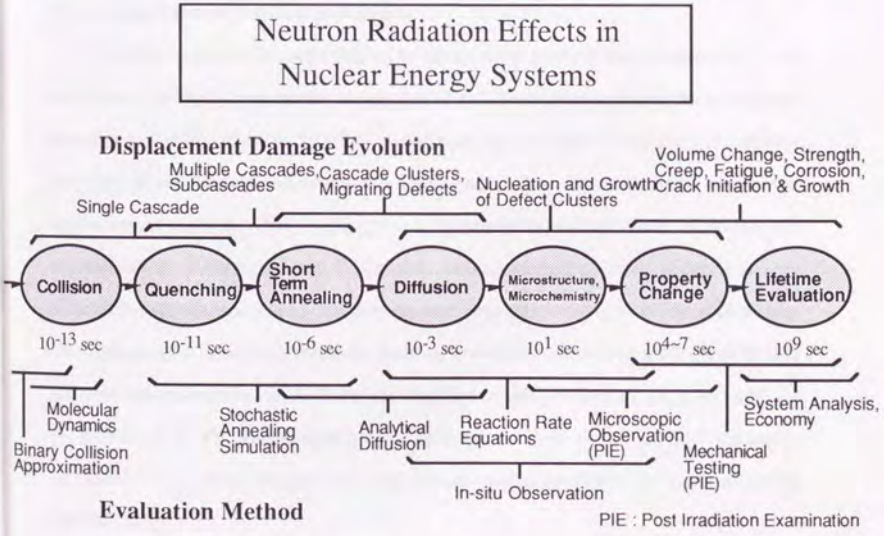

Fig.1-17 Sequential reactions along time scale for the development of microstructures from cascade damage by neutron irradiation. Small modification to [1-31].

1-4-1 Primary defect production

Energetic neutron bombardment to crystalline solids induces sequential displacement of lattice atoms from their lattice sites (displacement cascade). A schematic two-dimensional diagram of a cascade created by a fast neutron is shown in fig.1-18 [1-32]. It generates vacancies and interstitials in a displacement cascade, and they are the fundamental source of radiation embrittlement. The number of displaced atoms can be calculated as a function of primary knock-on atom (PKA) energy using the formalism developed by Norgett, Torrens and Robinson [1-33]. Since incident neutron flux and its energy spectrum can be converted to number of PKA and PKA energy spectrum using the displacement cross section, total number of vacancies and interstitials can be evaluated under a certain neutron exposure. This number gives displacement per atom (dpa) that is an internationally accepted exposure parameter. Thus dpa and damage rate (dpa/sec) can be estimated under a certain neutron exposure.

The dpa counts all the point defects produced by sequential displacements in a very short time (~ps) within a cascade irrespective of their fates. For modeling the subsequent phenomena it is necessary to describe the absolute number and configuration of vacancy and interstitial defects following the local short term rearrangement within the displacement cascade. This rearrangement (cascade annealing) leads to in-cascade recombination of vacancies and interstitials, and clustering of them. Since it is very difficult to experimentally study cascade damage structure that occurs within such a short time, computer simulation methods such as molecular dynamics (MD) and binary collision approximation (BCA) have been applied to this problem [1-34, 1-35, 1-36, 1-37, 1-38, 1-39, 1-40]. Recent examples of such approach are shown in figs.1-19 and 1-20 [1-40]. The current obtained insights through such approaches are summarized as follows [1-41];

1) The total residual defect production efficiency, or cascade efficiency η, defined as the ratio of the defects surviving the short term annealing (STA) to dpa, decreases from about

1 for very low energy recoils to about 0.25 to 0.45 at energies above 0.5 to 1keV; the variation of η with PKA energy is relatively slow at higher energies.

2) A significant fraction of the residual defects are contained in clusters of more than two defects. Maximum cluster sizes are 10 or greater. Clustering can be grossly defined in terms of the fraction of the residual defects contained in clusters $f_{i/vcl}$. The fractional clustering and average and maximum cluster size increase with increasing PKA energy. Clustering is also a function of the defect type, cluster size and temperature and is sensitive to the details of the MD or BCA/STA model. Various models predict clustering of 40% to more than 90% of the residual defect.

3) The corresponding estimate of the fraction of dpa in the form of mobile unclustered or 'freely migrating' residual defects is in the range of about 0.05 to 0.15.

A general view about cascades is vacancy-rich center surrounded by an interstitial rich region. The central region collapses to form a vacancy loop under certain conditions. Such vacancy loops that directly form from cascades during STA have been observed in neutron or self ion irradiated copper, however, they have never been observed in neutron or self ion irradiated iron. Although only very heavy ion irradiation like W produces very small vacancy loops that are observable with TEM [1-42], neutron irradiation seems not to form vacancy loops that directly form from cascades. Instead, positron lifetime measurements reveal small vacancy cluster formation like microvoids in neutron irradiated iron at liquid nitrogen temperature [1-43]. Since diffusion of vacancies at this temperature can be neglected, the vacancy clusters are believed to directly form from cascades in iron.

Although no direct evidence of interstitial clustering in isolated cascades has been reported in experiments on metals including iron under a wide range of irradiation conditions, indirect evidences for neutron irradiated nickel has been proposed by Kiritani [1-44]. In addition, recent computer simulations on copper and α-iron have demonstrated

the possibility of interstitial loop formation directly from cascades. This still has to be confirmed experimentally.

The number and configuration of point defects in cascades after short term annealing are key parameters for further modeling of the subsequent process such as diffusion or clustering. Much work is required for the precise evaluation of those key parameters such as η and fi/vcl.

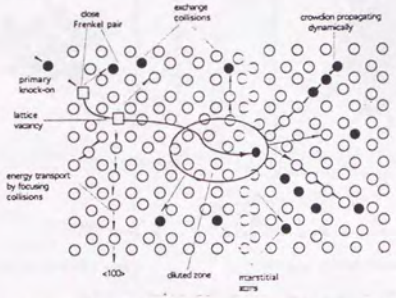

Fig.1-18 A schematic two-dimensional diagram of a cascade created in copper by a fast neutron [1-32].

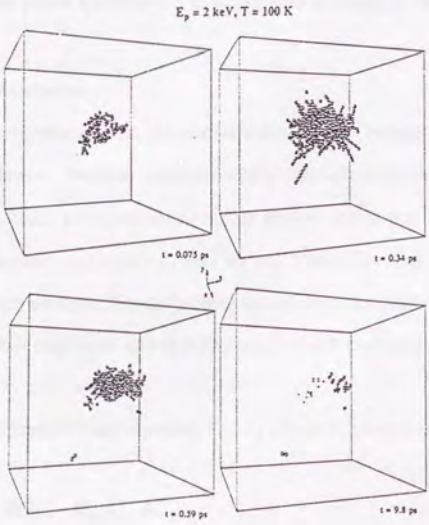

Fig.1-19 Vacant sites (small spheres) and displaced 'interstitial' atoms (large spheres) at four stages in the evolution of a 2keV cascade in α-iron at 100K [1-40].

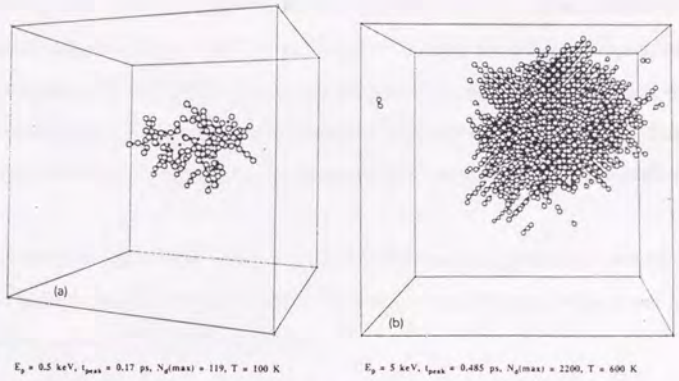

E_p = 0.5 keV, t_{peak} = 0.17 ps, N_d(max) = 119, T = 100 K

E_p = 5 keV, t_{peak} = 0.485 ps, N_d(max) = 2200, T = 600 K

Fig.1-20 Typical arrangement of vacant sites and displaced 'interstitial' atoms at the peak in number of displaced atoms for 0.5 and 5 keV cascades in α-iron [1-40].

1-4-2 Microstructural evolution

The point defects produced in the above ways are the source of the following microstructural evolution. Possible microstructural evolution includes clustering of vacancies and interstitials, precipitation of solute atoms, solute-point defect complex formation, grain boundary segregation, and so on. Vacancies and interstitials play important roles in each process. For describing the microstructural evolution, reaction rate equations are often employed and in many cases space-averaged approximation is applied.

Vacancy and interstitial concentration, C_V, C_I can be expressed in the simple form as follows;

$$\frac{dC_{v/i}}{dt} = G_{v/i} - RC_vC_i - D_{v/i}C_{v/i}S_{v/i}^{total} \qquad (1.1)$$

where $G_{V/I}$ is generation rate of each defect, R is recombination coefficient, $D_{V/I}$ is diffusion constant, and $S_{v/i}^{total}$ is total sink strength. The generation of point defects comes

from displacement cascade and thermal emission from extended sinks, then the net point defect generation rates are given as [1-45, 1-46];

$$G_{i/v} = \eta G_{dpa}(1 - f_{i/vcl}) + D_{v/i}\sum_j C^j_{v/i} S^j_{v/i} \qquad (1.2)$$

where η is cascade efficiency, G_{dpa} is generation rate of point defects calculated from the NRT model, $S^j_{v/i}$ are the point defect sink strengths for extended defects of type j, and $C^j_{v/i}$ are the point defect concentrations in equilibrium with these defects. In practice, the thermal emission term can be neglected compared with the cascade production term. Total sink strength composes of dislocations, grain boundaries, vacancy clusters and interstitial clusters.

Evolution of point defect clusters is dominated by direct generation rate from cascades and net balance of point defects flowing into and emitting from. It can be expressed as a series of j_{max} equations below;

$$\frac{dC^{v/icl}_j}{dt} = \alpha^{v/icl}_{v/i,j-1} C^{v/icl}_{j-1} + (\alpha^{v/icl}_{i/v,j+1} + \psi^{v/icl}_{j+1}) C^{v/icl}_{j+1} - (\alpha^{v/icl}_{v/i,j} + \alpha^{v/icl}_{i/v,j} + \psi^{v/icl}_j) C^{v/icl}_j + G^{v/icl}_j \qquad (1.3)$$

where $C^{v/icl}_j$ are the vacancy / interstitial cluster concentration containing j defects, $\alpha^{v/icl}_{v/i,j}$ are the rate constants for vacancy / interstitial impingement on a vacancy / interstitial cluster of size j, $\psi^{v/icl}_j$ are the rate constant for vacancy / interstitial emission rate from those clusters of size j, and $G^{v,icl}_j$ are the direct generation rate of vacancy / interstitial clusters of size j from cascades.

The rate constant for vacancy / interstitial impingement on a interstitial cluster (interstitial loop) of size j can be expressed as [1-45, 1-46];

$$\alpha^{icl}_{v/i,j} = \frac{z^j_{v/i}}{a_o^2} D_{v/i} C_{v/i} \qquad (1.4)$$

where $z^j_{v/i}$ are combinatorial numbers determined by the number of adjacent atomic sites from which an interstitial or vacancy can jump into an interstitial cluster of size j. This number can be computed for single defects and small clusters [1-47], but not available for large clusters. A continuum approach gives the following form for larger loops;

$$\alpha^{icl}_{v/i,j} = \frac{2\pi r_j}{\Omega_a} D_{v/i} C_{v/i} Z^L_{v/i}(j) \qquad (1.5)$$

where $Z^L_{v/i}(j)$ is the capture efficiency of a loop that is assumed to be proportional to the reciprocal of the square of the cluster radius between the lower limit (consistent value

with combinatorial number for single defects) and the upper limit (~capture efficiency for dislocation network) [1-45, 1-46].

The rate constant for vacancy / interstitial impingement on a vacancy cluster in spherical shape of size *j* can be expressed as [1-41];

$$\alpha_{v/i,j}^{vcl} = \frac{4\pi r_j}{\Omega_a} D_{v/i} C_{v/i} \quad . \tag{1.6}$$

The rate constant for interstitial emission from an interstitial loop is:

$$\psi_j^{icl} = \frac{D_i}{a_o^2} \exp\left(-\frac{E_j^B}{kT}\right) \tag{1.7}$$

where E_j^B is the binding energy of an interstitial to a cluster of size j. Stoller treats the emission from interstitial loops only for di-, tri- and tetra- interstitial clusters and neglect such emission from larger loops [1-45, 1-46].

The rate constant for vacancy emission from an vacancy cluster of size j can be written as [1-41];

$$\psi_j^{vcl} = 4\pi r_j D_{sd} \exp\left(\frac{2\gamma_{eff}\Omega_m}{r_j RT}\right) / \Omega_a \tag{1.8}$$

where D_{sd} is self-diffusion coefficient, γ_{eff} is effective surface energy, and Ω_m is molar volume.

By numerically solving equations (1.1) and (1.3) for vacancies, interstitials and their clusters simultaneously, their time evolution can be obtained. There are still many unknown parameters in the equations to result in reduction in reliability of the calculated results.

Clustering of solute atoms such as copper can be treated by an equation like equation (1.3). Then a key parameter is radiation enhanced diffusion coefficient, $D_{solutes}^{rad}$. $D_{solutes}^{rad}$ depends on vacancy concentration, vacancy diffusivity, binding energy between solutes and vacancies etc. It has not been established for copper in iron matrix.

1-4-3 Correlation between Microstructure and Mechanical properties

When radiation hardening is related to radiation-induced microstructural features, planar barrier models which describe the interaction forces of various defects as they impede dislocation motion along the slip plane are often employed. These models are generally derived from Orowan's theory for the athermal bowing of dislocations around obstacles, expressed as:

$$\Delta\tau = \frac{Gb}{\beta\bar{\ell}} \tag{1.9}$$

where τ is the shear stress, b is the magnitude of Burgers vector, $\bar{\ell}$ is the mean interpartial spacing, and β is the strengthening factor. The full Orowan force required to move a dislocation past an impenetrable obstacle, leaving behind a dislocation loop, is Gb^2 for a periodic array of obstacles and $0.84Gb^2$ [1-48] for a random array. The mean interpartial spacing $\bar{\ell}$ is given by $\bar{\ell} = \sqrt{Nd}$ where N is number density of obstacles, and d is the mean diameter of them. The increment change in shear stress can be related to the change in yield stress change using the Taylor factor in the case of polycrystalline materials as [1-49]:

$$\Delta\sigma_y \cong 3.1\Delta\tau. \tag{1.10}$$

In addition, Russell-Brown model is often used for calculation of hardening by dispersed precipitates of different shear modulus from matrix [1-50].

1-4-4 Correlation between hardening and embrittlement

The grain boundary segregation has been considered to have little effect on the embrittlement of RPV steels in the present EOL dose level of PWRs (typically ~2×10^{23} n/m^2). Then, hardening is the main contribution to embrittlement. As discussed in 1-3-1, correlation between increment change in yield stress and ΔDBTT is well established, therefore ΔDBTT can be calculated from $\Delta\sigma_y$.

1-4-5 Examples of mechanistic modeling

There are some examples that attempt to establish better prediction formalism based on mechanistic understandings. As embrittlement mechanisms are not fully understood, hardening features treated in them are different among the examples.

Odette et al. [1-8, 1-16, 1-25, 1-41, 1-51] treat copper rich precipitates and matrix defects. For copper rich precipitates, they assume rapid nucleation and diffusion-controlled growth. They distinguish matrix defects into three types with their thermal stability estimated in annealing experiments as unstable matrix defect (UMD), metastable matrix defect (MMD) and stable matrix defect (SMD).

Fisher and Buswell [1-9] propose a semi-empirical prediction formalism for Magnox reactor pressure vessel. They also treat copper precipitates and matrix defects. Copper precipitates contribution is calculated as acceleration of thermal aging behavior by supersaturated vacancies, therefore the copper contribution to hardening shows a peak value at a certain fluence and the peak hardness is calculated from the volume fraction of copper with Russell-Brown model. Matrix defect contribution is simply regarded as $A(\phi t)^{0.5}$, and A is determined by the data for low copper steels. They consider the total hardening as the linear sum of the two contribution.

Simons assumes that cascade-vacancy clusters stabilized by copper atoms act as nucleation sites of copper clusters and deduces a semi-empirical formula for embrittlement prediction [1-52]. Number density of the clusters is controlled by balance of formation from cascade, annihilation by cascade overlapping, and thermal annihilation. Cluster size is determined by radiation enhanced diffusion of copper atoms. He also applies Russell-Brown model, and his formalism includes many fitting parameters to be determined with statistic analysis.

Stoller estimates the contribution of interstitial loops and cascade-vacancy clusters to hardening with rate equation approach [1-45, 1-46]. He describes reaction rate equations for vacancies, interstitials, interstitial loops and vacancy clusters to solve them simultaneously, and demonstrates the effect of damage rate and irradiation temperature on point defect transient and cluster hardening. It is remarkable that no fitting parameters to

mechanical properties are employed in his calculation, therefore his approach is purely mechanistic.

Taguchi's semi-empirical formalism is proposed in his graduation thesis (1986) for the University of Tokyo under instruction by Ishino [1-53]. It is introduced here in some detail because there is no reference about it in English. He considers Cu-C-vacancy complexes as embrittlement features, and he assumes ΔDBTT is proportional to number density of them. Number density of Cu-C-vacancy, N, is expressed as:

$$\frac{dN}{dt} = K_{Cu-V} C_{Cu} C_v - K_N N \tag{1.11}$$

where only encounter of copper and vacancy, and its thermal dissociation are considered. Vacancy concentration is regarded as $C_v = \beta\phi^n$, and nickel is thought to have an effect of removal of vacancies from vicinity of nickel atoms to increase apparent vacancy concentration as:

$$C_v = \frac{\beta\phi^n}{1 - aNi} \tag{1.12}$$

Then he analytically solves (1.11) by replacing C_V with (1.12) and obtains;

$$N = K_{Cu-V}\beta \frac{C_{Cu}}{1 - aNi} \phi^n \frac{1 - \exp(-K_N t)}{K_N} \tag{1.13}$$

This gives the function form of ΔDBTT including four fitting parameters, c_1, c_2, c_3 and n, as;

$$\Delta DBTT = c_1 \frac{Cu}{1 - c_2 Ni} \phi^n \frac{1 - \exp(-c_3 t)}{c_3} \tag{1.14}$$

He applies this semi-empirical formula to some data bases (NUREG/CR-3391, HEDL-TME 83,22), and reports that it gives as good correlation as Guthrie's formula [1-15] for plates but does not give as good correlation as Guthrie's for welds.

1-5 Objectives of this study

As discussed above, although there are some models of radiation embrittlement proposed by different groups, modeled mechanisms differ among the groups. It is because the identification of the embrittlement mechanisms has not been completed yet all over the world.

Since the current prediction methods are derived from statistic analysis and do not consider physical meanings, physico-based methods are considered to have a possibility to give more reliable prediction. In order to establish such physico-based methods, the embrittlement mechanisms should be fully understood, however they are still unsolved. Many factors such as complexity of material conditions, invisibility due to very fine microstructural features below TEM resolution, and poor control of irradiation conditions make clear understanding of the embrittlement mechanisms so difficult. Therefore full use of available knowledge acquired through experiments of the different materials and irradiation conditions including model alloys and ion irradiation is required for better understanding of embrittlement mechanisms. This concept of correlation among different irradiation conditions based on physical understandings is called 'irradiation correlation', and its importance has been widely recognized. The prediction of the radiation embrittlement is a typical case of application of the irradiation correlation.

For the study on the embrittlement mechanisms, neutron irradiation has been the main irradiation methods. The neutron irradiation can produce 'similar' irradiation conditions to the practical RPV condition to a certain extent, however accelerated irradiation is substantially necessary because the embrittlement of the practical RPVs occurs over several decades. It takes considerably long time even for accelerated neutron irradiation to result in low productivity of the irradiated specimens. In addition, the recent global trend of shut down of test reactors spurs on the low productivity. Moreover, it is essentially difficult for neutron irradiation to produce well-controlled irradiation conditions. These facts make production of systematic irradiation matrix difficult. On the contrary, ion irradiation has advantage of good controllability of irradiation conditions over wide ranges of dose, dose rate and irradiation temperature. Therefore, it is natural

that ion irradiation is expected to produce systematic irradiation matrix for study on the radiation embrittlement mechanisms. In addition, little radioactivity makes handling of the ion-irradiated specimens easier than the neutron-irradiated specimens.

However unlike neutron irradiation that produces atomic displacement uniformly (in a macroscopic sense) over whole volume of a specimen, ion irradiation produces atomic displacement only in very small volume close to irradiation surface. This makes various post irradiation experiment (PIE) methods that are available for the neutron-irradiated specimens difficult or unavailable. For example, the tensile test, a very general PIE method for the neutron-irradiated specimens, is not available for the ion-irradiated specimens except for very high energy light ion-irradiated specimens. Although ion irradiation has been widely used for study on void swelling and radiation induced segregation with the TEM technique, such approach has not been successful for the RPV embrittlement mechanisms because the resolution of TEM is not sufficient for the study on the RPV embrittlement. Therefore in this study positron annihilation is attempted to be applied to investigation of microstructure in the ion-irradiated specimens for study on the RPV embrittlement mechanism due to its very high sensitivity to vacancy-type defects. In order to detect vacancy-type defects that exist only within the small volume close to the irradiation surface, the variable energy monoenergetic positron beam technique is employed.

Thus, the objectives of this study are:

To investigate the mechanisms of the radiation embrittlement of RPV steels by use of model alloys, ion irradiation and positron beam technique.

To investigate formation of matrix defects, behavior of copper during irradiation, and effects of dose or irradiation temperature on them.

To study correlation between microstructural features that form during irradiation and the resultant hardening through surface hardness measurement.

To demonstrate applicability of ion irradiation to study on the RPV embrittlement mechanisms through these experiments.

In the following, the method and the results of the positron beam experiment are discussed in Chapter 2. The results of the hardness measurement and the correlation between the hardening and the results of the positron beam experiment are discussed in Chapter 3. In Chapter 4, the nature of the hardening features that form under ion irradiation in the model alloys is discussed. It is also discussed how the evolution of the features is modeled and how the obtained understandings for the ion irradiated model alloys are applied to the neutron irradiated practical steels. Then this thesis is concluded in chapter 5.

1-6 References

1-1 L. E. Steele, in *Neutron Irradiation Embrittlement of Reactor Pressure Vessel Steels*, IAEA Technical Reports Series No.163 (1975).

1-2 W. Marshall, in *An Assessment of the Integrity of PWR Pressure Vessels* (1982).

1-3 W. J. Phythian and C. A. English, J. Nucl. Mater. 205 (1993) 162.

1-4 C. Z. Serpan, Jr., Nucl. Eng. Des. 8 (1968) 95.

1-5 T. R. Mager et al., ASTM-STP 784 (1983) 151.

1-6 H. Susukida, in *The Structural Materials of Light Water Reactor*, IPC (1989), in Japanese.

1-7 H. L. Heinisch, J. Nucl. Mater. 178 (1991) 19.

1-8 G. R. Odette and G.E. Lucas, ASTM-STP 909 (1986) 206.

1-9 S. B. Fisher, and J. T. Buswell, Int. J. Pres. Ves. & Piping, 27 (1987) 91.

1-10 J. R. Hawthorne, ASTM-STP 909 (1986) 235.

1-11 G. F. Carpenter, N. R. Knopf and E. S. Byron, Nucl. Sci. Eng., 19 (1964) 18.

1-12 J. R. Hawthorne and U. Potapovs, ASTM-STP 457 (1969) 113.

1-13 M. Kiritani, J. Nucl. Mater. 169 (1989) 89.

1-14 R. K. Nanstad, K. Farrell, D. N. Braski and W. R. Corwin, J. Nucl. Mater. 158 (1988) 1.

1-15 G. L. Guthrie, in *Charpy Trend Curves Based on 177 PWR Data Points, LWR Pressure Vessel Surveillance Dosimetry Improvement Program Quarterly Progress Report,* NUREG-3391-2, HEDL-83-22, Nuclear Regulatory Commission (1984).

1-16 G. R. Odette and P. Lombrozo, in *Physically-Based Regression Correlations of Embrittlement Data from Reactor Pressure Vessel Surveillance Programs*, EPRI NP-3319, Electric Power Research Institute (1984).

1-17 S. Ishino, T. Kawakami, T. Hidaka and M. Satoh, Nucl. Eng. Des. 119 (1990) 139.

1-18 K. Kussmaul, J. Fohl and T. Weissenberg, ASTM-STP 1046 (1990) 80.

1-19 W. J. Phythian, C. A. English and J. T. Buswell, Proc. 5th Int. Sym. on Environmental Degradation of Reactor Materials - Water Reactors, Monterey, California, 1991 (ANS Order No 700176, 1992).

1-20 P. McConnell, W. L. Server and W. Oldfield, in *Irradiated Pressure Vessel Steel Data Base*, EPRI-NP-2428, Electric Power Research Institute (1982).

1-21 J. T. Buswell, C. A. English, M. G. Hetherington, W. J. Phythian, G. D. W. Smith, and G. M. Worrall, ASTM-STP 1046 (1990) 127.

1-22 W. J. Phythian, A. J. E. Foreman, C. A. English, J. T. Buswell, M. Hetherington, K. Roberts and S. Pizzini, ASTM-STP 1127 (1992) 131.

1-23 F. Maury, N. Lorenzelli and C. H. De Novion, J. Nucl. Mater. 183 (1991) 217.

1-24 M. K. Miller and M. G. Burke, ASTM-STP 1046 (1990) 107.

1-25 G. R. Odette, P. M. Lombrozo and R. A. Wullaert, ASTM-STP 870 (1985) 840.

1-26 G. Solt, F. Frisius, W. B. Waeber and W. Bührer, ASTM-STP 1046 (1990) 154.

1-27 I. E. Ukpong, A. D. Krawitz, D. F. R. Mildner, and H. P. Leighly, Jr., ASTM-STP 956 (1987) 480.

1-28 F. Maury, N. Lorenzelli and C. H. De Novion, J. Nucl. Mater. 183 (1991) 217.

1-29 P. J. Othen, M. L. Jenkins, G. D. W. Smith and W. J. Phythian, Phylos. Mag. Lett. 64 (1991) 383.

1-30 P. Auger, P. Pareige, M. Akamatsu and J. C. Van Duysen, presented at 17th Symposium on Effects of Radiation on Materials, Sun Valley, Idaho, June, 1994.

1-31 N. Sekimura, in *Nuclear Power and Advanced Technology [I]*, NSA / COMMENTARIES: No.2 (1994) 1, in Japanese.

1-32 A. Seeger, Proc. 2nd UN Int. Conf. on Peaceful Uses of Atomic Energy, Geneva, 1958, vol.6 (United Nations, New York, 1958) p.250.

1-33 M. J. Norgett, M. T. Robinson and I. M. Torrens, Nucl. Eng. Des. 33 (1975) 50.

1-34 T. Diaz de la Rubia, R. S. Averback, R. Benedek and I. M. Robertson, Rad. Eff. & Def. in Sol. 113 (1990) 39.

1-35 T. Diaz de la Rubia and M. W. Guinan, J. Nucl. Mater., 174 (1990) 151.

1-36 A. J. E. Foreman, C. A. English, W. J. Phythian, D. J. Bacon and M. L. Jenkins, in *Materials Modeling: From Theory to Technology*, ISBN 0-7503-0196-1, Institute of Physics, Bristol (1992).

1-37 A. J. E. Foreman, W. J. Phythian and C. A. English, Phil. Mag. A 66 (1992) 671.

1-38 H. L. Heinisch, D. G. Doran and D. M. Schwartz, ASTM-STP 725 (1981) 191.

1-39 H. L. Heinisch and F. M. Mann, J. Nucl. Mater. 122&123 (1984) 1023.

1-40 A. F. Calder and D. J. Bacon, J. Nucl. Mater. 207 (1993) 22.

1-41 G. R. Odette, "Modeling Irradiation Embrittlement in Reactor Pressure Vessel Steels", in *Irradiation Effects in Pressure Vessel Steels*, M. Davies, Ed, Technical Reference Series Publication, International Atomic Energy Agency, Vienna, to be published.

1-42 M. L. Jenkins, C. A. English and B. L. Eyre, Philos. Mag. A. 38 (1978) 97.

1-43 P. Hautojärvi, L. Pöllänen, A. Vehanen and J. Yli-Kauppila, J. Nucl. Mater. 114 (1983) 250.

1-44 M. Kiritani, J. Nucl. Mater. 216 (1994) 220.

1-45 R. E. Stoller, in *Modeling the Influence of Irradiation Temperature and Displacement Rate on Radiation-Induced hardening in Ferritic Steels*, NUREG/CR-5859 ORNL/TM-12073 U.S. Nuclear Regulatory Commission, Washington D.C. (1992).

1-46 R. E. Stoller, ASTM-STP 1175 (1993) 394.

1-47 J. R. Beeler, Jr. and R. A. Johnson, Phys. Rev. 156 (1967) 677.

1-48 U. F. Kocks, in *Physics of Strength and Plasticity*, p.143, MIT press, Cambridge (1969).

1-49 U. F. Kocks, Metall. Trans. 1 (1970) 1121.

1-50 K. C. Russell and L. M. Brown, Acta Metall. 20 (1972) 969.

1-51 G. R. Odette, E. V. Mader, G. E. Lucas, W. J. Phythian and C. A. English, ASTM-STP 1175 (1993) 373.

1-52 R. L. Simons, ASTM-STP 956 (1987) 535.

1-53 M. Taguchi, Graduation Thesis for the University of Tokyo (1986), in Japanese.

2. Microstructural evolution in ion-irradiated model alloys detected by positron beam

2-1. Introduction

Since the shift in ductile-brittle transition temperature of RPV steels due to neutron irradiation is related to yield stress increase, matrix hardening leads to embrittlement [2-1] as discussed in Section 1-4. The matrix hardening is believed to result from formation of dispersed barriers against dislocation movement. The nature of the dispersed barriers has not been well understood yet, and many efforts have been made to reveal the mechanisms.

Copper impurity in steels is well known to have a great effect on the embrittlement according to the data analyses of the mechanical property tests after the surveillance and material test reactor (MTR) irradiation [2-2, 2-3]. Various microanalytical methods such as field emission gun/scanning transmission electron microscopy (FEG/STEM) [2-4, 2-5, 2-6], small angle neutron scattering (SANS) [2-5, 2-6, 2-7, 2-8], positron annihilation (PA) [2-4, 2-9, 2-10, 2-11, 2-12], and atom probe field ion microscopy (APFIM) have been applied to the study on the nature of fine particles produced by neutron irradiation [2-13, 2-14]. Production of the copper-rich precipitates and the matrix defects have been reported as the dominant mechanisms from these methods [2-2, 2-13, 2-14], and more study is required to obtain knowledge about their nature and the processes of formation, growth, and annihilation. The processes are controlled by many factors such as neutron fluence, neutron flux, neutron energy spectrum, irradiation temperature, chemical composition, microstructure, etc. Irradiation experiments in which these factors are separately controlled are desirable for better understanding of the mechanisms. In this study iron-based model alloys and ion irradiation are applied to the problems of the radiation embrittlement mechanisms. The model alloys are used for investigation of the copper effect on microstructural evolution. Ion irradiation, which has been used for fundamental study of radiation damage, has the advantages of relatively easy control of irradiation conditions such as damage rate and irradiation temperature, and low radioactivity of ion irradiated samples, which makes handling of the specimens easy. However, displacement damage produced by ion

irradiation is limited only near irradiation surface. It makes conventional post irradiation experiments such as tensile test, hardness test, and several microstructural experiments difficult. In this study, microstructural information in the damage region near the surface was obtained with variable energy monoenergetic positron beam technique.

Positron annihilation technique has been widely applied to study of radiation damage, especially vacancy-type defects, because positrons are selectively trapped and annihilate at vacancies or open-volume defects. This technique is so sensitive to the vacancy type defects that the small vacancy clusters below resolution limit of TEM and even monovacancies are detectable. A positron annihilates with an electron to emit annihilation photons with energy corresponding to the mass energy of an electron and a positron. Since implanted positrons are sufficiently thermalized in solids, the annihilating photons have information on electrons in solids. There are three types of the positron annihilation techniques; 1) lifetime measurement, 2) angular correlation, and 3) Doppler broadening.

Lifetime measurements have been applied to studies on lattice defects and radiation damage most frequently of the three techniques, because decomposition of lifetime spectrum can provide information on both size and population of vacancy type defects. Calculations based on Schrödinger equations have given the correlation between the positron lifetime and the size of vacancy clusters in some metals [2-15], and the calculated lifetime for monovacancies in iron is similar to measured value for electron-irradiated iron at liquid nitrogen temperature. Although the vacancy clusters formed by irradiation and the following annealing have size distribution, a lifetime spectrum is decomposed into 2 or 3 lifetime components using calculation code such as RESOLUTION [2-16] to get averaged, mainly qualitative, information on size and number density of vacancy clusters. It makes the interpretation of the experimental results model-dependent.

The Doppler broadening and the angular correlation of the annihilation photons reflects the momentum distribution of the annihilating electrons, which is a

superposition of narrow parabolic part, corresponding to the annihilation with conduction electrons, and broad part corresponding to the annihilation with core electrons. Therefore those techniques give essentially similar information on vacancy type defects. A schematic view of comparison among three techniques is shown in fig.2-1 [2-17]. Because of the simpler measurement system and higher counting rate than angular correlation, Doppler broadening has been often combined with positron beam technique. When positrons are trapped and annihilate at vacancies, the broad part is reduced and the whole energy spectrum is sharpened. The Doppler broadening can be characterized by S-parameter, the fraction of counts in central region of whole energy spectrum, and the positrons trapped by vacancy type defects make S-parameter higher. In the present study the S-parameter is measured to detect vacancy type defects.

The objectives of this chapter are to investigate the formation of vacancy clusters and behavior of copper atoms under irradiation using the ion irradiation and the variable energy positron beam technique, and to obtain information on the dependence of microstructural evolution on the copper content, irradiation dose, and irradiation temperature.

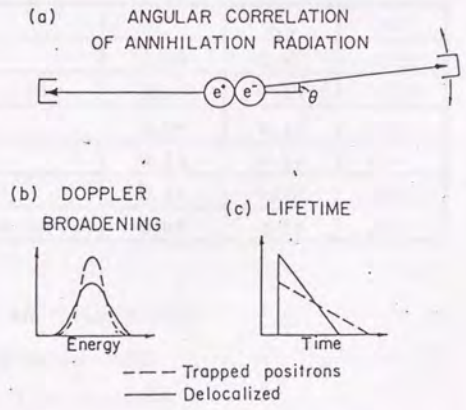

Fig.2-1 A schematic view of the three typical positron annihilation technique for detection of vacancy-type defect [2-17].

2-2. Experimental

2-2-1. Model alloys

The chemical compositions of the model alloys investigated in this study are shown in table 2-1. The copper contents are 0.1 and 0.4 wt.% (Fe-0.1C-0.1Cu, and Fe-0.1C-0.4Cu, respectively). 0.7wt.% of nickel was added to Fe-0.1C and Fe-0.1C-0.1Cu. All the model alloys were melted by high frequency induction heating in vacuum, hot-rolled. They were mechanically machined to 24ϕ x 2 mm disks for the positron annihilation measurement. They were annealed in vacuum using recrystallization annealing of 1130 K-0.5h followed by solution annealing of 1023 K-1h, and then furnace-cooled. They were electropolished finally using a 900 ml acetic acid-100 ml perchloric acid-0.5 g chromium trioxide (CrO_3) electrolyte to make the irradiation surface flat.

Table 2-1 Chemical composition (wt.%) of the model alloys investigated

	C	Cu	Ni
Fe	0.006	0.001	<0.01
Fe-0.1C	**0.10**	0.001	<0.01
Fe-0.1C-0.1Cu	**0.09**	**0.11**	<0.01
Fe-0.1C-0.4Cu	**0.10**	**0.38**	<0.01
Fe-0.1C-0.7Ni	**0.11**	<0.01	**0.72**
Fe-0.1C-0.1Cu-0.7Ni	**0.09**	**0.11**	**0.72**

Fe : balance

other elements: Si, Mn, Cr, Mo, V < 0.01

P, S, Sn, As < 0.003

Al, Ti, Nb, Co < 0.005

Table 2-2 Interstitial impurity level in Fe and Fe-0.1C after final annealing (wt.%)

	C	O	N
Fe	0.006	0.0074	0.0003
Fe-0.1C	0.1	0.0049	0.0003

2-2-2. Ion irradiation

2-2-2-1. High Fluence Irradiation Facility, the University of Tokyo (HIT)

In order to introduce displacement damage, the disk specimens for the positron measurement were irradiated with Ni ions accelerated to 3 MeV by the Tandetron accelerator at the High Fluence Irradiation Facility, the University of Tokyo (HIT).

HIT facility has two accelerators; Tandetron and Van de Graaf. The former mainly produce heavy ions, and the latter mainly produce light gas ions, and their maximum terminal voltages are 1 MV and 3.75 MV, respectively. HIT has five beam lines called BL1 to 5. The BL1 to 4 are light ion beam lines, and the BL5 is heavy ion beam line. Nickel ion beam has been mainly used with the BL5. The BL4 and 5 are connected to the so-called "dual beam irradiation chamber" to realize dual beam irradiation of heavy and light ions to study the synergistic effect of displacement damage and gas atom production on fusion materials. The overall view of HIT facility is shown in fig.2-2.

The heavy ion irradiation was carried out in dual beam irradiation chamber. The details of the chamber is discussed elsewhere [2-18]. It is evacuated by turbo molecular pump and ion pump to achieve 10^{-5} Pa. The chamber has dual ion irradiation stage to hold the specimens, heat the specimens, and measure the ion beam current. The stage is shown in fig.2-3. It has three sample holders called stage1 to 3 and two Faraday cup arrays one of which is for the heavy ion beam perpendicular to sample and the other is for the light ion beam tilted from perpendicular direction. This stage moves horizontally with a pulse motor and its controller so that the sample holders and the Faraday cup arrays stand at the same place in the beam course. A TEM disk holder can hold twenty 3mmØ TEM disks by 5x4 array on the thermalizing block. Thermalizing block can be heated by electron beam heating behind the ion beam direction and two Almel-Chromel

thermocouples are inserted into the hole of the thermalizing block to monitor the temperature. The structure of the TEM disk holder and the electron beam heating sub assembly is shown in fig. 2-4 [2-18]. The heating power is varied by feedback control of grid voltage to keep the temperature constant (fig.2-5 [2-19]). Although precision of temperature control is better for higher temperature, irradiation temperature was kept within ± 3K for the set temperature of 563K. The Faraday cup array consists of 20 micro Faraday cup with 2mm diameter (fig.2-6 [2-18]). Secondary electrons are suppressed by suppresser with voltage of 50V. The Faraday cup array can measure ion beam profile. When operator of accelerator starts up the ion beam, he can check position and broadening of ion beam with the beam profile monitor and he adjusts the position and condense beam with ion beam steerer and quadruple lenses. The well centered and focused ion beam is scanned by electrostatic ion beam scanner with high frequency of 1 to 10 kHz so that desired area can be irradiated. Although the system can measure the beam profile, the beam current cannot be monitored during irradiation. Therefore beam profile is checked with interval (typically 1 hour) by interruption of irradiation. Although the ion beam current may change between the interval, the error of dosimetry can be estimated as below 20%.

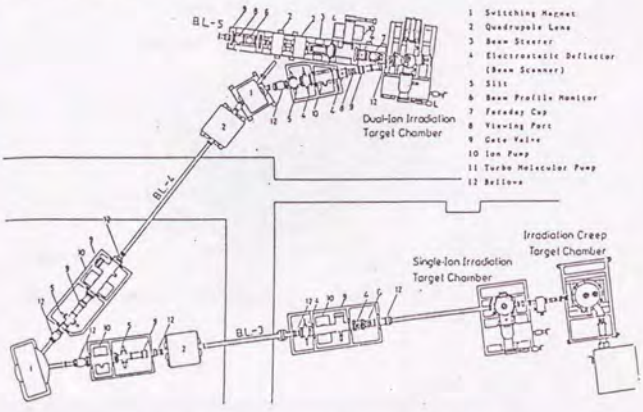

Fig.2-2 Overall view of HIT facility [2-18]

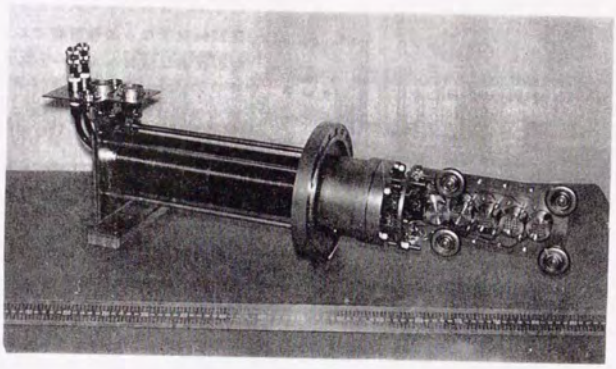

Fig.2-3 Ion irradiation stage for beam line 5 [2-18]

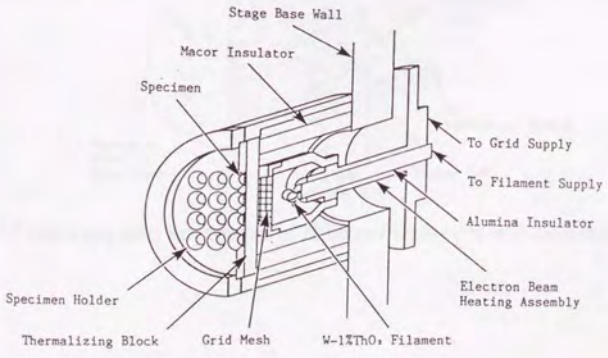

Fig. 2-4 Structure of TEM disk holder and the electron beam heating sub assembly [2-18].

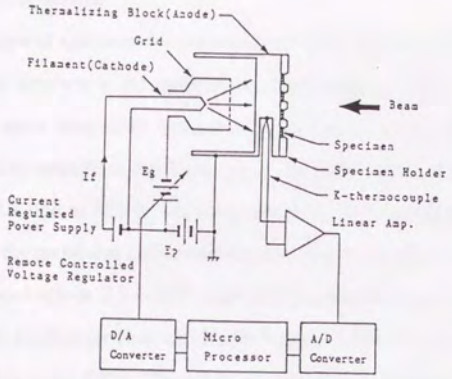

Fig.2-5 A schematic figure of the electron beam heating system [2-19]

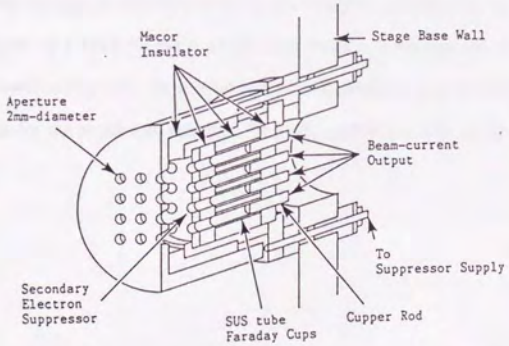

Fig.2-6 Faraday cup array that consists of 20 micro Faraday cup with 2mm diameter [2-18]

2-2-2-2. Irradiation conditions

Since the shape of specimen for positron annihilation measurement is 24Ø disk, they were directly attached to the thermalizing block with two bolts for irradiation. Displacement per atom (dpa) at the damage peak is used as a scaling parameter for the irradiation dose. The irradiation conditions are at first 0.001, 0.01 dpa at 563 K for all specimens, and 0.1 dpa at 563 K and room temperature is added to Fe-0.1C-*x*Cu specimens, while the maximum end-of-life neutron dose at the belt line of a four-loop PWR pressure vessel will be 2.3×10^{23} n/m^2 [2-20] corresponding to 3.9×10^{-2} dpa. The damage rate at the damage peak was 3×10^{-5} dpa/s, which is greater by 7 orders of magnitude than that in the RPVs. Therefore, cascade density during ion irradiation is very high, which might make the damage efficiency very low. This can make the radiation-induced change enhanced or suppressed by the accelerated irradiation [2-21]. According to the damage profile calculated by the EDEP-1 code [2-22], the thickness of the layer damaged by 3 MeV Ni ion is about 1 μm thick and the damage peak is 0.6 μm deep from the surface (fig.2-7). Implanted nickel concentration is below 40 appm at the range peak even for the maximum ion dose. The effect of nickel will be discussed later.

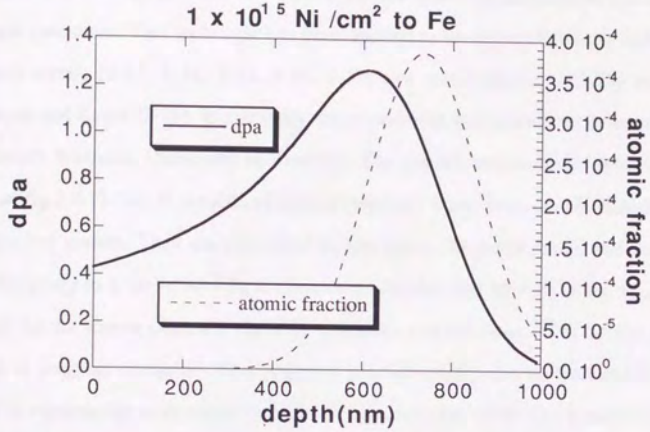

Fig.2-7 Displacement damage depth profile calculated with EDEP-1 code

(3MeV Ni^{2+} to 1 x 10^{15} ions/m^2 in pure Fe)

2-2-3. Variable energy positron beam technique

The variable energy positron beam technique was applied to unirradiated and ion-irradiated specimens. This technique has been applied to detection of defects in ion-irradiated metals [2-23, 2-24, 2-25, 2-26, 2-27] and semiconductors [2-28] since Trifshäuser and Kögel [2-29]. In this study, the experiment was carried out at Institute of Materials Sciences, University of Tsukuba. The overall measurement system is shown in fig.2-8 [2-30]. It consists of source chamber, beam line, sample chamber, and detection system. They are evacuated by ion pump, Ti getter pump, and turbo molecular pump to achieve 10^{-7} Pa at the source chamber and 10^{-9} Pa at the sample chamber. In the source chamber (fig.2-9), positrons emitted from ^{22}Na source are injected to tungsten converter. The positrons are sufficiently thermalized and then emitted to vacuum due to the negative positron work function of W. The positrons are extracted to grid by 100V of extraction voltage. This source chamber and the attached electronic apparatuses are electrically isolated from grand so that the whole source chamber can have the positron accelerating voltage up to 50kV. Beam line has a 45° curve to select positrons of desired low energy. The slow positron beam is bent by magnetic field produced by 9 coils. The positrons that have passed through the curve are electrostatically accelerated and introduced to sample chamber. Sample chamber also has two condenser coils to finally focus the beam. Doppler broadening of annihilation photons is measured with Ge detector (ORTEC CFG-SH-GEM). The block diagram of system for measuring the Doppler broadening of the annihilation photons as a function of the incident positron energy is shown in fig.2-10.

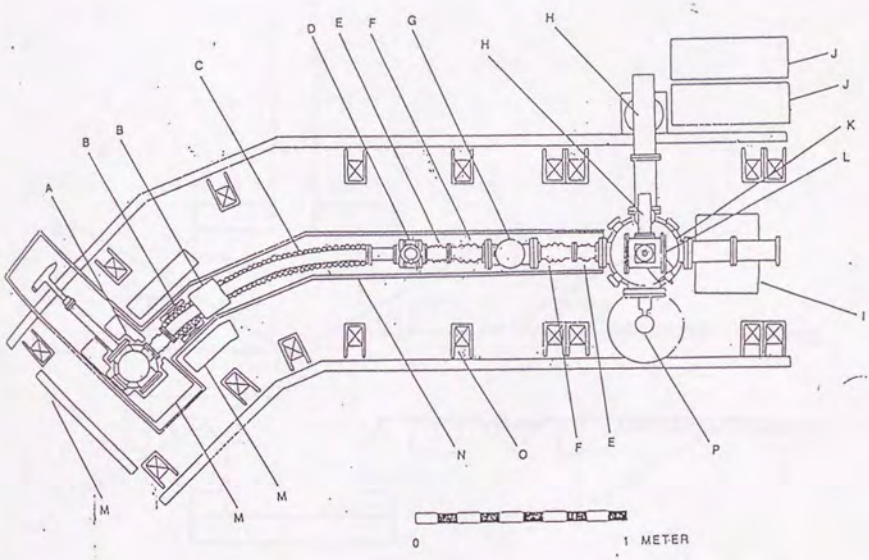

Fig.2-8 The overall view of the positron beam experiment system. (A) positron source chamber (B) correction coil (C) solenoid (D) gate valve (E) bellows (F) 50keV ceramic breaks (G) accelerator (H) turbo molecular pump (I) ion pump (J) rotary pump (K) sample chamber (L) sample preparation chamber (M) lead wall (N) adrylic acid resin plate (O) magnet coil (P) Ge detector [2-30].

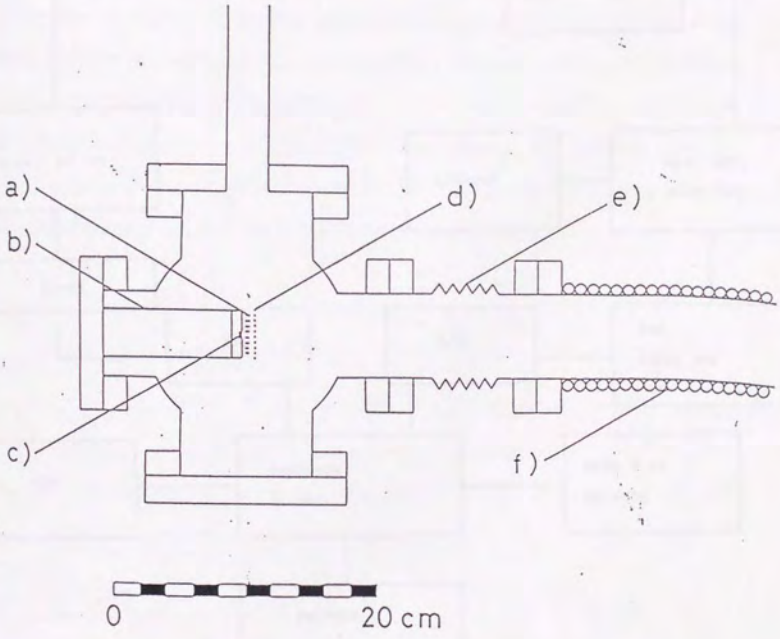

Fig.2-9 The schematic view of the source chamber as viewed from above: (a) W-converter (b) source holder (c) ^{22}Na source (d) extraction grid (e) bellows (f) solenoid [2-30].

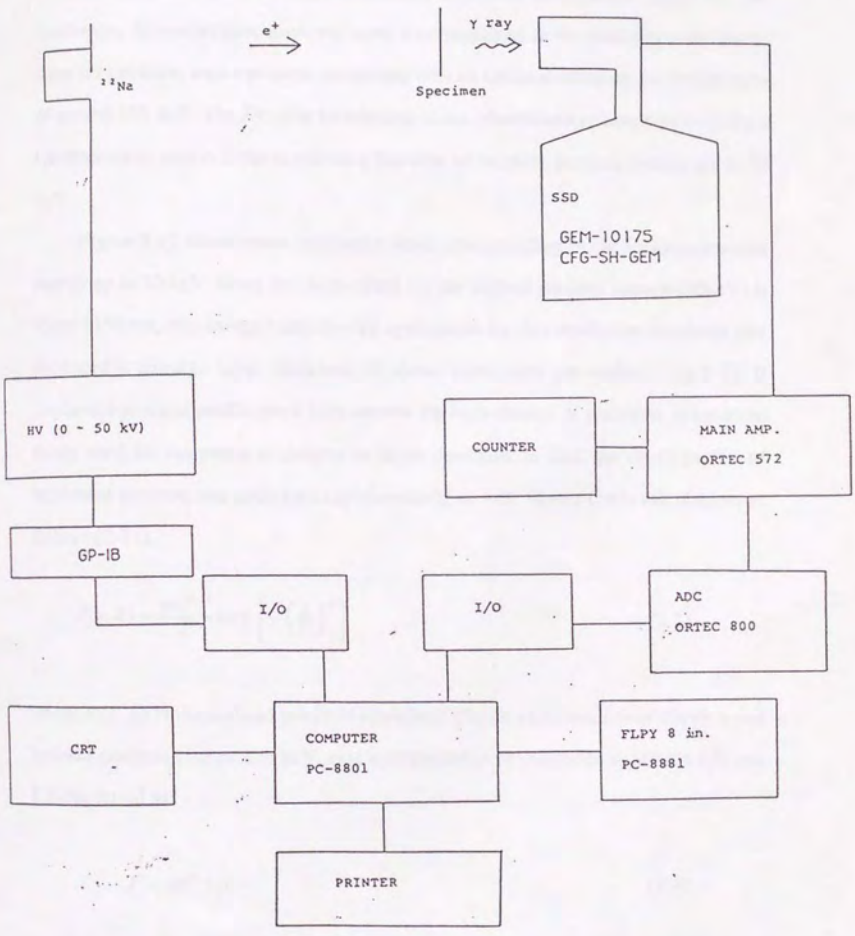

Fig.2-10 System for measuring Doppler broadening as a function of incident positron energy [2-30].

2-3 Variable energy positron beam experiment

A schematic view of this experiment is shown in fig.2-11. After the ion irradiation, monoenergetic positron beam was implanted to the irradiation surface at room temperature, then a positron annihilates with an electron, emitting the two photons of around 511 keV. The Doppler broadening of the photon energy was measured by a Ge detector to obtain S-parameter as a function of incident positron energy up to 30 keV.

Figure 2-12 shows mean implanted depth corresponding to the incident positron energy up to 30 keV. Since the mean depth for the highest positron energy (30keV) is about 1150 nm, this energy range is very appropriate for this irradiation condition that produced a damage layer thickness of about 1μm from the surface (fig.2-7). If implanted positron profile were very narrow for each energy of positrons, it could be easily used for the probe of defects in depth direction. In fact, the depth profile of implanted positron was estimated experimentally or with Monte Carlo calculations as follows [2-31];

$$P(x, E) = \frac{m x^{m-1}}{\Gamma} \exp\left[-\left(\frac{x}{\Gamma}\right)^{m}\right] \qquad (2.1)$$

where $P(x, E)$ is normalized positron implanted profile as a function of depth x and incident positron energy E in keV, m is a parameter to be estimated as around 1.9, and Γ is expressed as;

$$\Gamma = \alpha E^{n} / \rho \qquad (2.2)$$

where α and n are parameters to be $\alpha = 4.5 \mu g/cm^2$ and $n = 1.6$, and ρ is density of material. Figure 2-13 shows the implanted profile of positrons calculated from equ. 2-1. The profile is not actually so narrow that the data obtained with a certain incident positron energy comes from broad range of depth. In addition the stopped positrons

move through bulk diffusion, therefore the technique cannot be easily used for the probe of defects in depth direction with the mean depth of each positron energy.

Several methods have been proposed for the analysis of S parameter as a function of incident positron energy [2-17, 2-23, 2-24, 2-27, 2-32]. They commonly assume a single type of defects and three types of annihilation state: surface, bulk and defects. This idea was expressed as the following equation,

$$S(E) = S_s F_s(E) + S_b F_b(E) + S_d F_d(E) \tag{2.3}$$

where subscript s, b and d represent the positron annihilation site, surface, bulk and defect, respectively. $F_S(E)$, $F_b(E)$ and $F_d(E)$ are the fraction of positron annihilating at each site, and S_S, S_b and S_d are characteristic S-parameter for annihilation at each site. Depth profile of implanted positrons ($n(x,E)$) can be expressed as following steady state one-dimensional diffusion equation,

$$D\frac{d^2 n(x,E)}{dx^2} - \lambda_b n(x,E) - \kappa(x) n(x,E) + P(x,E) = 0 \tag{2.4}$$

where D is the diffusion coefficient of positrons, λ_b is the bulk annihilation rate of positrons, $\kappa(x)$ is the positron trapping rate of defects, and $P(x,E)$ is the positron implantation profile. The $\kappa(x)$ is generally proportional to defect concentration $C(x)$. By integrating equation (2), the$F_S(E)$, $F_b(E)$ and $F_d(E)$ can be obtained as follows,

$$F_s(E) = -D\frac{dn(x,E)}{dx}\bigg|_{x=0} \tag{2.5}$$

$$F_b(E) = \int_0^\infty \lambda_b n(x,E)dx \tag{2.6}$$

$$F_d(E) = \int_0^\infty \kappa(x) n(x,E)dx. \tag{2.7}$$

In this study, the program VEPFIT [2-32] was used to analyze the S-E curve. The program is developed by Van Veen et al. in order to extract the relevant parameters from the positron measurements on ion-implanted materials and layered structures. Measurements of the Doppler Broadening parameter S vs. the energy of the incident positrons are analyzed by means of a semi-linear fitting procedure. On solving the problems, it is assumed that $p(x, E)$ and $\kappa(x)$ are slowly varying functions in a given depth interval $[x, x+\Delta x]$ and thus can be taken constant in the interval. As shown in equation (2.3), S parameters for each annihilation process are linear parameters while the others are non-linear parameters. Therefore the semi-linear fitting procedure is employed.

At first, the S-E curve of the unirradiated specimens of each alloy was fitted to obtain the S_b and the bulk diffusion length L_b. S parameter data of low energy positrons below 4 keV are neglected in the fitting of the unirradiated specimens in order to eliminate the effect of epithermal positrons. Then the simplest layered defect profile is assumeed, $C(x)=C$ $(0<x<x_b)$ and $C(x)=0$ $(x_b<x<\infty)$. The C, x_b, S_d , and S_s are determined by fitting under the fixed S_b and L_b. S parameter data of low energy positrons below 1 keV are neglected in the fitting of irradiated specimens for the reason discussed above. The VEPFIT program can also apply the assumption of gaussian defect profile, however some trials revealed that deviation of data from fitting under assumption of gaussian defect profile is larger than the layered defect profile. Gaussian defect profile is more suitable for the case that implanted atoms affect void formation, for example, helium implantation.

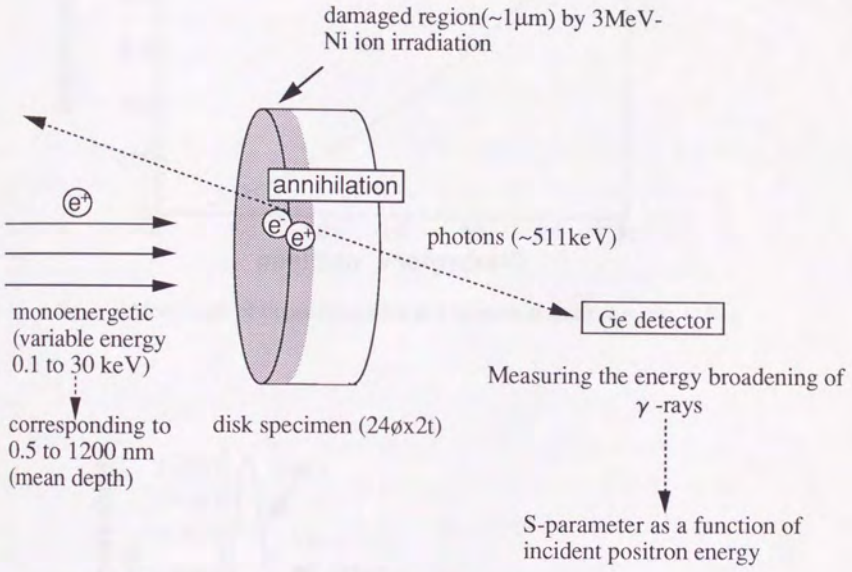

Fig.2-11 A schematic figure of monoenergetic positron beam experiment.

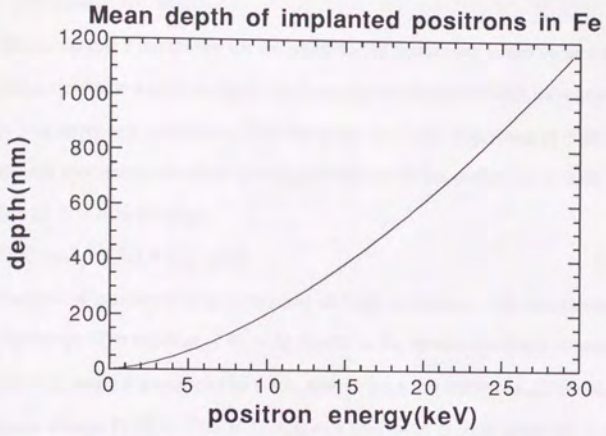

Fig.2-12 Mean depth of stopped positrons as a function of incident energy in Fe

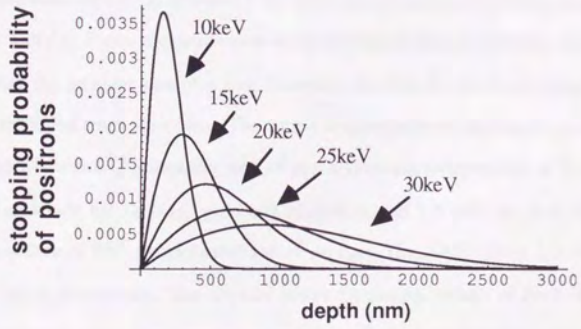

Fig.2-13 Implanted profile of positrons in Fe for various incident energies

2-4. Results

2-4-1 unirradiated specimens

The measured S parameter for the unirradiated specimens is shown as a function of the incident positron energy in fig.2-14. S parameter decreases with increasing positron energy and approach saturation. This behavior is easily explained as follows. In the unirradiated specimens, positron annihilation occurs at the surface or in bulk. Therefore equation (2.3) is simplified as:

$$S(E) = S_s F_s(E) + S_b F_b(E). \qquad (2.8)$$

The fraction of positrons that annihilate in bulk increases with increasing incident positron energy. The relation of $S_S > S_b$ results in the observed energy dependence.

The measured S parameter as a function of positron energy is almost same for all specimens except Fe-0.1C-0.4Cu. It suggests that there is little trapping sites in these specimens except Fe-0.1C-0.4Cu. S parameter of Fe-0.1C-0.4Cu is a little lower than others.

The VEPFIT program can extract the bulk diffusion length of positrons and S_b by fitting of the measured S - E curves for the unirradiated specimens. Fitting parameters are S_b, S_S, and L_b. There is contribution of epithermal positrons diffusing back to the surface when the incident energy is low. Therefore the data for the lower energy below E_{min} are excluded from the fitting. The fitting is done with the various E_{min} and it is determined when fitting parameter and x^2 reach constant independent of E_{min}. It is estimated as 4 keV for Fe-0.1C and Fe-0.1C-0.4Cu, and 1.5 keV for Fe-0.1C-0.4Cu from dependence of fitting parameters and x^2 on E_{min} (fig.2-15). Table 2-3 shows the obtained fitting parameters. The slightly lower S_b and L_b values of Fe-0.1C-0.4Cu indicate that there are some trapping sites in matrix and the trapping sites are not vacancy-type. It is probably due to small copper precipitates formed during furnace cooling from solution annealing. Since the cooling rate is not so slow, precipitates are thought to be smaller than peak hardness condition of 2 nm. It has been reported that small copper precipitates in Fe trap positrons and affect positron lifetime [2-33].

Table 2-3. Fitting parameters calculated with VEPFIT on unirradiated specimens.

	S_s	S_b	bulk diffusion length (nm)
Fe	0.4703	0.4052	136
Fe-0.1C	0.4696	0.4072	134
Fe-0.1C-0.1Cu	0.4701	0.4073	130
Fe-0.1C-0.4Cu	0.4624	0.4057	125
Fe-0.1C-0.7Ni	0.4710	0.4067	128
Fe-0.1C-0.1Cu-0.7Ni	0.4707	0.4068	124

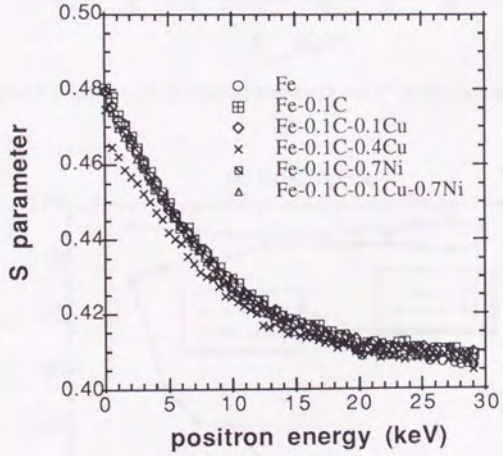

Fig.2-14 Measured S parameter for unirradiated specimens as a function of incident positron energy.

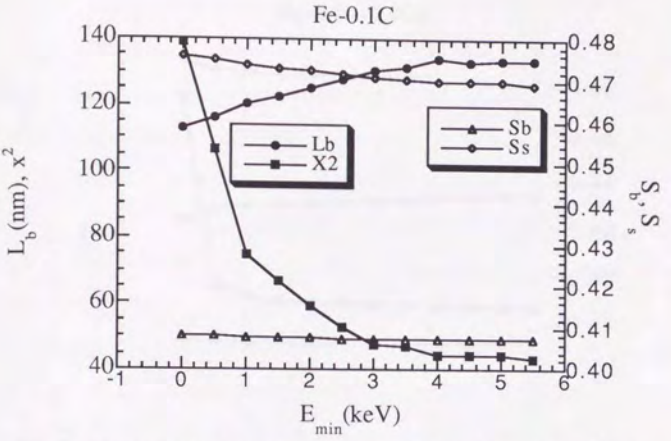

Fig.2-15 Dependence of fitting parameters and x^2 on E_{min}. (a) Fe-0.1C

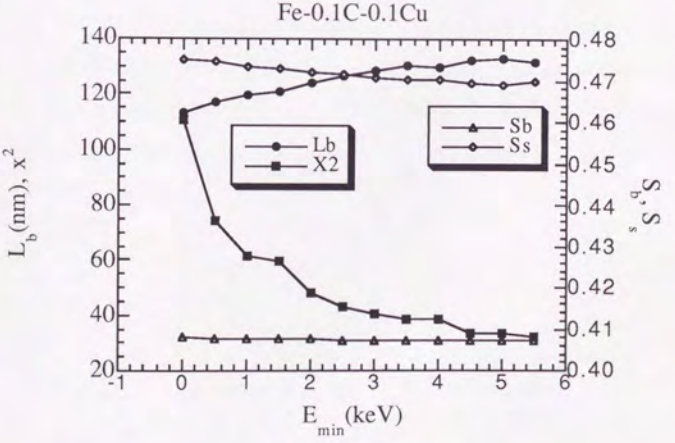

(b) Fe-0.1C-0.1Cu

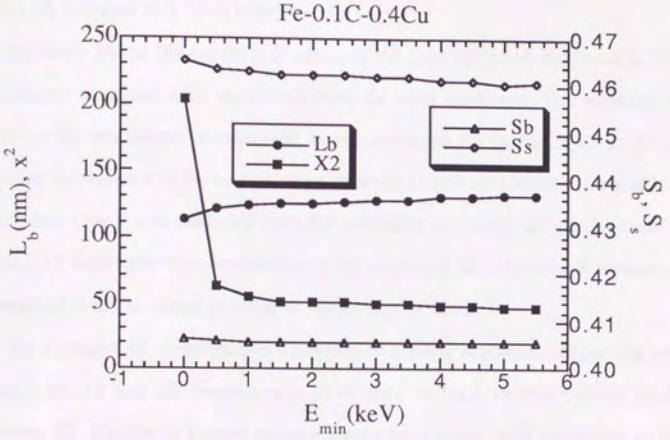
Fe-0.1C-0.4Cu
250
200
150
100
50
0
-1
0
1
2
3
4
5
6
0.47
0.46
0.45
0.44
0.43
0.42
0.41
0.40
Lb
X2
Sb
Ss
L_b(nm), x^2
S_b, S_s
E_{min}(keV)

(c) Fe-0.1C-0.4Cu.

2-4-2 Effect of nickel ion irradiation at 563K

2-4-2-1 ΔS averaged over 15 to 30keV

Figures 2-16a to 16f are the S-E curves of the each specimen irradiated at 563K. S-parameter increases with increasing dose for each specimen. The increase of S parameter by irradiation is estimated as the averaged ΔS in figs.2-17 to 20 with averaging the increase in the energy range between 15 keV and 30 keV. Data of lower energy than 15keV was excluded from the averaging to reduce the effect of surface. Figure 2-17 shows the dose dependence of the averaged ΔS. The dose dependence of averaged ΔS is not so strong as linear or square root of dose.

The averaged ΔS is replotted as a function of content of carbon, copper and nickel in figs.2-18, 19 and 20, respectively. It is seen in fig.2-18 that carbon slightly decreases ΔS. Carbon is known to have strong interaction with vacancies to form carbon-vacancy complexes. Positron lifetime measurement [2-34] shows carbon addition to iron slightly reduces τ_2 compared with pure iron due to carbon-vacancy pair formation and their asymmetric character. The slightly smaller ΔS might be attributed to decoration of vacancy clusters with carbon to reduce apparent free volume of vacancy clusters. The effect of copper content is clearly seen in fig.2-19 to increase the averaged ΔS. Nickel addition to Fe-C increases ΔS for 0.01dpa irradiation, however little effect of nickel addition to Fe-0.1C-0.1Cu is seen in fig.2-20.

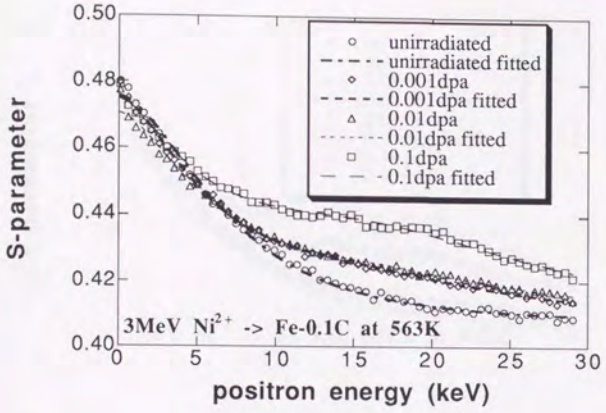

Fig 2-16a S-E curves for Fe-0.1C. Lines are fitting curves calculated with the VEPFIT.

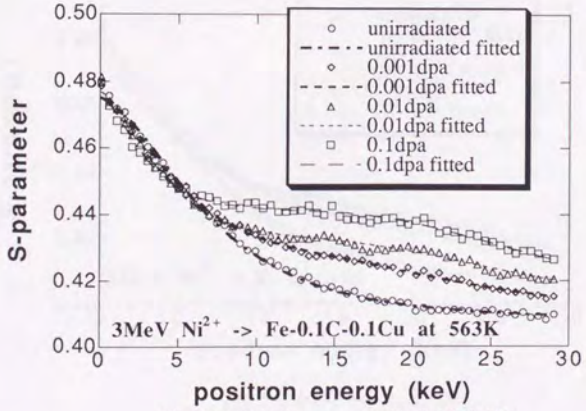

Fig. 2-16b S-E curves for Fe-0.1C-0.1Cu

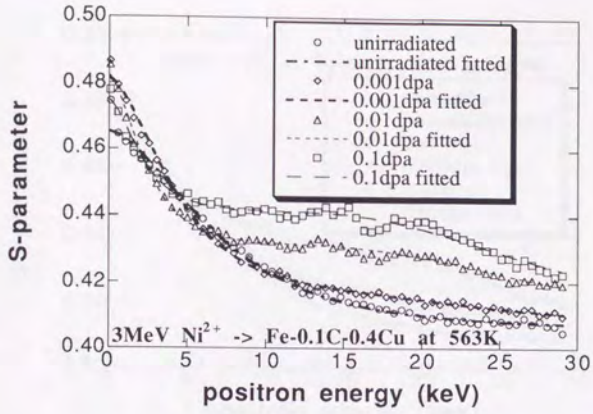

Fig.2-16c S-E curves for Fe-0.1C-0.4Cu

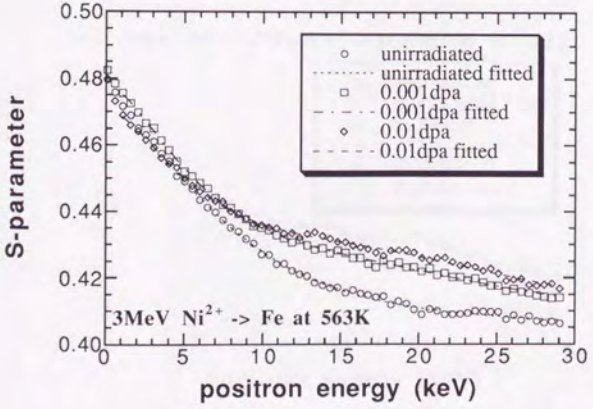

Fig 2-16d S-E curves for Fe

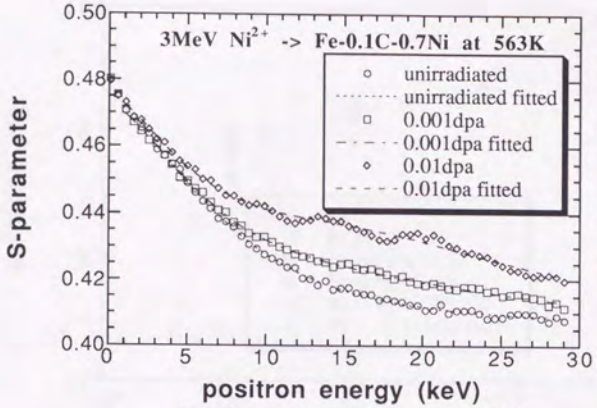

Fig 2-16e S-E curves for Fe-0.1C-0.7Ni

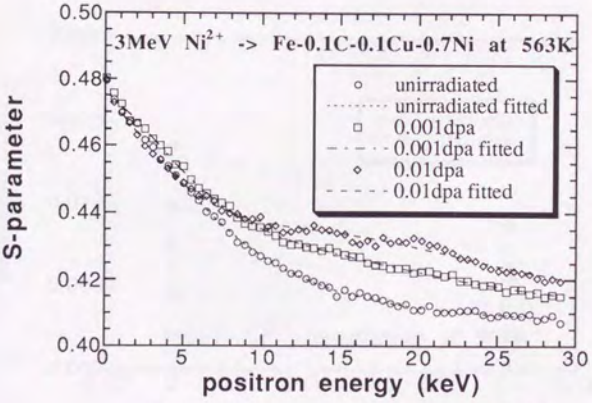

Fig 2-16f S-E curves for Fe-0.1C-0.1Cu-0.7Ni

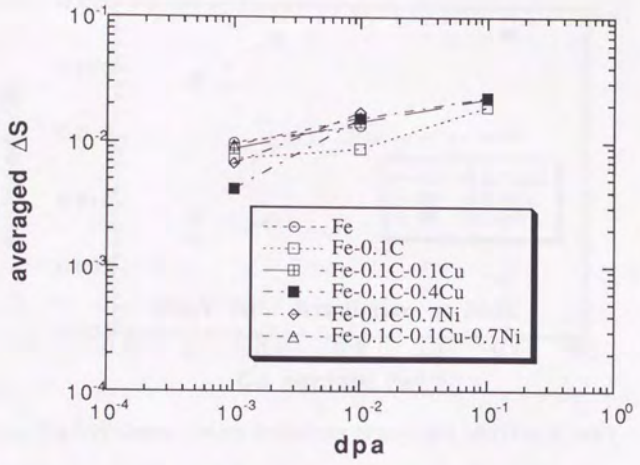

Fig.2-17 Dose dependence of averaged ΔS (15 to 30 keV)

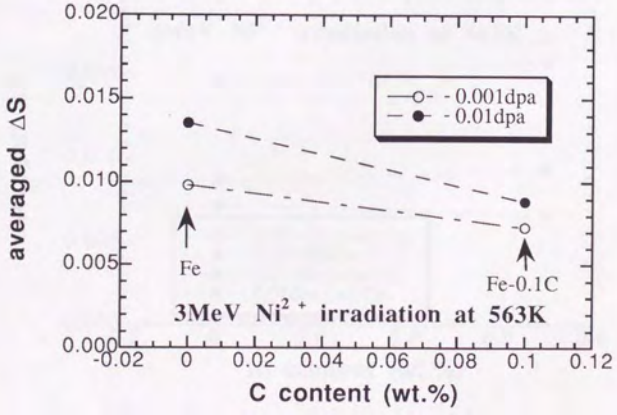

Fig.2-18 Carbon content dependence of averaged ΔS (15 to 30 keV)

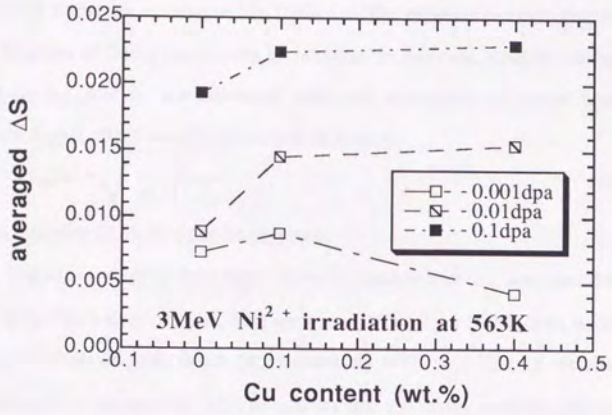

Fig.2-19 Copper content dependence of averaged ΔS (15 to 30 keV)

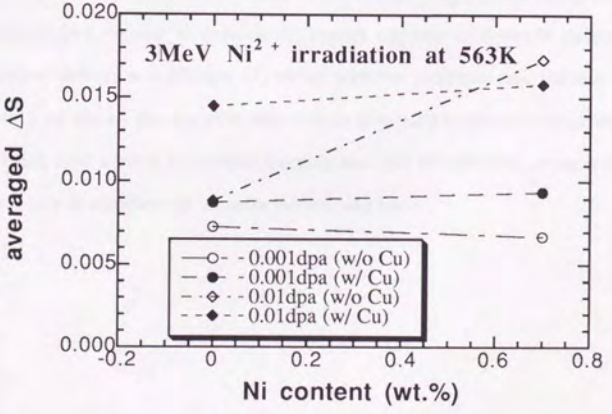

Fig.2-20 Nickel content dependence of averaged ΔS (15 to 30 keV)

2-4-2-2 Insight from VEPFIT calculation

The lines in the figures 2-16a to 16f are the fitting curves by the VEPFIT, and the results of fitting are summarized in Table 2-4. The program can calculate the optimum combination of fitting parameters by iteration. In this case, effective diffusion length L_{eff}, x_b, S_d , and S_s are estimated under the assumption of simple layered defect profile. L_{eff} is effective diffusion length defined as,

$$L_{eff}(x) = \sqrt{\frac{D}{\kappa(x) + \lambda_b}} . \qquad (2.8)$$

From equation (2.8), $\kappa(x)$ can be obtained.

The x_b is the boundary depth between shallower defect zone and deeper defect free zone. The values obtained here are within 750±80 nm (Table 2-4), which is deeper than the damage peak depth (approximately 600 nm). The x_b obtained here is considerably a reasonable value to indicate that the fitting certainly characterizes the surface defect zone.

Figure 2-21 shows $(S_d\text{-}S_b)/S_b$, which is related to the free volume of the trapping sites of the implanted positrons, in other words, increasing S_d/S_b means increase of free volume of each defect. The observed tendencies are; (1) increasing dose leads to increasing free volume of defects, (2) copper addition of 0.4wt.% reduces the free volume of defects at 0.001dpa, (3) nickel addition increases free volume of defects. Figure 2-22 shows the trapping rate, which is related to the concentration of them. Increasing dose leads to increase of trapping rate, and the effect of copper is clearly seen in the figure to significantly increase the trapping rate.

Table 2-4 Summary of VEPFIT results

sample	Fe-0.1C			Fe-0.1C-0.1Cu			Fe-0.1C-0.4Cu		
dpa	0.001	0.01	0.1	0.001	0.01	0.1	0.001	0.01	0.1
S_d	0.4312	0.4348	0.4452	0.4333	0.4348	0.4428	0.4175	0.4313	0.4417
S_s	0.4723	0.4625	0.4728	0.4733	0.4750	0.4715	0.4786	0.4762	0.4696
Boundary(nm)	704	813	725	707	741	742	719	688	678
L_{eff}(nm)	81.9	88.3	57.4	77.1	48.3	34.9	57.4	24.6	22.4
Trapping rate (1/ns)	13.2	10.2	35.0	14.7	49.5	102	29.7	196	238
x^2	43.9	36.3	77.6	48.6	78.4	90.2	46.5	93.9	227.5
S_d/S_b	1.0589	1.0678	1.0933	1.0638	1.0675	1.0872	1.0291	1.0631	1.0887

sample	Fe		Fe-0.1C-0.7Cu		Fe-0.1C-0.1Cu-0.7Ni	
dpa	0.001	0.01	0.001	0.01	0.001	0.01
S_d	0.4347	0.4385	0.4343	0.4453	0.4416	0.4381
S_s	0.4780	0.4711	0.4721	0.4750	0.4741	0.4729
Boundary(nm)	747	768	756	736	707	702
L_{eff}(nm)	85.2	75.1	94.1	65.4	92.4	51.1
Trapping rate (1/ns)	12.3	18.0	6.63	22.2	6.34	38.6
x^2	39.4	55.6	45.9	147.7	48.9	127.7
S_d/S_b	1.0727	1.0820	1.0680	1.0949	1.0854	1.0767

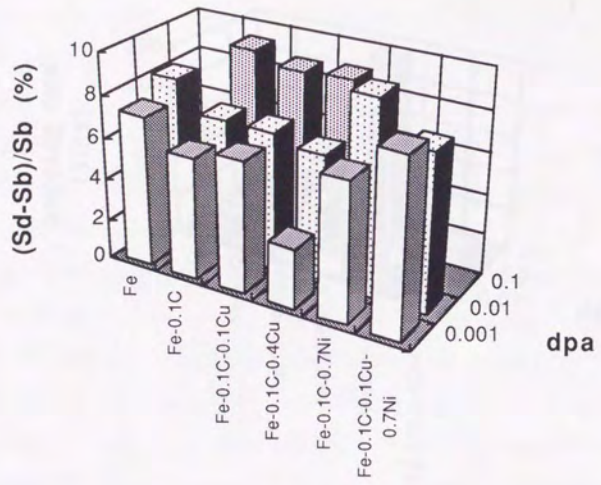

Fig.2-21 Fitted $(S_d\text{-}S_b)/S_b$ for 563K irradiation

(3MeV Ni ion irradiation at 563K)

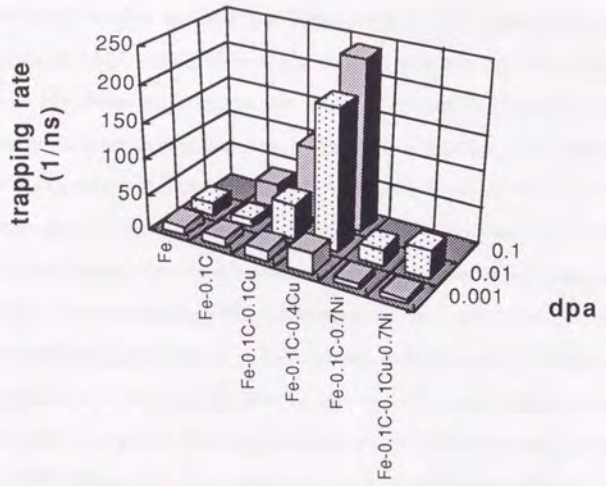

Fig.2-22 Positron trapping rate estimated by VEPFIT

(3MeV Ni ion irradiation at 563K)

2-4-2-3 Vacancy clusters formed in Fe and Fe-0.1C

Figure 2-23 shows the dose dependence of $(S_d\text{-}S_b)/S_b$ and the trapping rate for Fe and Fe-0.1C. The obtained values of S_d are 6 to 9 % higher than S_b for each specimen and dose. It suggests that the trapping sites are vacancy clusters. For comparison, S_d can be estimated to be 7% higher than S_b for neutron irradiated Fe and Fe-C at liquid nitrogen temperature where the longer lifetime component was about 200ps [2-34]. This lifetime value is longer than the value for monovacancies [2-15], indicating that positrons are trapped by not only monovacancies but also vacancy clusters. Therefore vacancy clusters are formed in the present ion irradiation experiment to trap positrons because the S_d/S_b ratio is similar between these experiments. In the literature [2-34],

larger vacancy clusters are formed during isochronal annealing and the vacancy clusters which have longer lifetime component of 350ps make S_d 23% greater than S_b. The lifetime value of 350ps corresponds to vacancy clusters which contain 10 to 15 vacancies [2-15]. From these results, the vacancy clusters produced by the ion irradiation at 563K is not so large and most of them contain less than 10 vacancies. The increase of S_d/S_b ratio with increasing dose indicates growth of vacancy clusters and the growth is more significant between 0.01-0.1dpa than between 0.001-0.01dpa. Vacancy clusters directly form from cascades in matrix. Growth and shrinkage of the vacancy clusters are dominated by balance of point defect flux flowing into vacancy clusters and the thermal emission of vacancies from vacancy clusters. Previous work done by Vehanen et al. [2-11, 2-34] showed that vacancy clusters become unstable around 500-600K in Fe and Fe-C. It suggests that vacancy clusters emit their vacancies thermally at 563K. Biased sink that preferably absorbs interstitials is needed for growth of vacancy clusters through unbalance of point defect flux. There is little biased sinks in unirradiated state, however small dislocation loops (probably interstitial-type) were observed with TEM in Fe-0.1C irradiated to 0.1dpa at 563K (Fig.2-24). It is speculated that the vacancy flux flowing into vacancy clusters exceeds the vacancy emission rate in the dose range due to the bias effect of the dislocation loops formed during irradiation.

Trapping rate is generally expressed as $\kappa = \mu C$ where κ is trapping rate, μ is specific trapping rate into defects and C is defect concentration. When vacancy clusters are considered as trapping defects, the equation is expressed as $\kappa = \mu_{cl} C_{cl}$ where μ_{cl} is specific trapping rate into vacancy clusters and C_{cl} is vacancy cluster concentration. Although there is no experimental data for the specific trapping rate as a function of vacancy cluster size, theoretical calculations by Nieminen et al. show that μ_{cl} is proportional to the number of vacancies in the cluster in the case of small cluster size [2-35]. Therefore total vacancy concentration in vacancy clusters can be estimated by applying μ_V (specific trapping rate into monovacancies, well established) instead of μ_{cl}. [2-11]. Vacancy cluster concentration can be also estimated by dividing the total

vacancy concentration by a number of vacancy in each vacancy cluster. Such calculation shows the total vacancy concentration ranges from several ppm to several tens of ppm in Fe and Fe-0.1C irradiated up to 0.1dpa at 563K. It shows only small fraction of initially introduced vacancies remains surviving in-cascade recombination, matrix recombination and diffusion to sinks.

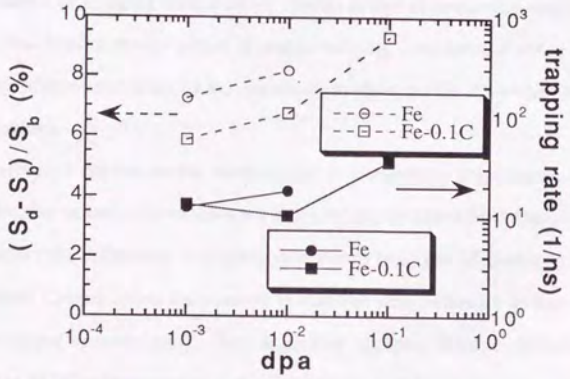

Fig.2-23 Dose dependence of $(S_d-S_b)/S_b$ (blank symbols) and trapping rate (solid symbols) for Fe and Fe-0.1C

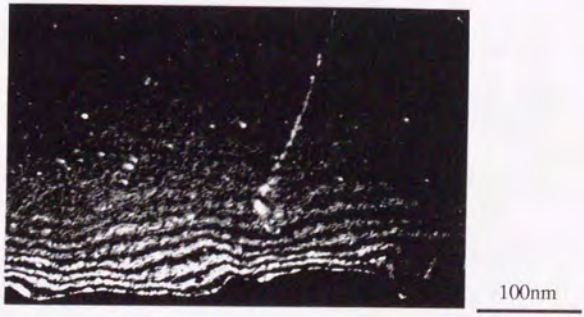

Fig.2-24 TEM images of Fe-0.1C irradiated to 0.1dpa at 563K (Dark field). Bright dot images are thought to be dislocation loops.

2-4-2-4 Effect of copper on vacancy clustering

The effect of copper on vacancy cluster size and number density is shown as a function of dose (fig.2-25) and as a function of copper content (fig.2-26). The effect of copper on vacancy cluster size is significant only for 0.001dpa. Copper addition of 0.4wt% leads to decrease of vacancy cluster size in the case of 0.001dpa. The calculated S_d/S_b ratio is around 3% for this irradiation condition. This small value indicates that the free volume of trapping sites is either similar to that of monovacancies or smaller than that. This implies the formation of copper-vacancy complexes. Further irradiation causes absorption of vacancies by the complexes to show similar open volume to that of no copper alloys.

The effect of copper on the trapping rate is particularly significant at 0.01 and 0.1dpa. The size of each cluster does not seem to vary so much from calculated S_d/S_b ratio, therefore the difference in trapping rate results from the difference in the defect concentration. Copper atoms have strong interaction with vacancies to trap vacancies and form copper-vacancy pairs. They aggregate together through diffusion during irradiation at 563K to form copper-vacancy complexes which contain several vacancies and copper atoms. It is guessed that the complexes have enough free volume to trap positrons and show the estimated S_d/S_b value.

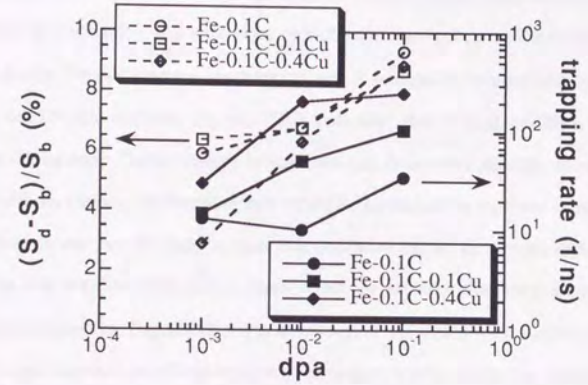

Fig.2-25 Dose dependence of $(S_d-S_b)/S_b$ (blank symbols) and trapping rate (solid symbols) for Fe-0.1C-xCu (x: 0, 0.1 and 0.4 wt.%)

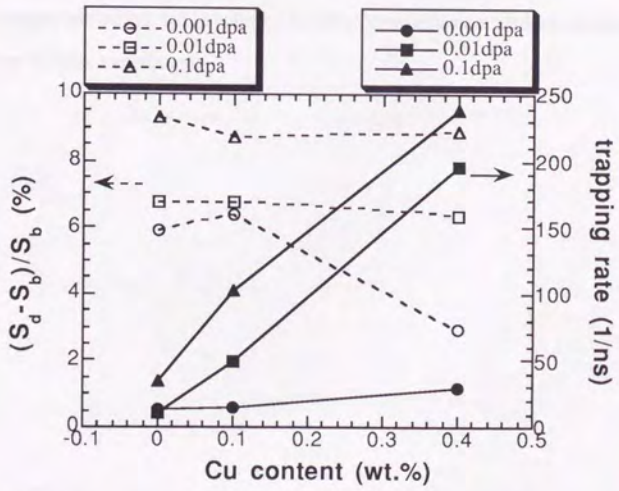

Fig.2-26 Dependence of $(S_d-S_b)/S_b$ and trapping rate on copper content

2-4-2-5 Effect of nickel on vacancy clustering

The effect of nickel is shown in figs.2-27, 28 and 29. Nickel addition increases the S_d/S_b ratio for each alloy and each dose, which indicates increase of volume of each vacancy cluster. On the contrary, the trapping rate is reduced by copper addition except the case of 0.01dpa without copper. This indicates that nickel addition leads to formation of vacancy clusters larger in size and less in number density. Even for the 0.01dpa without copper, the trapping rate might be increased by increase in size rather than increase in number density, because this condition shows the largest difference in S_d/S_b ratio. It is not clear how nickel atoms affect the vacancy clustering. One possible mechanism assumed by Taguchi [2-36] is a removal of vacancies from vicinity of nickel atoms. It might increase the effective vacancy concentration for clustering to result in the enhancement of the unbalance of point defect fluxes. The other possible mechanisms such as stabilizing vacancy cluster by nickel atoms might be given, however one dominant mechanism cannot be specified in this experiment. The synergetic effects between copper and nickel that is believed to enhance radiation embrittlement cannot be clearly seen in these experiments.

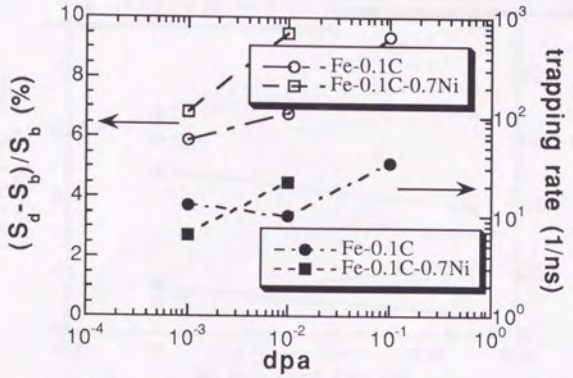

Fig.2-27 Dose dependence of $(S_d-S_b)/S_b$ and trapping rate for Fe-0.1C and Fe-0.1C-0.7Ni

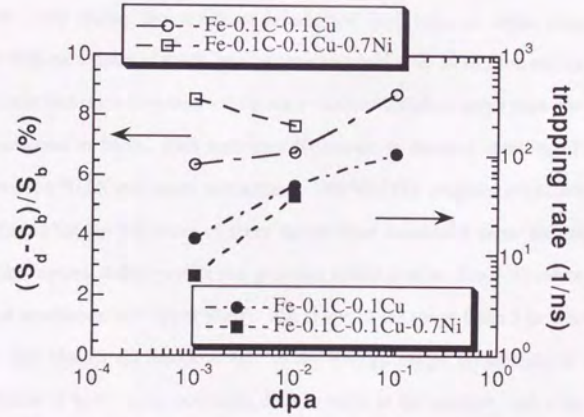

Fig.2-28 Dose dependence of $(S_d-S_b)/S_b$ and trapping rate for Fe-0.1C-0.1Cu and Fe-0.1C-0.1C-0.7Ni

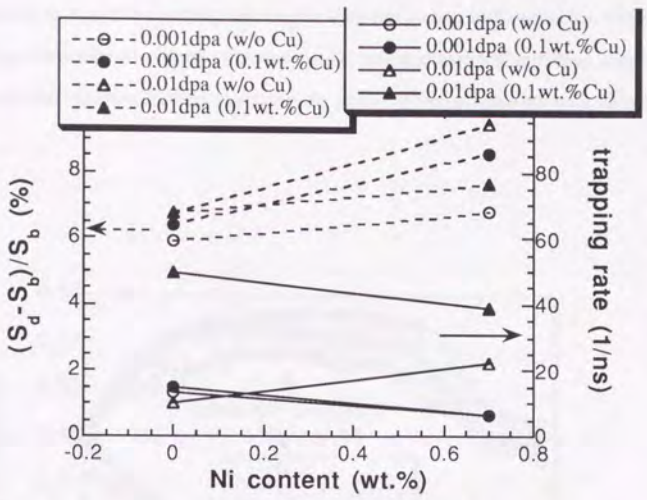

Fig.2-29 Dependence of $(S_d-S_b)/S_b$ and trapping rate on nickel content

2-4-3 Effect of irradiation temperature

Figure 2-30 shows the result of irradiation to 0.1dpa at room temperature. Increment of S-parameter is much greater than irradiation at 563K, and the large value of S-parameter indicates formation of vacancy clusters which is larger than ones formed during irradiation at 563K. This indicates difference in thermal stability of vacancy clusters between 563 K and room temperature. The VEPFIT program could not produce sufficient fitting for the S-E curve of room temperature irradiation under the assumption of neither the layered defect profile nor gaussian defect profile. The *S(E)* curve of room temperature irradiation has 'upper shelf' - like shape in the range from 5 keV to 20 keV. It implies that almost all the positrons in the energy range annihilates at vacancy clusters. Below 5 keV, some positrons diffuse back to the surface, and over 20 keV some positrons annihilate at the deep defect free region. *S(E)* in the upper shelf range nearly equals to S_d, because $F_b = F_s = 0$ and $F_d = 1$ in equation (1). Copper addition apparently decreases S_d and the free volume of vacancy clusters at room temperature

irradiation. It is also due to strong interaction between copper and vacancies. Copper atoms trap vacancies to reduce effective vacancies on clustering and they may be associated with vacancy clusters to reduce the apparent free volume of each vacancy cluster.

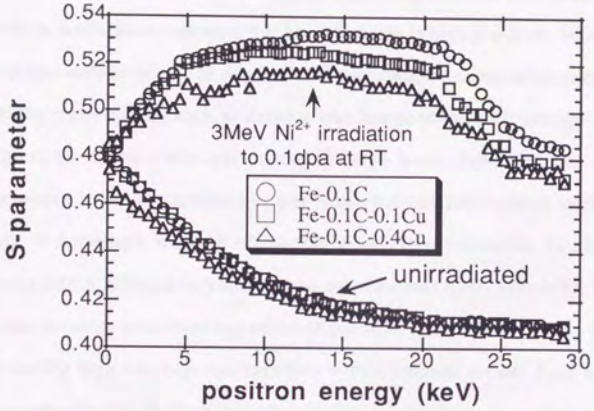

Fig.2-30 S parameter change by 0.1 dpa irradiation at room temperature.

2-5. Discussion on the vacancy cluster formation

It has been widely considered that the radiation embrittlement results from the formation of very fine features that impede dislocation motion. Fine copper precipitates are believed to form during irradiation to cause matrix hardening. The other features than copper precipitates are called "matrix defects" because their nature has not been well characterized.

Since the vacancy cluster is one of the likely matrix defects that cause hardening, the positron annihilation technique that has advantage in high sensitivity for detection of vacancy-type defects is used in this study. The formation process of vacancy clusters is affected by many factors such as damage rate, temperature, sink strength, and so on. Nucleation of vacancy clusters occurs in three ways: homogeneous nucleation, heterogeneous nucleation assisted by gas atoms and cascade-induced nucleation. The first one is encounter reaction of randomly migrating vacancies in matrix. Their nucleation rate is affected by vacancy concentration and their diffusivity. The second one is due to cavity pressurization effect of gas atoms like helium [2-37]. The latter is due to locally high vacancy concentration within cascade region. Such locally high vacancy concentration leads to cascade collapse to form vacancy loops in some metals such as gold [2-38], however, cascade-induced vacancy loops have never been observed in neutron-irradiated iron. The positron annihilation study by Hautojärvi et al. [2-34] showed that clustering of vacancies has already occurred in neutron-irradiated iron at liquid nitrogen temperature. Even below stage III temperature, growth of vacancy clusters occurs by post irradiation isochronal annealing through short range migration of vacancies within and near the cascade region. From these facts, cascade-induced nucleation of vacancy clusters is expected to occur in Fe during the irradiation both at 563K and room temperature. In addition, such high dose rate and low sink strength result in very high vacancy concentration in matrix. It might make the homogeneous nucleation of vacancy clusters more significant than the case of neutron irradiation to practical steels.

In this experiment, a great difference was observed in vacancy cluster size between irradiation at 563K and room temperature. It is due to a difference in thermal stability of vacancy clusters as well as diffusivity of point defects. Intrinsic sinks of point defects are mainly dislocation, grain boundary, and irradiation surface. In these annealed model alloys, the dislocation density is low and the grain size with several tens of μm is larger than the distance from damaged layer to irradiation surface. Therefore it is guessed that the main point defect sink in this experiment is their irradiation surface. Under this assumption the depth distribution and time evolution of vacancies and interstitials are roughly estimated under the present ion irradiation conditions. It considers only generation of monovacancies and single interstitial atoms, their recombination in matrix, and their diffusion to surface sink, and does not consider clustering of point defects and other sinks than surface. The solved equations are:

$$\frac{\partial Cv}{\partial t} = Gv - R\,CiCv - Dv\frac{\partial^2 Cv}{\partial x^2} \tag{2.13}$$

$$\frac{\partial \mathrm{Ci}}{\partial t} = Gi - R\,CiCv - Di\frac{\partial^2 \mathrm{Ci}}{\partial x^2} \tag{2.14}$$

where subscript v and i stand for vacancy and interstitial, respectively, C is concentration, G is generation rate of point defects as a function of depth, R is recombination rate, D is diffusivity, and x is depth from the irradiation surface. G is assumed as tenth of damage rate (damage efficiency equals to 0.1). The results are shown in Fig.2-31 (563K) and Fig.2-32 (room temperature). They show that the depth profile of vacancy concentration is much more different between 563K and room temperature than that of interstitial concentration. At 563K, surface is an effective sink for both vacancies and interstitials in this dose range. At room temperature surface is not an effective sink for vacancies in this dose range while it is an effective sink for interstitials. This difference results in difference in effective number of vacancies for clustering. From this, the difference in the thermal stability of vacancy clusters as well as the mobility of vacancies leads to the great difference in the vacancy cluster evolution between 563K and room temperature.

The effect of copper on the positron trapping rate was very significant. It is guessed that the effect is due to copper-vacancy complex formation. The VEPFIT calculation showed that they have small free volume corresponding to a few vacancies. It might indicate that the complexes are vacancy clusters surrounded by copper atoms. Migration of a copper atom needs a vacancy next to the copper atom to exchange its lattice site. It means that copper necessarily has neighboring vacancy when it jumps to other lattice site. Such diffusion of copper atoms leads to aggregation of copper atoms in matrix. When copper atoms encounter together or come into vacancy clusters and copper-vacancy complexes, the migrating copper atom has a neighboring vacancy. The vacancy might be added to total number of vacancy in the vacancy cluster or the copper-vacancy complex to show the observed S_d/S_b ratio. Akamatsu et al. recently proposed the possibility of cascade-induced copper clustering from the comparison between their neutron and electron irradiation experiments [2-39]. It might be due to the formation of copper-vacancy complexes by copper migration to cascade vacancy clusters. Thus copper vacancy complexes might act as precursors of larger copper cluster or precipitates.

The effect of copper on vacancy clustering at room temperature was seen in this experiment to reduce the volume of each vacancy cluster. It has been believed that copper has little effect on embrittlement at lower temperature at which copper migration and aggregation is not so significant. However this data show that copper has effect on vacancy clustering through strong interaction with vacancies. Therefore the copper effect on matrix defects should be considered through their strong interaction with vacancies in modeling vacancy cluster evolution.

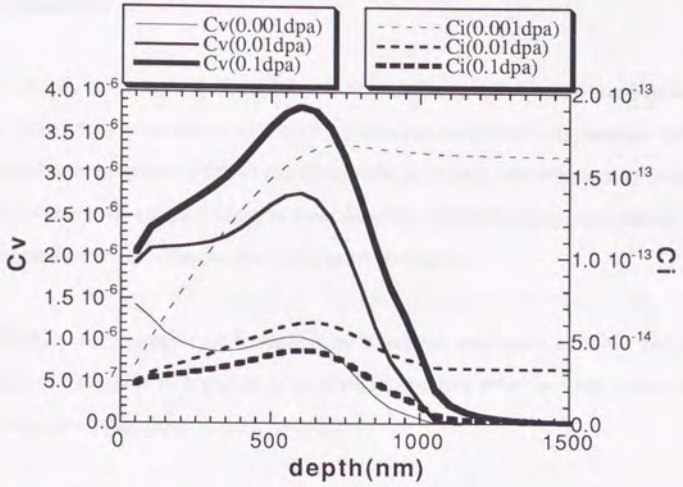

Fig.2-31 Depth profile and evolution of vacancy and interstitial concentration under ion irradiation at 563K. No clustering is considered.

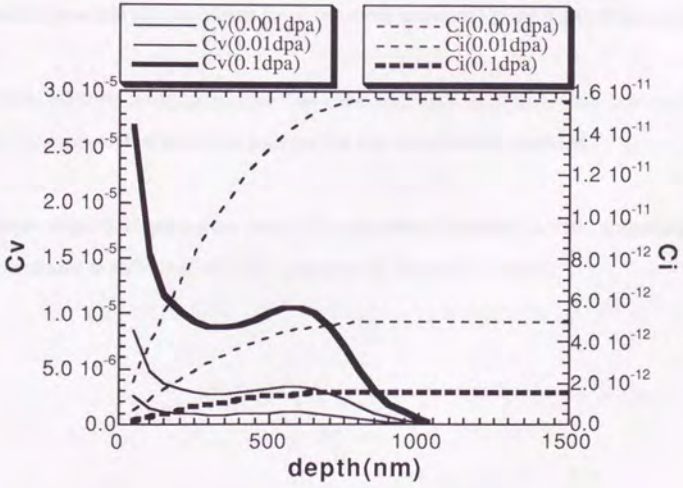

Fig.2-32 Depth profile and evolution of vacancy and interstitial concentration under ion irradiation at room temperature. No clustering is considered.

2-6. Conclusions

Vacancy clustering and effects of irradiation conditions and chemical elements on it were successfully investigated with ion irradiation and variable energy monoenergetic positron beam technique. VEPFIT calculation was done to extract information on size and population of vacancy clusters from incident positron energy dependence of measured S parameter. The obtained insights are as follows:

1) Small vacancy clusters are formed under heavy ion irradiation at 563K, and the number of vacancies in a cluster is estimated to be less than 10. They grow with increasing irradiation dose.

2) Copper content strongly affects positron parameters, particularly trapping rate of positrons. This effect is attributed to formation of copper-vacancy complexes. Its formation occurs in the lower dose range and tends to saturate in the higher dose range.

3) Nickel addition tends to increase free volume of each vacancy cluster. Synergetic effect of copper and nickel was not seen as for this experimental condition.

4) Larger vacancy clusters were detected in specimens irradiated at room temperature than irradiated at 563K, and their free volume was reduced by copper.

2-7. References

2-1 G. R. Odette, P. M. Lombrozo and R. A. Wullaert, ASTM-STP 870 (1985) 840.

2-2 G. R. Odette and G. E. Lucas, ASTM-STP 909 (1986) 206.

2-3 S. B. Fisher and J. T. Buswell, Int. J. Pressure Vessels and Piping, 27 (1987) 91.

2-4 W. J. Phythian, N. De Diego, J. Mace and R. J. McElroy, ASTM-STP 1175, (1993) 462.

2-5 J. T. Buswell, C. A. English, M. G. Hetherington, W. J. Phythian, G. D. W. Smith and G. M. Worrall, ASTM-STP 1046 (1990) 127.

2-6 W. J. Phythian, A. J. E. Foreman, C. A. English, J. T. Buswell, M. Hetherington, K. Roberts and S. Pizzini, ASTM-STP 1127 (1992) 131.

2-7 M. Akamatsu, J. Bourgoin, C. Janot, P. Moser and J. C. Van Duysen, Ann. Chim. France, 16 (1991) p.333.

2-8 J. T. Buswell, C. J. Bolton, M. R. Wootton, P. J. E. Bischler, R. B. Jones, W. J. Phythian and R. N. Sinclair, ASTM-STP 1175 (1993) 332.

2-9 C. L. Gil, A. P. De Lima, N. A. De Campos, J. V. Fernandes, G. Kögel, P. Sperr and D. Pachur, J. Nucl. Mater. 161 (1989) 1.

2-10 G. Brauer, L. Liszkay, B. Molnar and R. Krause, Nucl. Eng. Des. 127 (1991) 47.

2-11 A. Vehanen, P. Hautojärvi, J. Johansson, J. Yli-Kauppila and P. Moser, Phys. Rev. B25 (1982) 762.

2-12 K. Ghazi-Wakili, U. Zimmermann, J. Brunner, P. Tipping, W. B. Waeber and F. Heinrich, Phys. Status Solidi, 102 (1987) 153.

2-13 W. J. Phythian and C. A. English, J. Nucl. Mater., 205 (1993) 162.

2-14 W. J. Phythian, C. A. English and J. T. Buswell, in: Proc. 5th International Symposium on Environmental Degradation of Reactor Materials - Water Reactors, (ANS, La Grange Park, 1991) P.27.

2-15 M. J. Puska and R. M. Nieminen, J. Phys. F13 (1983) 333.

2-16 P. Kirkegaard, M. Eldrup, O. E. Mogensen and N. J. Pedersen, Computer Phys. Communications 23 (1981) 307.

2-17 P. J. Schultz and K. G. Lynn, Rev. Mod. Phys. 60 (1988) 701.

2-18 Yutai Kato, Doctoral Thesis for the University of Tokyo (1994), in Japanese.

2-19 K. Asano, Doctoral Thesis for the University of Tokyo (1989), in Japanese.

2-20 L. M. Davies and T. Ingham, ASTM-STP 909 (1986) 13.

2-21 M. Kiritani, J. Nucl. Mater., 169 (1989) 89.

2-22 C. M. Davisson, and I. Manning, Computer Physics Communications, 42 (1986) 137.

2-23 K. G. Lynn, D. M. Chen, B. Nielsen, R. Pareja and S. Myers, Phys. Rev. B34 (1986) 1449.

2-24 A. Vehanen, Proc. 8th Int. Conf. on Positron Annihilation (1989) 39.

2-25 A. Uedono, S. Tanigawa and H. Sakairi, J. Nucl. Mater. 173 (1990) 307.

2-26 A. Uedono, S. Tanigawa and H. Sakairi, J. Nucl. Mater. 184 (1991) 191.

2-27 T. Aruga, Doctoral Thesis for the University of Tokyo, (1992) in Japanese.

2-28 J. Keinonen, M. Hautala, E. Rauhala, V. Karttunen, A. Kuronen, J. Räisänen, J. Lahtinen, A. Vehanen, E. Punkka and P. Hautojärvi, Phys. Rev. B 37 (1988) 8269.

2-29 W. Trifshäuser and G. Kögel, Phys. Rev. Lett. 48 (1982) 1741.

2-30 W. Long, Master's Thesis for University of Tsukuba, in Japanese.

2-31 S. Valkealahti and R. M. Nieminen, Appl. Phys. A35 (1984) 51.

2-32 A. van Veen, H. Schut, J. de Vries, R. A. Hakvoort and M. R. IJpma, in: Proc. 4th International Workshop on Slow Positron Beams for Solids and Surfaces, (1990).

2-33 W. J. Phythian, N. de Diego, J. Mace and R. J. McElroy, ASTM-STP 1175 (1993) 462.

2-34 P. Hautojärvi, L. Pöllänen, A. Vehanen and J. Yli-Kauppila, J. Nucl. Mater. 114 (1983) 250.

2-35 R. M. Nieminen and J. Laakkonen, Appl. Phys. 20 (1979) 181.

2-36 M. Taguchi, Graduation Thesis for the University of Tokyo (1986), in Japanese.

2-37 L. K. Mansur, J. Nucl. Mater. 216 (1994) 97.

2-38 M. Kiritani, J. Nucl. Mater. 216 (1994) 220.

2-39 M. Akamatsu, J. C. Van Duysen, P. Pareige and P. Auger, presented at 17th Symposium on Effects of Radiation on Materials, Sun Valley, Idaho, June, 1994.

3. Hardening Characteristics of Ion-irradiated Model Alloys

3-1. Introduction

As discussed in Chapter 1, microstructural features formed during irradiation act as obstacles against dislocation movement to result in matrix hardening. The matrix hardening leads to DBTT increase with Ludwig-Davidenkov model, and it is currently regarded as the main contribution to embrittlement. Therefore it is essential to know how microstructural features cause hardening. In addition, hardening trend and the its thermal recovery behavior are expected to provide information on microstructural features that cause hardening.

Hardness measurement has recently been used for study on embrittlement mechanisms by a group of University of California, Santa Barbara (UCSB) [3-1, 3-2]. They prepared many varieties of specimens by changing the chemical compositions, and did irradiation under various conditions such as high, intermediate and low flux, high and low temperature, and many fluences. In addition, they carried out several conditions of post irradiation annealing (PIA). Although their experimental matrix is extremely large more than 1000 conditions, they have been measuring hardness with semi-automated hardness tester developed by them. They proposed four types of defects distinguished with their annealing behavior as Unstable Matrix Defect (UMD), Metastable Matrix Defect (MMD), Stable Matrix Defect (SMD), and Copper Rich Precipitate (CRP). Thus, hardening behavior and their annealing behavior can give insight into microscopic features. However nature of each matrix defect is not still clear.

In this chapter, surface hardening caused by heavy ion irradiation was measured in order to investigate how microstructural features cause hardening and obtain insight into microscopic features through hardening trends and recovery behavior. Fe-C-Cu, Fe-C-Ni and Fe-C-Cu-Ni model alloys were prepared in order to simplify the effect of the elements of copper and nickel. In this study, irradiation was carried out with varied fluence, fixed flux and temperature as the first stage of experiments.

3-2 Experimental

In this study micro Vickers hardness was measured for the estimation of surface hardening of the irradiated specimens. Because the damaged region of samples irradiated with the energetic heavy ions is limited to thin surface layer, low load (0.5g) was employed so that the diamond indentor is not indented too deeply.

3-2-1 Model alloys

The chemical composition of the model alloys investigated is shown in Table 3-1. Fe-0.1C-2.0Ni and Fe-0.1C-0.1Cu-2.0Ni were added to the list of specimen compositions for the positron experiment. All the model alloys were melted by high frequency induction heating in vacuum, hot-rolled, and cold-rolled to 0.2 mm in thickness. The final reduction ratio is 2.5 for each alloys. They were mechanically-polished, punched out in the form of TEM discs of 3 mm in diameter, annealed in vacuum; recrystallization annealing at 1130K for 0.5h followed by solution annealing at 1023K for 1h, and then furnace-cooled. Each of them except Fe has ferrite-pearlite structure and the grain size of ferrite is 10 - 50 μm. They were electropolished finally using the electrolyte of 900 cm^3 acetic acid - 100 cm^3 perchloric acid - 0.5 g chromium trioxide (CrO_3) to present a flat surface. Interstitial impurity (C, N, O) and copper impurity levels were measured for Fe and Fe-0.1C (Table 3-2).

Table-3.1 Chemical composition (wt.%) of the model alloys investigated

	C	Cu	Ni
Fe	< 0.01	<0.01	<0.01
Fe-0.1C	**0.10**	<0.01	<0.01
Fe-0.1C-0.1Cu	**0.09**	**0.11**	<0.01
Fe-0.1C-0.2Cu	**0.10**	**0.20**	<0.01
Fe-0.1C-0.4Cu	**0.10**	**0.38**	<0.01
Fe-0.1C-0.7Ni	**0.11**	<0.01	**0.72**
Fe-0.1C-2.0Ni	**0.10**	<0.01	**2.02**
Fe-0.1C-0.1Cu-0.7Ni	**0.09**	**0.11**	**0.72**
Fe-0.1C-0.1Cu-2.0Ni	**0.10**	**0.11**	**2.05**

Fe : balance

Other elements: Si, Mn, Cr, Mo, V < 0.01

P, S, Sn, As < 0.003

Al, Ti, Nb, Co < 0.005

Table-3.2 Impurity level (wt.%) of Fe and Fe-0.1C measured after final heat treatment.

	C	O	N	Cu
Fe	0.006	0.0074	0.0003	0.001
Fe-0.1C	0.1	0.0049	0.0003	0.001

3-2-2 Ion irradiation

In order to introduce displacement damage, the specimens mentioned above were irradiated with Ni^{3+} ions which were accelerated to 4 MeV by the Tandetron accelerator at HIT. According to the damage profile calculated by E-DEP-1 code, the damaged layer is about 1 μm thick and the damage peak is 0.8 μm deep from the surface (fig.3-1). Displacement per atom (dpa) at the damage peak is used as a scaling parameter of irradiation dose. The damage rate at the damage peak is controlled to be $1x10^{-4}$ dpa/s in this case, greater by the 6 orders of magnitude than that in RPVs. Specimens were irradiated from 0.001 dpa up to 5 dpa at the damage peak in order to obtain data in the wide range of dose, while dpa of the practical pressure vessel steels is estimated to be of the order of 0.1 at the end of plant life.

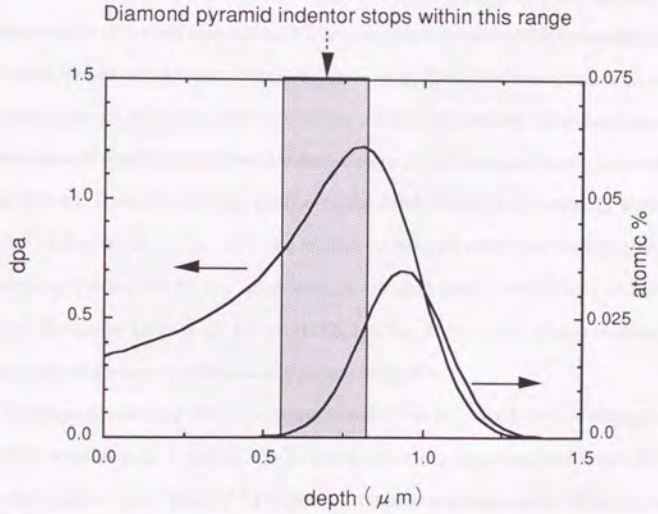

Fig.3-1 Damage profile and range distribution for Fe irradiated with 4 MeV Ni^{3+} to 10^{19} ions/m^2 calculated with EDEP-1 code.

3-2-3 Micro Vickers hardness test employing low load

Micro Vickers hardness test was carried out to obtain data about the radiation hardening caused by ion irradiation. Terazawa's micro hardness tester (MM-II) was used in the air at room temperature. Fig.3-2 shows the photograph of the tester. The load to indentor can be varied by changing the weight on the saucer above the indentor up to 200g. Loading time can be varied up to 75 sec, and it is set to the maximum value through these experiments. As the damage region is only within surface layer of about 1 μm in thickness, micro Vickers hardness test employing low load (0.5 g) was carried out so that the tip of the diamond indentor stops within the damage region. The depth of indentation is 0.57 μm for the hardest sample, 0.81 μm for the softest one as far as this experiment is concerned (Fig.3-1). Grain size of the specimens is larger than the diagonal of diamond traces. So the effect of grain boundary on hardness is avoided when the center region of a grain is indented. Vickers hardness numbers (HV) were determined as the mean values of 5 or more different grains. Apparently abnormal values caused by temporary external vibration such as careless closing of the door were excluded. The hardness data of irradiated samples are the average of the damaged layer. Since the ion energy was constant, the damage profile to the depth direction is probably similar in shape for all dpa levels. So the ΔHV is a relative value but it represents the characteristics of hardening caused by the ion irradiation. Each data point is estimated to have the standard deviation of ± 5 to 10 in HV(0.5g) for 5 or more measurements. The experimental procedure is schematically shown in fig.3-3.

Isochronal annealing after irradiation was done to measure hardness change of the specimens irradiated to 1 dpa at 563 K. Each annealing step was performed for four hours in a vacuum better than 10^{-4} Pa under continuous evacuation with diffusion pump. The duration of 4 h was chosen in order to keep the heating-up and cooling-off periods short compared to the holding period [3-3, 3-4].

Fig.3-2 Micro Vickers hardness tester (MM-II type)

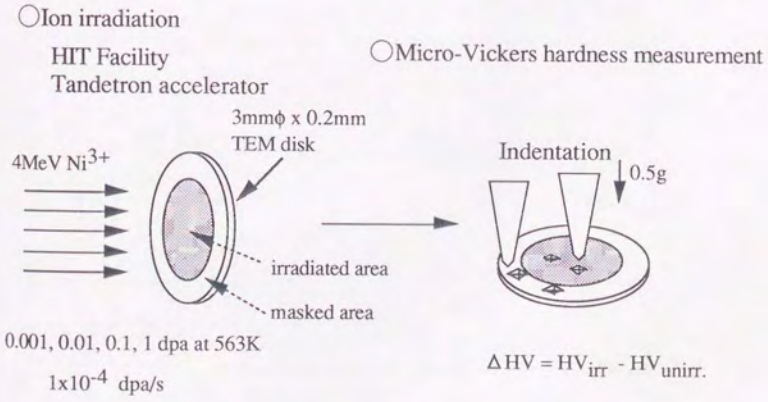

Fig.3-3 Experimental procedure schematically shown

2-4 Transmission electron microscopy (TEM)

TEM observation was carried out for part of the irradiated alloys in order to obtain information about microstructural evolution caused by ion irradiation. Thin foils of the damage peak region were made of irradiated samples. Controlled electropolishing was done to polish out the layer from the irradiated surface to the damage peak region followed by back-thinning using Tenupol-3 for the perforation. The electrolyte was 900 m*l* acetic acid - 100 m*l* perchloric acid - 0.5 g CrO_3 and the polishing voltage during back-thinning is 35 V. There was a difficulty in making a round hole because carbide may fall out to make a corrugated hole. This fact added another difficulty to TEM observation as well as magnetic field caused by ferromagnetic ferrite samples.

3-3 Results

3-3-1 Fe

The radiation hardening caused by the heavy ion irradiation was detectable by micro Vickers hardness test. Figure 3-4 shows the dependence of the irradiation hardening of Fe on dose. The hardness change (ΔHV) on the ordinate is difference between hardness number of the irradiated area and the unirradiated area in the same specimen so that the effect of thermal history is eliminated. It shows the slight hardening at 0.001 to 0.01dpa, and the gradual hardening over this dose range. No saturation trend is observed. Power low fitting ($\Delta HV = k\ (dpa)^n$) was done and the result is also shown in fig.3-4. This function form represents the hardening trend of Ni-ion irradiated iron well and the value of n was estimated to be 0.27.

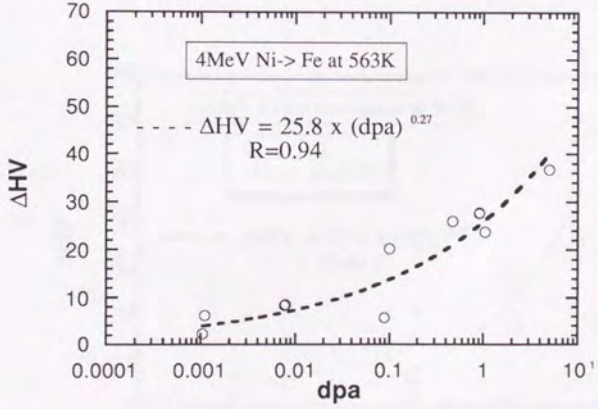

Fig.3-4 Dose dependence of hardening of Fe

3-3-2 Fe-0.1C

The dose dependence of hardening of Fe and Fe-0.1C is shown in fig.3-5. The hardening trends of Fe and Fe-0.1C are similar, so the effect of carbon is not clear. Power low fitting can represent the hardening trends of Fe-0.1C as well as that of Fe. The estimated n value of 0.43 is large compared with 0.27 of Fe, however, the difference in n value seems not to be essential.

Figures 3-6 shows ΔHV change as a function of temperature in isochronal annealing for 4 h for Fe and Fe-0.1C. The hardness change in HV(0.5g) on the ordinate is defined as the difference between hardness number of the irradiated and the unirradiated areas in one sample. The hardening of both samples is gradually recovered and it seems to be completely recovered at 693K.

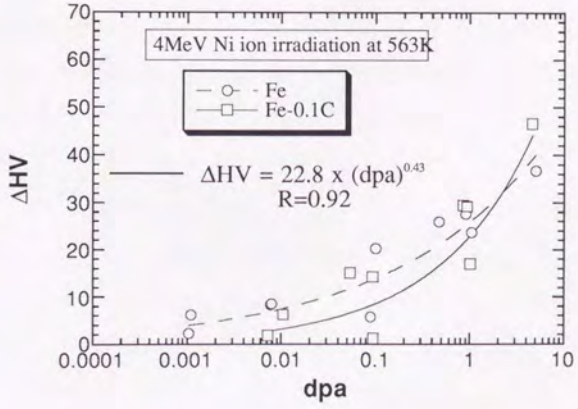

Fig.3-5 Dose dependence of hardening of Fe and Fe-0.1C

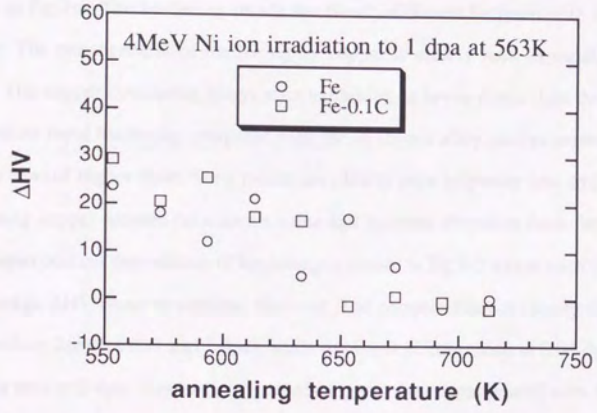

Fig.3-6 Recovery process of radiation hardening of Fe and Fe-C in isochronal annealing for 4 h.

3-3-3 Fe-0.1C-xCu

The dose dependence of hardening of Fe-0.1C-*x*Cu (x: 0, 0.1 and 0.4 wt.%) is shown in fig.3-6. The hardening trends are clearly different between with and without copper. The enhancement of hardening by copper is clearly seen especially in lower doses. The copper containing alloys start hardening at lower doses than the no copper alloy, show rapid hardening compared with the no copper alloy, and saturation tendency is seen toward higher dose. Such trends are clearly seen in power low fitting of data. Increasing copper content decreases n value and increase deviation from fitting curves. The copper content dependence of hardening is shown in fig.3-7 where each data point is the average ΔHV close to nominal fluences. The copper effect is clearly found at the intermediate fluences (0.1 and 1 dpa), while the slight effect is seen at 0.01 dpa and little effect is seen at 5 dpa. This hardening trends suggest the copper related term like $\Delta HV = k\,(dpa)^n + f(Cu, \emptyset t, etc)$.

Figure 3-8 shows the ΔHV change as a function of temperature in isochronal annealing for 4 h for Fe-0.1C, Fe-0.1C-0.1Cu, and Fe-0.1C-0.4Cu. The hardening of Fe-0.1C and Fe-0.1C-0.1Cu is gradually recovered and after 673 K - annealing it seems to be recovered completely. Significant hardening was observed for Fe-0.1C-0.4Cu after annealing at 613 K. The hardening of Fe-0.1C-0.4Cu was not recovered completely even after annealing at 713 K.

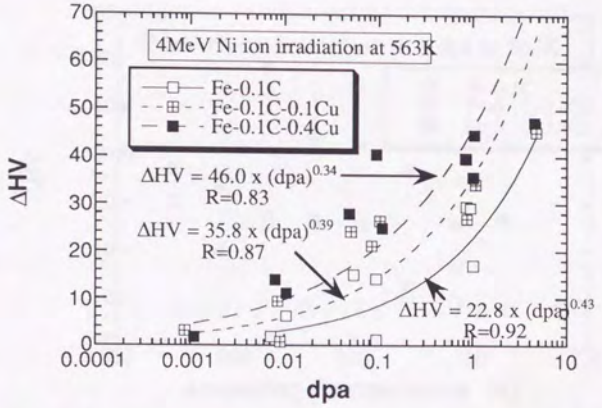

Fig.3-6 Dose dependence of hardening of Fe-0.1C-xCu (x: 0, 0.1, 0.4)

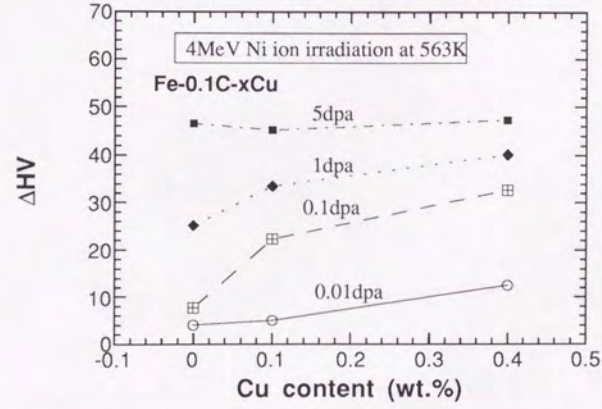

Fig.3-7 Copper content dependence of surface hardening by heavy ion irradiation

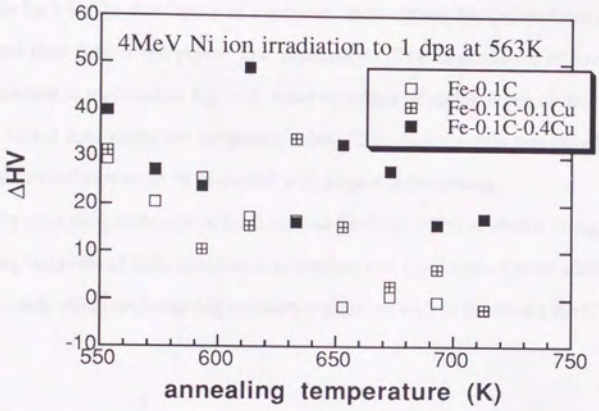

Fig.3-8 Recovery process of radiation hardening of Fe-C-Cu in isochronal annealing

3-3-4 Fe-0.1C-xNi

The dose dependence of hardening of Fe-0.1C-xNi (x: 0, 0.7 and 2.0 wt.%) is shown in fig.3-9. The three types of specimens show almost similar hardening trends on dose, and they follow the power low dependence. The dependence of hardening on nickel content is replotted in fig.3-10, however effect of nickel is not clear. From these results, nickel does not affect hardening solely. This fact suggests that the effect of the implanted nickel atoms can be neglected with respect to hardening.

The annealing behavior of Fe-0.1C and Fe-0.1C-0.7Ni is shown in fig.3-11. The annealing behavior of both specimens is similar, and it indicates nickel addition to Fe-0.1C has little effect on hardening recovery process as well as hardening itself.

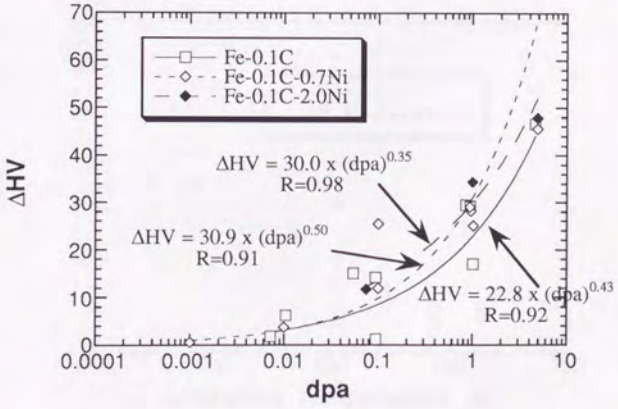

Fig.3-9 Dose dependence of hardening of Fe-0.1C-xNi (x: 0, 0.7, 2.0)

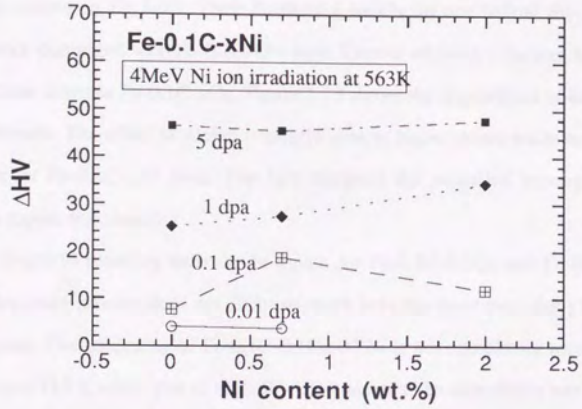

Fig.3-10 Nickel content dependence of surface hardening by heavy ion irradiation

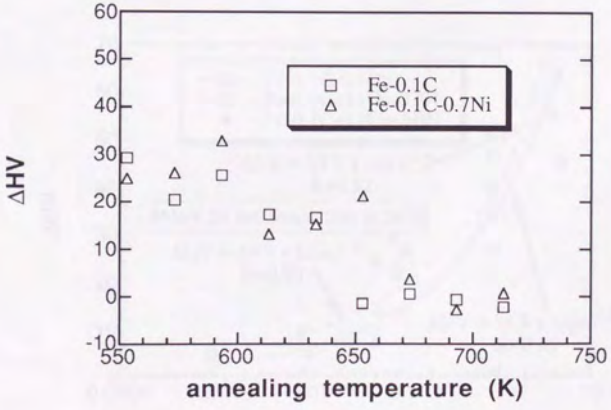

Fig.3-11 Recovery process of radiation hardening of Fe-C-Ni in isochronal annealing

3-3-5 Fe-0.1C-0.1Cu-xNi

The dose dependence of hardening of Fe-0.1C-0.1Cu-xNi (x: 0, 0.7 and 2.0 wt.%) is shown in fig.3-12. Their hardening trends do not follow the power low dependence compared with Fe-0.1C-xNi case. Copper addition enhances hardening at intermediate doses as Fe-0.1C-xCu. Figure 3-13 shows the dependence of hardening on nickel content. The effect of nickel is clearly seen at higher doses while no effect was observed in Fe-0.1C-xNi case. The fact suggests the so-called 'synergetic effect' between copper and nickel.

In Fig.3-14 recovery behavior is shown for Fe-0.1C-0.1Cu and Fe-0.1C-0.1Cu-0.7Ni. Recovery process does not differ so much between these two alloys except high temperature. The hardening of Fe-0.1C-0.1Cu-0.7Ni is not completely recovered after annealing at 713 K while that of Fe-0.1C-0.7Ni seems to be completely recovered after the annealing.

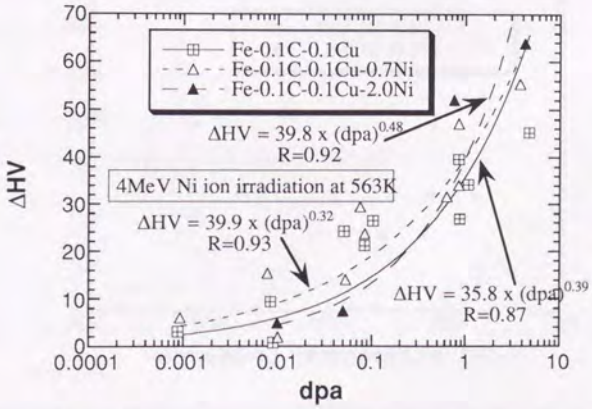

Fig.3-12 Dose dependence of hardening for Fe-0.1C-0.1Cu-xNi (x: 0, 0.7, 2.0)

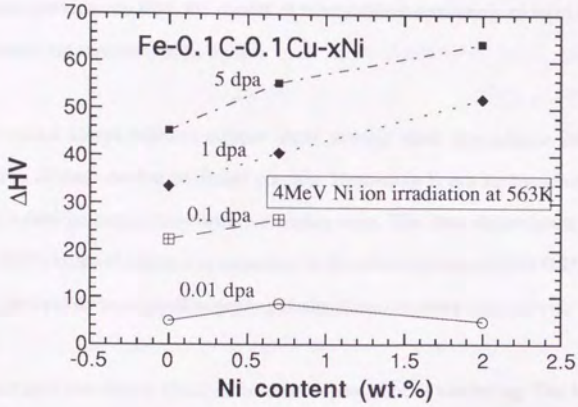

Fig.3-13 Nickel content dependence of surface hardening by heavy ion irradiation

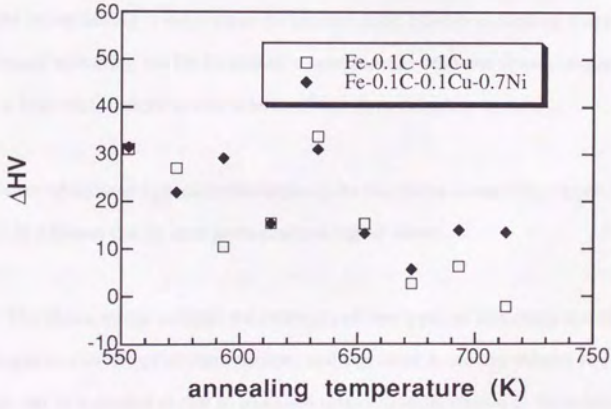

Fig.3-14 Recovery process of radiation hardening of Fe-C-Cu and Fe-C-Cu-Ni in isochronal annealing

3-4 Discussion

In the previous section, the results of the hardness measurement were shown. The overall trends are summarized as below;

(1) The model alloys without copper show similar dose dependence of hardening irrespective of their carbon or nickel content. Hardening is not so significant at lower doses, and then getting greater with increasing dose. The dose dependence follows the form of $\Delta HV=k(dpa)^n$ where n is estimated to be within the range from 0.25 to 0.5. The recovery process by isochronal annealing is also similar among these alloys.

(2) Copper addition clearly changes the dose dependence of hardening. The hardening of the model alloys containing copper shows greater hardening than the alloys without copper particularly at lower doses, and the hardening increases with increasing copper. Then hardening shows saturation tendency at higher doses, and the effect of copper content on hardening is not seen at the highest dose. Further hardening was observed by isochronal annealing for Fe-0.1C-0.4Cu, and the alloy did not show complete recovery even at high temperature at which other alloys show complete recovery.

(3) Nickel addition enhances hardening only for the alloys containing copper. The effect of nickel addition can be seen particularly at higher doses.

The above trends indicate the existence of two types of hardening contribution; one is irrespective of material composition, and the other is clearly related to copper. The former can be regarded as due to so-called matrix defects. Nature of the matrix defects in practical steels has not been understood yet, and "sponges" (vacancy-rich regions), microvoids, dislocation loops (vacancy or interstitial), or solute-point defect clusters

have been regarded as possible features [3-5]. However, for the case of the ion irradiation to the simple model alloys, existence of fine vacancy clusters is revealed in the previous chapter. In addition, TEM observation indicates existence of small dislocation loops (probably interstitial type). Although other possibilities should be taken into consideration, only vacancy clusters and interstitial loops are considered as matrix defects in the discussion below.

From the positron annihilation experiments, vacancy clusters that form during heavy ion irradiation at 563K are estimated to be very small and contain only less than 10 vacancies. Although damage rate ($3x10^{-5}$ dpa/sec for positron annihilation vs. $1x10^{-4}$ dpa/sec for hardness measurement) and ion energy (3MeV for positron annihilation vs. 4MeV for hardness measurement) are different between these experiments, the difference would not result in so different vacancy cluster evolution because PKA spectrum is almost same between these conditions. With respect to vacancy clusters, there must be vacancy clusters in specimens for the hardness measurement although higher vacancy concentration due to higher damage rate may result in larger vacancy clusters. Dot images that are interpreted as dislocation loops were also observed with TEM in specimens irradiated under the same condition as the hardness measurement. These facts indicate that it is reasonable to consider vacancy clusters and dislocation loops as matrix defects in ion-irradiated model alloys.

As shown in 1-4-3, dislocation barrier model has been used to estimate the matrix hardening due to the interstitial and vacancy clusters. It describes the intersection forces of various defects as they impede dislocation motion along the slip plane. There are some models and they are generally derived from Orowan's theory for the athermal bowing of dislocations around obstacles, expressed as:

$$\Delta\tau = \frac{Gb}{\beta\bar{\ell}} \qquad (3.1)$$

where $\Delta\tau$ is the change in shear stress, b is the magnitude of the Burgers vector, $\bar{\ell}$ is the average barrier spacing, G is the shear modulus, and β is a obstacle strengthening factor

[3-6]. The average barrier spacing is computed from the number density, N, and the diameter, d, of the obstacles, $\bar{\ell} = \sqrt{Nd}$. However Friedel [3-7] suggests that dislocations will move past barriers in a zig-zag fashion in the case of weak barriers, and defines an enlarged effective interbarrier spacing to express the change in shear stress as;

$$\Delta\tau = \frac{Gb}{\beta} dN^{2/3} \qquad (3.2)$$

The statistical theory of flow stress shows that Friedel's relation holds over a rather large range of obstacle strength; i.e., up to 1/4 of the Orowan stress [3-8]. Bemont, Jr. summarized various barrier interaction models in Table 3-3. The increment change in shear stress can be related to the change in yield stress change using the Taylor factor in the case of polycrystalline materials as [3-9]

$$\Delta\sigma_y \equiv 3.1\Delta\tau. \qquad (3.3)$$

3-4-1 Hardening due to vacancy clusters

Vacancy cluster evolution was investigated in the previous chapter. The vacancy clusters that formed during heavy ion irradiation at 563K were estimated to contain less than 10 vacancies from the S_d/S_b ratio calculated with VEPFIT. Theoretical calculations by Nieminen and Laakkonen show that specific trapping rate for vacancy clusters, μ_{cl}, is proportional to the number of vacancies in the cluster in the case of small cluster size [3-10]. Therefore, trapping rate $\kappa = \mu_{cl} C_{cl}$ can be expressed as $\kappa = \bar{N}\ \mu_V C_{cl}$ where μ_V is specific trapping rate for monovacancies, C_{cl} is vacancy cluster concentration and $\bar{N}$ is the average number of vacancies in a cluster. Since μ_V is well established to be 1.1×10^{15} sec^{-1} for iron, C_{cl} can be estimated under an assumption of $\bar{N}$ value in the range up to 10 [3-11]. The assumed $\bar{N}$ can be also related to cluster radius r as $\bar{N}\,\Omega_a = 4\pi r^3/3$. Thus obstacle number density, N, and radius, r, can be roughly estimated under an assumption of $\bar{N}$ value within the range up to 10.

Although large voids are known to act as strong barriers [3-12, 3-13], it is not

clear that the small vacancy clusters act as either strong barriers or weak barriers. Then three types of hardening models are examined for the estimation of hardening due to vacancy clusters detected with positron beam. The first one is the strong barrier hardening model (β=1 in equ. (3.1)), the second one is weaker barrier of β=0.1 in equ. (3.1) proposed by Odette et al. [3-1], and the third one is the Friedel's weak barrier model assigned to 6d in Table 3-3. When $\overline{N}$ is set to a certain value, increment change in yield stress can be estimated with the three models and equ. (3.3). Increment change in yield stress are estimated from the positron trapping rate of Fe-0.1C irradiated at 563K in Table 3-4. In addition, rough estimate of the change in Vickers hardness number is done using the empirical proportional constant between ΔHV and $\Delta\sigma_y$ ($\Delta\sigma_y/\Delta HV = 3.5$) in the table. The table shows that the predicted hardening strongly depends on the choice of the hardening models and the strengthening factor, and that the predicted hardening under the strong barrier model is several tens of times higher than the Friedel's weak barrier. The predicted hardening and measured hardening data for Fe-0.1C are plotted together in fig.3-15. Although predicted hardening includes uncertainty in the proportional constant between ΔHV and $\Delta\sigma_y$, and in load dependence of ΔHV, application of the strong barrier model clearly leads to overestimation of hardening. It indicates that the fine vacancy clusters that form during ion irradiation up to 0.1dpa at 563K act as weak barriers against dislocation motions.

Table 3-3. Various models for dislocation barrier interactions [3-6].

Dislocation Networks	Expression for $\Delta\tau$	β	Eq.No.	Ref.
a. Long-range interaction (Frank Network)	$\frac{\mu b}{\beta}\rho^{1/2}$	2π	4a	9
b. Short-range interaction (Trees)	$\frac{\mu b}{\beta}\rho^{1/2}$	~3-4	4b	9
Prismatic Loops				
a. Strong barrier model (after Orowan)	$\frac{\mu b}{\beta \bar{l}}$	~4	5a	10
		~3.7	5b	11
		~2-3	5c	12
b. Weak barrier model (after Friedel)	$\frac{\mu b \cdot d \cdot N^{2/3}}{\beta}$	~8 (b.c.c.)	5d	13
		~4 (f.c.c.)	5e	14
Impurities, Clusters, Precipitates				
a. Strong precipitates	$\frac{\mu b}{\beta \bar{l}}$	~1 (periodic array)	6a	15
		~1.20 (random array)	6b	7
b. Tetragonal distortions	$\frac{\mu C^{1/2}}{\beta}$	~10	6c	16
c. Vacancy clusters	$\frac{\mu b \cdot r_v \cdot N^{2/3}}{\beta}$	~10	6d	17
Voids	$\frac{\mu b}{\beta \bar{l}}\left(\ln\frac{r_v}{r_c}+0.83\right)$	~2π	7a	18
	$\frac{\mu b}{\beta \bar{l}}$	~1	7b	19

τ = shear stress
μ = shear modulus
b = Burgers vector
β = constant
$\bar{l} = (N_i d_i)^{-1/2}$ = average inter-barrier distance

N_i = barrier density
d_i = barrier diameter
ρ = mean dislocation density
C = impurity concentration
r_v = void or vacancy cluster radius
r_c = dislocation core radius

Table 3-4. Predicted hardening due to vacancy clusters detected with positron beam using various hardening models.

		yield stress change						hardness change ($\Delta\sigma_y/3.5$)					
		strong barrier model (ß=1)		weaker barrier model (ß=10)		Friedel's weak barrier model (ß=10)		strong barrier model (ß=1)		weaker barrier model (ß=10)		Friedel's weak barrier model (ß=10)	
dpa	κ (1/ns)	N=5	N=10	N=5	N=10	N=5	N=10	N=5	N=10	N=5	N=10	N=5	N=10
0.001	13.2	396	314	39.6	31.5	6.6	4.2	113	89.9	11.3	9.0	1.9	1.2
0.01	10.2	348	277	34.8	27.7	5.6	3.5	100	79.0	10.0	7.9	1.6	1.0
0.1	35.0	645	512	64.5	51.2	12.7	8.0	184	146	18.4	14.6	3.6	2.3

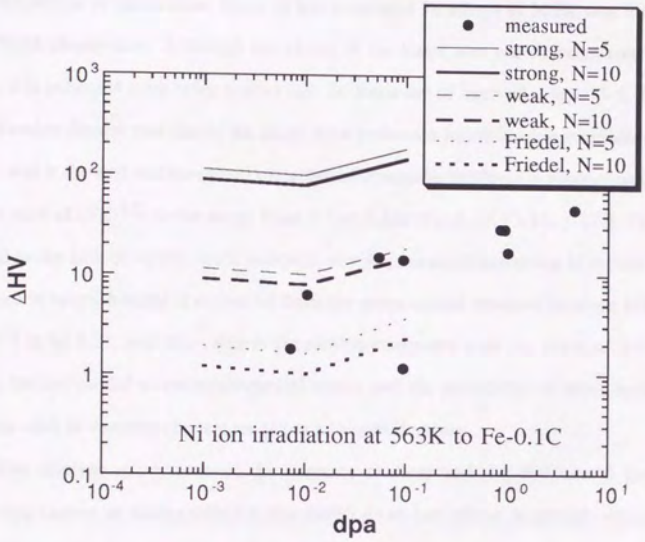

Fig. 3-15 The predicted hardening due to vacancy clusters detected with the positron beam technique and measured hardening data for Fe-0.1C.

3-4-2 Hardening due to dislocation loops

Existence of dislocation loops in ion-irradiated Fe alloys at 563K was indicated with TEM observation. Although the nature of the loops was not characterized in this study, it is indicated from other studies that the loops are of interstitial type [3-5, 3-14, 3-15]. Number density and size of the loops were estimated for nickel-ion irradiated iron at 563K, and it showed that measured incremental change in hardness is proportional to the square root of $(Nd)^{1/2}$ in the range from 0.1 to 5 dpa (fig.3-17, [3-16, 3-17]). This fact as well as the lack of visible voids indicates that the measured hardening is mainly due to dislocation loops. ß value is estimated from the proportional constant between ΔHV and $(Nd)^{1/2}$ to be 5.27, and this value is reasonable compared with the value of 3-4 in the strong barrier model when experimental errors and the possibility of other hardening features such as vacancy clusters are taken into consideration.

The relative importance of the vacancy clusters and the dislocation loops on hardening cannot be distinguished in this study. As shown above, it strongly depends on the hardening models and strengthening factors. Therefore more precise estimation of the hardening models and strengthening factors are required for the prediction of hardening from microstructural information. It will be discussed again in Chapter 4.

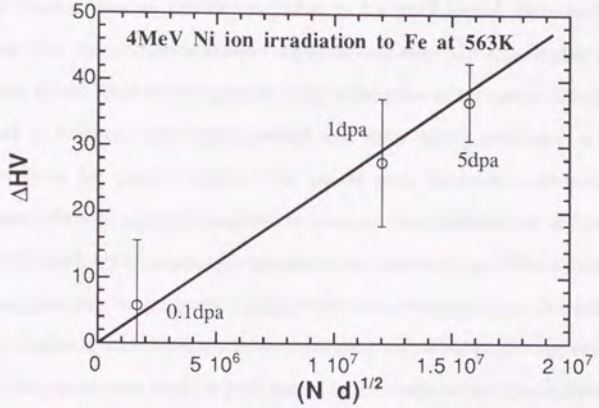

Fig.3-16 Relation between $(Nd)^{1/2}$ and ΔHV where N and d are number density and mean diameter of observed dislocation loops in ion irradiated iron at 563K, respectively [3-16].

3-4-3. Effect of copper

The effect of copper on hardening is significant at relatively low dose range. Since the positron annihilation experiment indicates the formation of copper-vacancy complexes at the low dose range as discussed in Chapter 2, the effect of copper on the hardening can be related to the copper-vacancy complexes. Although such complexes themselves would act as weak barriers with their free volume like small vacancy clusters, the dose dependence of the positron trapping rate shows earlier formation of copper-vacancy complexes than hardening trend. It implies that the copper-vacancy complexes enhance nucleation of stronger barriers like copper clusters rather than act as barriers themselves.

Post irradiation annealing causes the further hardening only for Fe-0.1C-0.4Cu at

613K. Similar radiation anneal hardening (RAH) has been observed in neutron-irradiated model alloys: Takaku et al. [3-18] irradiated Fe, Fe-0.1Cu and Fe-0.3Cu in the Japanese Material Testing Reactor (JMTR) at 523 K to 5 x 10^{18} n/cm^2. Data on isochronal annealing after the irradiation showed the hardening after 573 K annealing for copper containing alloys, similar to the present work in the point of the copper effect. It can be explained as follows; fine copper clusters that form during irradiation at 563K are different from the copper clusters that shows peak hardness condition in aging experiment, either in size, composition, or structure (bcc, twinned 9R or fcc). There is no example that finds fcc copper precipitates in the irradiated iron alloys unlike overaged conditions, and this fact suggests that the irradiation-induced copper clusters are in the 'pre-peak hardness' state. Post irradiation annealing would induce change either in size, composition, or structure to show peak hardness. This experiment cannot distinguish the three types of change, however they can occur simultaneously during annealing. Thus, different annealing behavior due to copper addition also indicates formation of copper clusters.

3-4-4 Effect of nickel and its synergetic effect with copper

Nickel addition to Fe-0.1C seems to have little effect on hardening trend and the recovery behavior. On the contrary, nickel addition to Fe-0.1C-0.1Cu enhances hardening in the higher dose range. This effect is attributed to formation of copper cluster containing nickel at higher doses. Buswell et al. showed that such copper cluster containing nickel form in Fe-Cu-Ni during neutron irradiation at 563K with FEG/STEM attached with EDX while thermal aging induces formation of pure copper clusters [3-19]. They also showed that the hardening of Fe-Cu-Ni is greater than Fe-Cu at relatively higher dose. Our data is consistent with their experiment, and it is reasonable to attribute the nickel effect to the increase in volume fraction of copper-rich clusters by nickel addition to them.

3-5 Conclusions

Surface hardening caused by heavy ion irradiation was measured in order to investigate how microstructural features cause hardening and obtain insight into microscopic features through the hardening trends and the recovery behavior. The results are summarized as;

(1) The model alloys without copper show similar dose dependence of hardening trends irrespective of their carbon or nickel content. Hardening is not so significant at lower doses, and then getting greater with increasing dose. The dose dependence follows the form of $\Delta HV=k(dpa)^n$ where n is estimated to be within the range from 0.25 to 0.5. The recovery process by isochronal annealing is also similar among these alloys.

(2) Copper addition clearly changes the dose dependence of hardening. Hardening of the model alloys containing copper shows greater hardening than the alloys without copper in the dose range between 0.01 and 1 dpa, and the hardening increases with increasing copper. Then hardening shows saturation tendency at higher doses, and the effect of copper content on hardening is not seen at 5 dpa. Further hardening was observed by isochronal annealing for Fe-0.1C-0.4Cu, and the alloy did not show complete recovery even at high temperature at which other alloys show complete recovery.

(3) Nickel addition enhances hardening only for the alloys containing copper. The effect of nickel addition can be found at 1 and 5 dpa.

From the dose dependence and the annealing behavior, hardening features were distinguished to matrix defects and copper clusters. Fine vacancy clusters and interstitial loops are possible matrix defects, however a vacancy cluster acts as a weak barrier

against dislocation motion. Interstitial loops are dominant hardening features in the higher dose range.

Formation of the copper clusters occurs during ion irradiation at 563K, and copper-vacancy complexes proposed in Chapter 2 have possibility of enhancing formation of copper clusters. The copper clusters add nickel atoms at higher doses to show further growth and the resultant hardening.

3-6 References

3-1 G. R. Odette, "Modeling Irradiation Embrittlement in Reactor Pressure Vessel Steels", in *Irradiation Effects in Pressure Vessel Steels*, M. Davies, Ed, Technical Reference Series Publication, International Atomic Energy Agency, Vienna, to be published.

3-2 G. R. Odette, E. V. Mader, G. E. Lucas, W. J. Phythian and C. A. English, ASTM-STP 1175 (1993) 373.

3-3 C. L. Gil, A. P. De Lima, N. A. De Campos, J. V. Fernandes, G. Kögel, P. Sperr and D. Pachur, J. Nucl. Mater. 161 (1989) 1.

3-4 D. Pachur, Nucl. Tech. 59 (1982) 463.

3-5 W. J. Phythian and C. A. English, J. Nucl. Mater. 205 (1993) 162.

3-6 A. L. Bemont, Jr., "Fundamental Materials Problems in Nuclear Reactors", in *Strength of Metals and Alloys*, Proceedings of Second International Conference, Am. Soc. Met., Metals Park, Ohio (1970) 693.

3-7 J. Friedel, in *Electron Microscopy and Strength of Crystals*, p. 605, Interscience, New York (1963).

3-8 U. F. Kocks, in *Physics of Strength and Plasticity*, p.143, MIT press, Cambridge (1969).

3-9 U. F. Kocks, Metall. Trans. 1 (1970) 1121.

3-10 R. M. Nieminen and J. Laakkonen, Appl. Phys. 20 (1979) 181.

3-11 A. Vehanen, P. Hautojärvi, J. Johansson, J. Yli-Kauppila and P. Moser, Phys. Rev. B25 (1982) 762.

3-12 R. W. Weeks, S. R. Pati, M. F. Ashby and P. Barrand, Acta Mett. 17 (1969) 1403.

3-13 P. Coulomb, Acta Met., 7 (1959) 556.

3-14 V. Krishnamoorthy and F. Ebrahimi, presented at MRS Fall meeting, 1988.

3-15 N. Yoshida, H. L. Heinisch, T. Muroga, K. Araki and M. Kiritani, J. Nucl. Mater. 179-181 (1991) 1078.

3-16 Yoshiaki Katoh, Graduation Thesis for the University of Tokyo (1990), in Japanese.

3-17 T. Iwai, H. Kawanishi, Y. Arai, Y. Kato, N. Sekimura and S. Ishino, ASTM-STP 1204 (1993) 228.

3-18 H. Takaku, M. Tokiwai, H. Kayano, Y. Higashiguchi, M. Narui, Y. Suzuki and K. Matsuyama, J. Nucl. Mater. 80 (1979) 57.

3-19 J. T. Buswell, C. A. English, M. G. Hetherington, W. J. Phythian, G. D. W. Smith, and G. M. Worrall, ASTM-STP 1046 (1990) 127.

4. Discussion on physico-based methods for the embrittlement prediction

4-1 Introduction

As discussed in Chapter 1, it is needed to precisely predict the radiation embrittlement of RPV steels. Since the current prediction methods are derived from statistic analysis and do not consider physical meanings, physico-based methods are considered to have possibility to give more precise prediction and higher reliability. In order to establish such a physico-based methods, the embrittlement mechanisms should be fully understood, however they are still unsolved. Many factors such as complexity of material conditions, very fine features below TEM resolution, and poor controllability of irradiation conditions make understanding of embrittlement mechanisms difficult. Therefore full use of knowledge acquired under the different material and irradiation conditions including model alloys and ion irradiation is required for better understanding of embrittlement mechanisms. This concept of correlation among different irradiation conditions based on physical understandings is called 'irradiation correlation', and its importance has been widely recognized. The prediction of radiation embrittlement is a typical case of application of irradiation correlation.

In this chapter, two types of methodology for the embrittlement prediction based on physical understandings are discussed. The first one is based on the fundamental modeling of the embrittlement mechanisms from microstructural evolution through microstructure-mechanical property correlation. It is the ideal, ultimate method, and applicable to the condition out of the data base in principle. However, various physical parameters such as diffusivity of point defects and solutes must be precisely estimated for establishing the prediction. The second one is semi-mechanistic methods pioneered by Odette et al. [4-1, 4-2], Fisher and Buswell [4-3], Simons [4-4], and Taguchi [4-5] in which function forms are derived based on physical understanding and several fitting parameters included in the formula are obtained with statistic analysis. These two methods as well as application of the experiments in this study will be discussed in this chapter.

4-2 Methodology for embrittlement prediction based on modeling of embrittlement mechanisms

In Chapters 2 and 3, the microstructural evolution in the model alloys induced by the heavy ion irradiation was discussed. Existence of fine vacancy clusters was confirmed with positron beam technique, and formation of copper-vacancy complexes was indicated by the VEPFIT analysis of positron data. Moreover, small dot images (~2nm) were observed with TEM in several model alloys irradiated to relatively high doses at 563K and they are believed to be interstitial loops. In addition, the difference in the hardening trend between alloys without copper and alloys with copper suggests the formation of 'copper-related features', believed to be copper clusters, at around 0.1 to 1 dpa. They may form from the copper-vacancy complexes discussed above. Such microstructural evolution is schematically shown in figs.4-1 and 4-2 for the alloys without copper and with copper, respectively. In the following, the modeling of such features and prospect about these features in practical conditions are discussed.

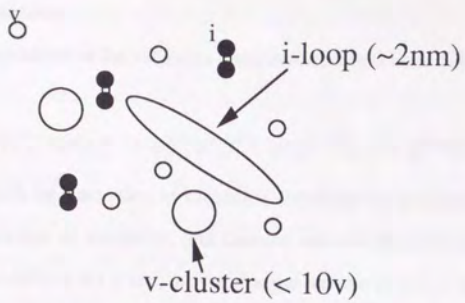

Fig.4-1 A schematic view of microstructure evolution in model alloys without copper induced by nickel ion irradiation at 563K.

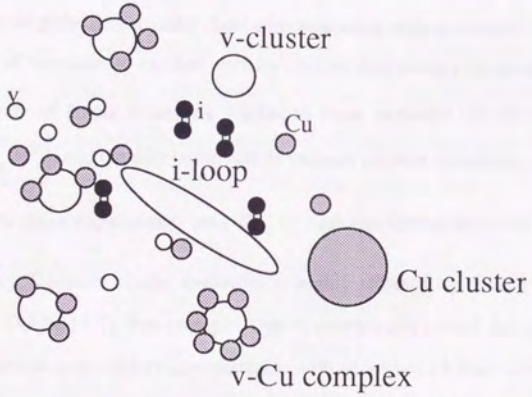

Fig.4-2 A schematic view of microstructure evolution in model alloys with copper induced by nickel ion irradiation at 563K.

4-2-1 Vacancy clustering

General expression of the vacancy cluster evolution was shown as equation (1.3) in Chapter 1 as;

$$\frac{dC_j^{v/icl}}{dt} = \alpha_{v/i,j-1}^{v/icl} C_{j-1}^{v/icl} + (\alpha_{i/v,j+1}^{v/icl} + \psi_{j+1}^{v/icl}) C_{j+1}^{v/icl} - (\alpha_{v/i,j}^{v/icl} + \alpha_{i/v,j}^{v/icl} + \psi_j^{v/icl}) C_j^{v/icl} + G_j^{v/icl} \quad (1.3)$$

It considers growth by absorption of vacancies, shrinkage by absorption of interstitials and thermal emission of vacancies, and cascade-induced nucleation. If vacancy and interstitial concentrations are given, the set of equations can be solved numerically using stiff equation solver such as "GEAR" [4-6]. However, many of physical parameters in the equation are to be established, which might lead to large variation in calculation results.

They include some parameters related to cascade structure or number and configuration of point defects after short term annealing such as cascade efficiency, η, and fraction of vacancies in cascade vacancy clusters containing j vacancies f_j^{vcl}. Then generation rate of freely migrating vacancies from cascades can be expressed as $\eta G_{dpa}\left(1 - \sum_{j=2}^{j_{max}} f_j^{vcl}\right)$, and the generation rate of vacancy clusters containing j vacancies as $\eta G_{dpa} \frac{f_j^{vcl}}{j}$. In these expressions, only G_{dpa} is well established with NRT model, but others are not. Vacancy cluster evolution is highly affected by those parameters as indicated by Odette [4-7]. For example, Odette numerically solved the equation (1.3) under equilibrium point defect concentration with or without 1 barn cross section of generation of cascade vacancy clusters containing 10 vacancies (fig.4-3). The calculation showed that formation of cascade vacancy cluster containing 10 vacancies of 1 barn cross section makes vacancy cluster concentration much higher by about 4 orders of magnitude than the case of no cascade vacancy clusters. Thus, correct knowledge about cascade structure is required for precise estimation of vacancy cluster evolution.

Since cascade structure varies with the PKA energy, these parameters should be functions of PKA energy. Computer simulation studies qualitatively indicate that cascade efficiency, η, is nearly unity for the low PKA energy just above Ed (displacement energy) and it decreases with increasing PKA energy, and that the variation of cascade

efficiency with PKA energy is relatively slow at higher energies [4-8, 4-9, 4-10, 4-11]. The PKA energy dependence of η and f_j^{vcl} is schematically shown in fig.4-3. Recent self ion irradiation experiment for Au shows that monoenergetic PKAs don't form a single type of defect clusters in size and subcascade structure but distribution of size and number in a group [4-12, 4-13, 4-14, 4-15]. It suggests that a PKA of an energy has possibility of making various sizes of vacancy clusters. Therefore if the dependence of f_j^{vcl} on PKA energy are given, f_j^{vcl} of a certain neutron exposure field can be estimated by integrating $f_j^{vcl}(E_{PKA})W(E_{PKA})$ from E_d to E_{PKA}^{max} where $W(E_{PKA})$ is a weighing function that represents the PKA energy spectrum. Since $W(E_{PKA})$ can be obtained for a neutron exposure field using SPECTER code [4-16, 4-17], the dependence of f_j^{vcl} on PKA energy can account for the difference in PKA energy spectrum among various reactors in principle.

Thus f_j^{vcl} is a key parameter for modeling of the vacancy cluster evolution. Computer simulation has potential for the estimation of f_j^{vcl} as a function of PKA energy. Then how can it be experimentally estimated? Self ion irradiation has recently been applied to study on cascade damage structure based on PKA energy with regarding its energy as PKA energy [4-12, 4-13, 4-14, 4-15, 4-18]. These are TEM-base experiments, therefore pure metals with high defect yield such as gold and copper have been examined. As discussed in Chapter 1, self ion irradiation of iron does not form any TEM-visible defects within a cascade region. However, positron annihilation technique can detect TEM-invisible vacancy clusters. Therefore combination of self ion irradiation and positron annihilation technique may be promising. Doppler broadening measurement with variable energy monoenergetic positron beam technique was successfully applied to materials irradiated with MeV-order heavy ions in Chapter 2, however, maximum PKA energy in pressure vessels is ~150keV. Then self ion irradiation should be done with ions of less than 150keV for the application to study on cascade vacancy cluster formation in RPVs to result in defect production very close to surface. This means reduction in the energy range of probe positrons has to be done, and positronium formation at the surface or epithermal positrons must be taken into consideration to make the data interpretation

more complicated. Although self ion irradiation experiment where incident self ions are regarded as monoenergetic PKAs is thus difficult for iron, ion irradiation has capability of making various PKA energy spectra by varying ion species rather than ion energies. In these experiments for cascade vacancy clusters, low temperature irradiation and the following cryo-transfer is desirable for freezing the vacancy structure.

Another unknown parameter that affects the calculation results is effective surface energy of vacancy clusters. This value controls the vacancy emission rate from a vacancy cluster. Odette estimated the sensitivity of calculation results on this parameter, and showed the very large variation of the results with various surface energy (fig.4-4) [4-7]. Positron annihilation technique is the most possible experimental technique for determining the value experimentally due to its high sensitivity for vacancy-type defects. Combination of irradiation and annealing under well controlled conditions is required for it.

The key parameters for description of vacancy cluster evolution and possible techniques for evaluating such parameters are summarized in fig.4-6. Vacancy cluster evolution is very important not only for estimation of its contribution to hardening but also for their effect as sinks of point defects on freely migrating point defect concentration. Therefore detailed studies that determine these key parameters are desired, and the positron annihilation technique has capability for these studies about vacancy clusters. Combination of controlled ion irradiation and the positron beam technique discussed in Chapter 2 is also applicable to such studies.

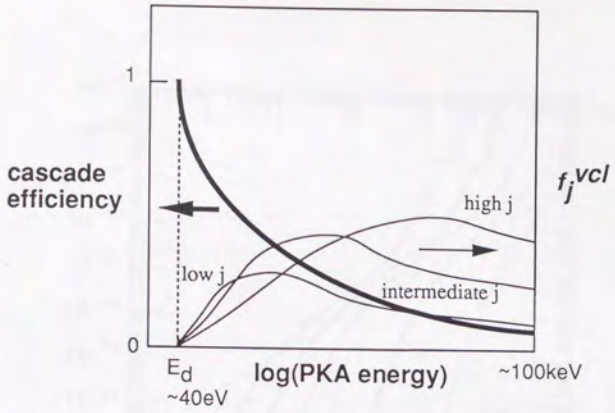

Fig.4-3 A schematic view of PKA energy dependence of η and f_j^{vcl}

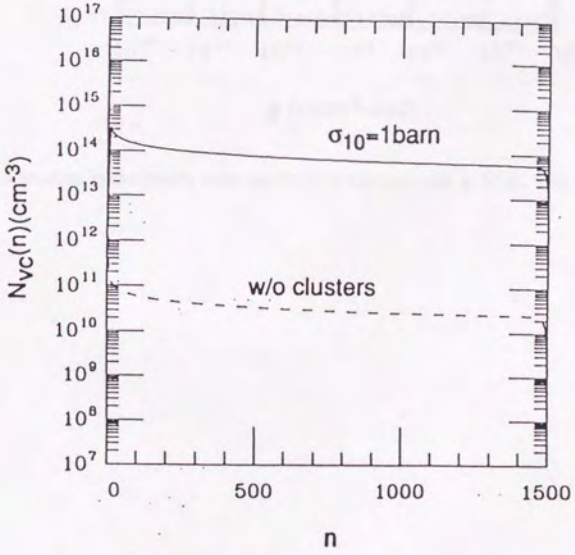

Fig.4-4 Steady-state distributions of vacancy clusters at 563K and a flux of $5x10^{12}$ n/cm^2-s for γ_{eff} =1.2J/m^2, with and without the production (1barn) of 10 vacancy cascade clusters [4-7].

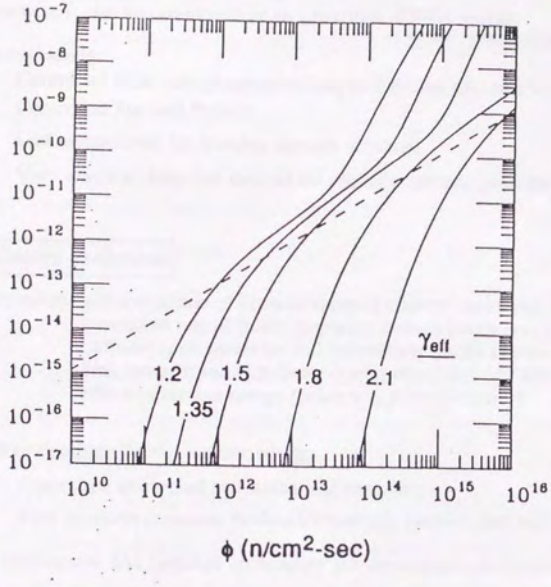

Fig.4-5 Variation in the steady state nanovoid nucleation rate at 563K with flux and γ_{eff}. [4-7]

cascade-vacancy cluster generation

key parameters: size and cross section as a function of PKA energy
→ not well established

For evaluating,

Controlled PKA energy spectrum (use of different ion mass or self ion)

Controlled flux and fluence

Low temperature for freezing damage structure

Very sensitive detection method for vacancy clusters (positron annihilation)

vacancy cluster evolution

key parameters: generation rate of cascade-vacancy clusters (unknown, f(PKA energy, flux))
generation rate of freely migrating defects (unknown, f(PKA energy, flux))
Diffusivity of vacancies and interstitials (partly known, f(temperature))
Sink strength and bias factor (partly detectable and known, f(material conditi
effective surface energy (unknown, f(temperature))

For evaluating effective surface energy,

Controlled isochronal and isothermal annealing

Very sensitive detection method for vacancy clusters (positron annihilation)

Fig.4-6 Key parameters and required techniques for description of vacancy cluster evolution.

4-2-2 Interstitial loop evolution

Interstitial loop evolution is also described by equation (1.3), where the absorption rate and emission rate have different forms from those for vacancy clusters. There are several examples where interstitial loops are observed in iron or iron-based simple systems irradiated to relatively high doses, while no such loops are observed in irradiated practical RPV steels. Although there are few experiments that try to reveal the reason of the difference in interstitial loop evolution between simple iron-based alloys and complex RPV steels, it might be due to difference in impurity levels [4-19]. For example, the fact that more and smaller interstitial loops are observed in Fe-Ni-P than high purity Fe [4-19, 4-20] indicates the importance of alloy and impurity levels. Difference in sink strength might also induce difference in fraction of interstitials available for clustering.

Since any other technique than TEM cannot detect interstitial loops, resolution limit of TEM is the current detection limit for interstitial loops. When interstitial loop evolution in practical steels is considered, extrapolation from 'TEM-visible' condition to the practical 'TEM-invisible' condition. The extrapolation must be done for difference in dose, sink strength, and impurity levels. It is schematically shown in fig.4-7. For realizing such extrapolation, controlled irradiation conditions and well-characterized materials (sink strength and impurity levels) are desired. Ion irradiation can produce visible interstitial loops as shown in Chapter 3, therefore ion irradiation can be applied to such extrapolation work. Then, dose rate effect should be considered in addition to the difference shown in fig.4-7.

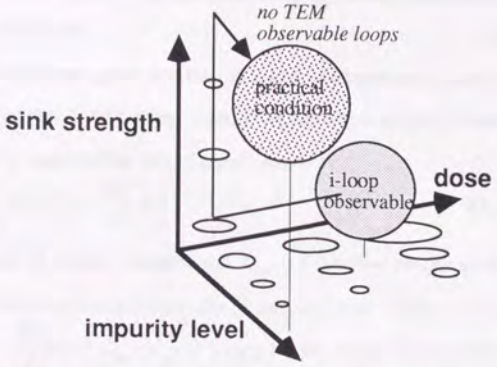

Fig.4-7 A schematic view of comparison between a condition where interstitial loops are observable with TEM and a practical condition where no interstitial loops are observed. Expected loop size trends are also shown. The arrow in the figure is one of the approaches to consider the difference.

4-2-3 Copper clustering

Although any direct evidence of copper clustering cannot be acquired in this experiment, the effect of copper on vacancy clustering is significantly seen in Chapter 2. It indicates the formation of copper-vacancy complexes during irradiation, as schematically shown in fig.4-2. There are several models approaches where copper clustering under irradiation is modeled, and most of them assume rapid homogeneous nucleation and growth of copper clusters accelerated by radiation enhanced diffusion of copper atoms [4-3, 4-7]. On the other hand, Simons assumes that cascade-vacancy clusters stabilized by copper atoms act as nucleation sites of copper clusters and deduces a semi-empirical formula for embrittlement prediction [4-4]. This mechanism is consistent with the present experimental results in the point that it considers interaction between vacancy clusters and copper atoms. Simons' model considers number density, N, of

copper cluster as determined by cascade vacancy cluster formation rate, their annihilation rate by cascade overlapping, and their annihilation rate by thermal emission of vacancies;

$$\dot{N} = \alpha H - \beta G N - \nu N \tag{4.1}$$

where H is vacancy cluster generation rate, G is cascade overlapping rate constant, ν is thermal annihilation rate constant, and α and β are fitting parameters. Size evolution of the copper cluster is controlled by flux of copper atoms as;

$$\frac{dd}{dt} = \frac{4\Omega}{d}\left(D_v C_v C_{Cu} - \frac{\pi d^3}{6} N \right) \tag{4.2}$$

where d is the size of copper clusters, and C_{Cu} is the initial copper concentration in solution. (This equation in that literature may be incorrect with respect to dimension in the bracket, and $\frac{dd}{dt} = \frac{4\Omega}{d} D_v C_v \left(C_{Cu} - \frac{\pi d^3}{6} N \right)$ may be the correct form.) These equations are analytically solved for semi-empirical formula including several fitting parameters and linked to ΔNDTT with Russell-Brown hardening model for copper precipitates in iron matrix [4-21].

This approach is for semi-empirical prediction, so the equations are considerably simplified. In practice, equation (4.1) is appropriate for cascade vacancy cluster formation but may be inappropriate for copper clusters because of the unlikely thermal annihilation term. Thermal emission of vacancies from copper-vacancy complexes leads to formation of copper clusters to act also as hardening features.

For more detailed description of copper-vacancy complex evolution, equation (1.3) can be basically used with some modification. Equation (1.3) is for clustering of a single type of features such as vacancies or interstitials, then $C_j^{v/icl}$ should be substituted with $C_{i,j}^{CuVcl}$ for description of copper-vacancy complex evolution where i and j denote the number of copper atoms and vacancies in a copper-vacancy complex, respectively. The evolution is also controlled by point defect flux and thermal emission of vacancies and Cu-V pair flux, and it is schematically shown in fig.4-8.

Key parameters for the estimation of copper-vacancy complex evolution are radiation enhanced diffusion coefficient, binding energy between a copper atom and a vacancy, vacancy emission rate constant from a cluster, etc. The radiation enhanced

diffusion coefficient is a basic parameter, but it is not well characterized for copper in iron matrix. Specific experiments are required for getting the value (e.g. HVEM). However, since sink strength and irradiation temperature range vary the dependence of diffusion coefficient on vacancy migration energy [4-22], simple extrapolation may be inappropriate. Vacancy emission rate constant from a cluster is not known at all for such copper-vacancy complexes although it may depend on number of copper atoms in a complex as well as its size and temperature. Thus there are still many unknown parameters for modeling copper-vacancy complex evolution. However, this treatment is thought to be more realistic than treating independently vacancy clustering and copper clustering.

There is another possibility that copper-vacancy complexes directly form from cascade during short term annealing. This might enhance nucleation of copper clusters, but there is no direct evidence of it. Computer simulation and low temperature irradiation experiment may give insight about it in the future.

Other elements such as nickel and manganese are also contained in the copper-rich clusters. Fraction and configuration of such elements in a copper rich precipitates varies with irradiation conditions, material conditions, and measurement methods, therefore the mechanism is not systematically understood. Tomographic APFIM is expected to clearly show the fraction and configuration of these atoms in a precipitate, and systematic irradiation experiments should be combined with the technique.

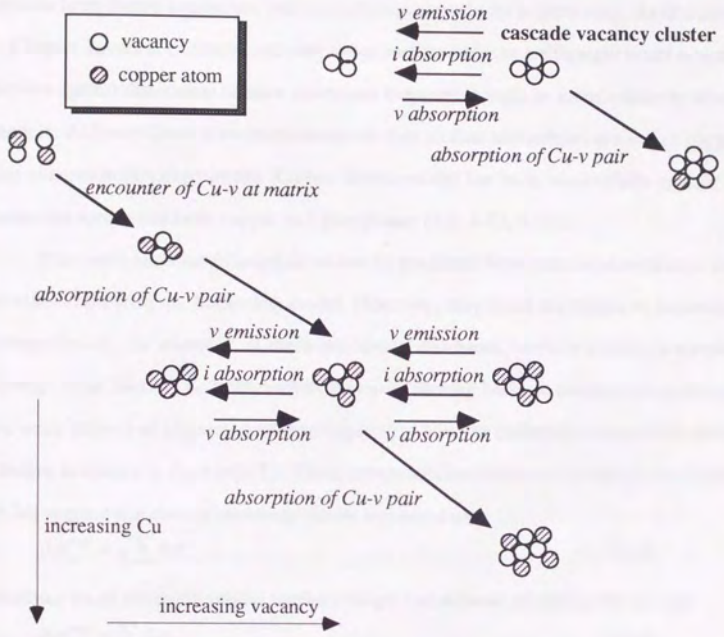

Fig.4-8 A schematic view of copper-vacancy complex evolution

4-2-4 Correlation between microstructural features and mechanical properties

Vacancy clusters, interstitial loops, copper-vacancy complexes and copper rich clusters form during irradiation, and each of them contributes to hardening. As discussed in Chapter 3, vacancy clusters and copper-vacancy complexes are thought to act as weak barriers against dislocation motion. Interstitial loops are thought to act as relatively strong barriers. Although there is no microstructural data on size and number density of copper rich clusters in this experiment, Russell-Brown model has been successfully applied to hardening estimation from copper rich precipitates [4-7, 4-21, 4-23].

Thus each hardening contribution can be predicted from microstructural data to a certain extent with the hardening model. However, they don't contribute to hardening independently, for example, if there are strong and weak barriers similar in number density, weak barriers do little contribution to hardening because dislocations penetrate the weak barriers at a lower stress than required to bow the dislocation around the strong barriers as shown in fig.4-9 [4-7]. Then, computer simulations by Foreman and Makin [4-24] suggest that the net hardening can be expressed as,

$$\Delta\sigma_y^{total} = \sqrt{\sum \Delta\sigma_j^2} \qquad (4.3)$$

for obstacles of relatively similar barrier strength (weak/weak or strong/strong), and

$$\Delta\sigma_y^{total} = \sum \Delta\sigma_j \qquad (4.4)$$

for mixture of many weak barriers and a few strong barriers. Therefore, barrier strength of each features is a very important parameter not only for predicting each hardening contribution but also for selection of the net hardening model. These two cases are typical cases, and superposition model at the intermediate state between equations (4.3) and (4.4) has not been established yet.

The small vacancy clusters are estimated to act as relatively weak barriers (Chapter 3), however, larger voids are known to act as strong barriers [4-25]. It indicates that the barrier strength of vacancy clusters varies with their size. Larger voids might form in RPVs during irradiation at 563K if the end-of-life fluence increases in the future, so the precise evaluation of barrier strength of vacancy clusters is necessary for the

embrittlement prediction based on microstructural evolution. For this purpose, computer simulations or well-designed experiments are desired.

The hardening trends of the model alloys irradiated with Ni ions at 563K are schematically shown in fig.4-10. It shows the matrix defect contribution and the copper-related contribution that is attributed to copper cluster formation. This trend is similar to model prediction by Fisher et al. [4-3] and they treat the decrease in copper contribution with increasing dose as overaging of copper precipitates. However, overaged larger copper precipitates have never been observed in irradiated steels and model alloys. It is generally considered that copper precipitates remain 2~4 nm in diameter during irradiation at 563K. Therefore, the decrease in copper contribution might not be due to overaging but be due to increase of strong barriers such as interstitial loops comparable with copper clusters. This effect makes copper precipitates less effective for hardening like fig.4-9.

As discussed above, predicted hardening value from microstructural features strongly depends on the choice of hardening model and barrier strength value for each microstructural feature and on their superposition model. Studies on such correlation between microstructure and mechanical properties began more than 30 years ago, and the problem is still to be solved. More efforts should be made on this problem using combination of newly developed techniques such as SANS, PA, nano-indentor, etc. for establishing the embrittlement prediction formula fully based on microstructural evolution.

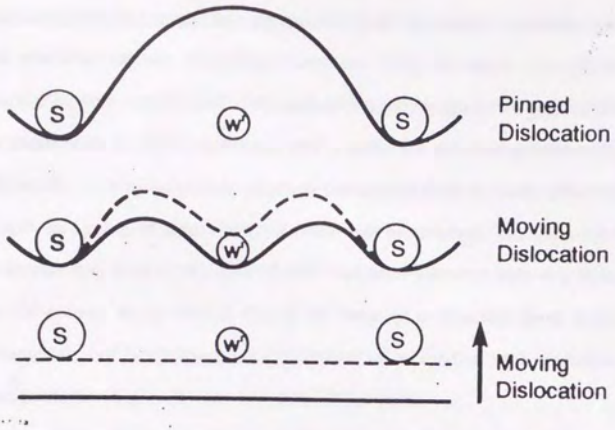

Fig.4-9 A schematic illustration of a dislocation penetrating an approximately equal number of strong and weak dispersed obstacles [4-7].

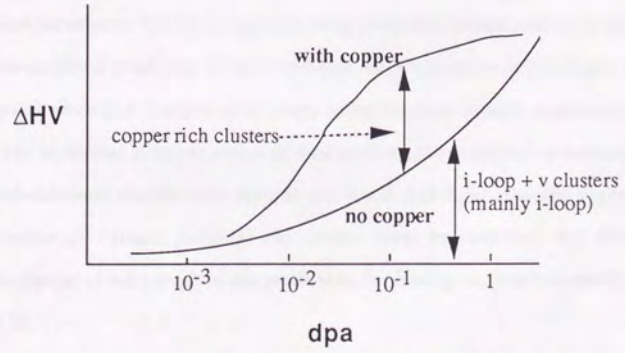

Fig.4-10 A schematic view of dose dependence of ΔHV and two types of contributor to hardening.

4-3 Combination of empirical model and mechanistic model of radiation embrittlement

In the previous section, modeling based on fairly complete description of microstructural evolution is discussed. This method has advantage on its applicability to various conditions even out of the data base, and is useful for preventing from technical surprises. However, it includes various physical parameters from cascade efficiency to barrier strength, and many of them have not been well established. The uncertainty in physical parameter may lead to variation of predicted embrittlement over two orders of magnitudes. Of course, many efforts should be made on evaluating those unknown physical parameters, but fairly complete description of microstructural evolution and embrittlement prediction based on it are still difficult problems.

Then some semi-empirical prediction methods have been proposed by Odette et al., Fisher and Buswell, Simons, and Taguchi [4-1, 4-2, 4-3, 4-4, 4-5]. In the semi-empirical prediction formula, function form is derived from physical understandings, and some fitting parameters are included in them to be determined by statistic analysis. They are more practical than full modeling based prediction, and sometimes give better prediction than fully empirical prediction.

In the present, full mechanistic prediction is still difficult due to many uncertainty in physical parameters. Therefore semi-empirical prediction should become an alternative to current empirical prediction in the near future when it predicts embrittlement better than empirical prediction. Further mechanistic understandings as well as enrichment of data base can be applied to improvement of these semi-empirical prediction methods. So study on embrittlement mechanisms must be continued, and highly specific experiments for evaluation of various physical parameters must be designed and done for the establishment of fully mechanistic prediction, the ideal goal, as schematically shown in fig.4-11.

There should be at least two kinds of contribution to hardening within this study. As discussed above, matrix defect contribution seems to come from vacancy clusters and interstitial loops. Rate equation calculation by Stoller suggests that their dose dependence shows $(\phi t)^n$ (n~1/2) until it reaches a saturation level [4-26, 4-27]. The dose dependence

is consistent with the hardening results (Chapter 3). His calculation also shows increasing flux accelerates hardening by the clusters. Although this flux effect is not confirmed in this experiment, ion irradiation experiment can be used for confirmation of such an effect. In this way, function form of semi-empirical prediction can be improved with theoretical calculation and appropriate experiments.

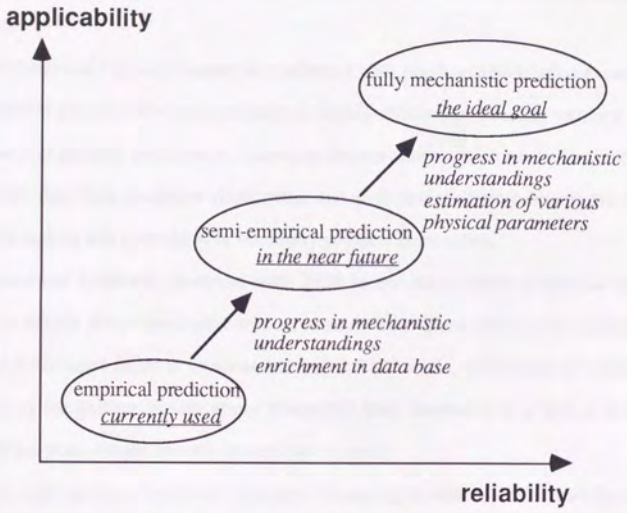

Fig.4-11 Future prospective of prediction method of radiation embrittlement

4-4 Conclusions

The combination of positron annihilation, TEM and hardness measurement of the model alloys irradiated with the heavy ion suggests that the microstructural features that form during ion irradiation at 563K are vacancy clusters, interstitial loops, copper-vacancy complexes, and copper rich clusters. Their evolution process can be basically expressed as the cluster equation (equation (1.3)). The ideal way to establish mechanistic prediction is to solve the equation to estimate the size and number density of them under the interested irradiation condition and material condition, and convert them to mechanical properties.

Formation of vacancy clusters is confirmed with positron annihilation experiment. The evolution process of vacancy clusters is highly affected by cascade vacancy cluster formation and thermal emission of vacancies from a cluster. Both of them are not fully understood, therefore computer simulations and well-designed experiments are desired for understanding and estimation of necessary physical parameters.

Interstitial loops are observed with TEM in this experiment as well as in other studies on simple alloys irradiated with neutron or ions. Since there is no example that observed dislocation loops in irradiated complex RPV steels, well-designed experiment are required for getting insight about interstitial loop evolution in practical steels by extrapolation from simple systems to complex systems.

Although no direct evidence of copper clustering is obtained in this study, copper affects hardening trends and positron parameters. Copper-vacancy complexes are thought to form, and it is possible for them to act as precursors of copper rich clusters. Therefore vacancy clustering evolution should be expanded to copper-vacancy clustering evolution. Anyway, many parameters remain unknown.

Since there are many unknown parameters that affect clustering evolution as well as uncertainty in barrier strength and appropriate hardening superposition model, fully mechanistic prediction is currently impractical. Semi-empirical prediction should be an alternative to the current empirical method, and well-designed, specific experiments are

needed for further mechanistic understandings and evaluation of various physical parameters.

4-5 References

4-1 G. R. Odette, P. M. Lombrozo, J. F. Perrin and R. A. Wullaert, in *Physically Based Regression Correlations of Embrittlement Data From Reactor Pressure Vessel Surveillance Programs*, EPRI NP-3319 (1984).

4-2 G. R. Odette and G. E. Lucas, in *Irradiation Embrittlement of LWR Pressure Vessel Steels*, EPRI NP-6114 (1989).

4-3 S. B. Fisher and J. T. Buswell, Int. J. Pres. Ves. & Piping, 27 (1987) 91.

4-4 R. L. Simons, ASTM STP 956 (1987) 535.

4-5 M. Taguchi, graduation thesis for University of Tokyo (1986), in Japanese.

4-6 A. C. Hindamarsh, Signum, Newsletter of the ACM, 15 (1980).

4-7 G. R. Odette, "Modeling Irradiation Embrittlement in Reactor Pressure Vessel Steels", in *Irradiation Effects in Pressure Vessel Steels*, M. Davies, Ed, Technical Reference Series Publication, International Atomic Energy Agency, Vienna, to be published.

4-8 T. Diaz de la Rubia and M. W. Guinan, J. Nucl. Mater. 174 (1990) 151.

4-9 C. A. English, W. J. Phythian, and A. J. E. Foreman, J. Nucl. Mater. 174 (1990) 135.

4-10 C. A. English, A. J. E. Foreman, W. J. Phythian, D. J. Bacon and M. L. Jenkins, Materials Science Forum 97-99 (1992) 1.

4-11 T. Diaz de la Rubia and M. W. Guinan, Materials Science Forum 97-99 (1992) 22.

4-12 M. Kiritani, M. Hoshino, H. Kato, H. Matsui and N. Matsunami, J. Nucl. Mater. 191-194 (1992) 1128.

4-13 Y. Kanzaki, master's thesis for University of Tokyo, (1993), in Japanese.

4-14 T. Masuda, graduation thesis for University of Tokyo, (1993), in Japanese.

4-15 N. Sekimura, Y. Kanzaki, S. R. Okada, T. Masuda and S. Ishino, J. Nucl. Mater. 212-215 (1993) 160.

4-16 L. R. Greenwood and R. K. Smither, in *SPECTER: Neutron Damage Calculations for Materials Irradiations*, ANL/FPP-TM-197 (1985).

4-17 L. R. Greenwood, J. Nucl. Mater. 216 (1994) 29.

4-18 M. Kiritani, J. Nucl. Mater. 216 (1994) 220.

4-19 W. J. Phythian and C. A. English, J. Nucl. Mater. 205 (1993) 162.

4-20 V. Krishnamoorthy and F. Ebrahimi, presented at MRS Fall meeting, 1988.

4-21 K. C. Russell and L. M. Brown, Acta Metall. 20 (1972) 969.

4-22 N. Lam and S. J. Rothman, in *Radiation Damage in Metals*, ed. by N. L. Peterson and S. D. Harkness, ASM, (1976) 125.

4-23 W. J. Phythian, A. J. E. Foreman, C. A. English, J. T. Buswell, M. Hetherington, K. Roberts and S. Pizzini, ASTM-STP 1127 (1992) 131.

4-24 A. J. E. Foreman and M. J. Makin, Can. J. Phys., 45 (1967) 511.

4-25 A. L. Bemont, Jr., "Fundamental Materials Problems in Nuclear Reactors", in *Strength of Metals and Alloys*, Proceedings of Second International Conference, Am. Soc. Met., Metals Park, Ohio (1970) 693.

4-26 R. E. Stoller, in *Modeling the Influence of Irradiation Temperature and Displacement Rate on Radiation-Induced hardening in Ferritic Steels*, NUREG/CR-5859 ORNL/TM-12073 U.S. Nuclear Regulatory Commission, Washington D.C. (1992).

4-27 R. E. Stoller, ASTM-STP 1175 (1993) 394.

5. Concluding Remarks

In this study, the mechanisms of the radiation embrittlement are investigated using the ion irradiation and the model alloys. Application of variable-energy positron beam technique to study on the embrittlement mechanisms is originally attempted, and, TEM and hardness measurement are also carried out for the irradiated specimens.

Vacancy clustering and effects of irradiation conditions and chemical elements on it were successfully investigated with the ion irradiation and the variable energy monoenergetic positron beam technique. The VEPFIT calculation was done to extract information on size and population of vacancy clusters from incident positron energy dependence of measured S parameter. Surface hardening caused by heavy ion irradiation was measured in order to investigate how microstructural features cause hardening and acquire information on microscopic features through hardening trends and recovery behavior. The obtained insights are summarized below.

Matrix defects:

1) Small vacancy clusters form under heavy ion irradiation at 563K, and the number of vacancies in a cluster is estimated to be less than 10. They grow with increasing irradiation dose. They are thought to act as weak obstacles against dislocation motions rather than strong obstacles such as large voids. Nickel addition tends to increase free volume of each vacancy cluster. Larger vacancy clusters were detected in specimens irradiated at room temperature than irradiated at 563K, and their free volume was reduced by copper.

2) The model alloys without copper show similar hardening trends irrespective of their carbon or nickel content. Hardening is not so significant at the lower doses, and then getting greater with increasing dose. The dose dependence follows the form of $\Delta HV=k(dpa)^n$ where n is estimated to be within the range from 0.25 to 0.5. The recovery process by isochronal annealing is also similar among these alloys. Fine vacancy clusters and interstitial loops are possible matrix defects that

induce the hardening, however the vacancy clusters act as weak barriers against dislocation motion. Interstitial loops are dominant hardening features in the higher dose range.

Effects of copper

1) Copper content strongly affects the positron parameters, particularly trapping rate of positrons. This effect is attributed to formation of copper-vacancy complexes. Their formation occurs in the lower dose range and tends to saturate in the higher dose range. Since they do not induce significant surface hardening, they also act as relatively weak obstacles.

2) Copper addition clearly changes the hardening trends. The hardening of the model alloys containing copper shows greater hardening than the alloys without copper particularly at relatively low doses, and the hardening increases with increasing copper. Then hardening shows saturation tendency at higher doses, and the effect of copper content on hardening is not seen at the highest dose. Further hardening was observed by isochronal annealing for Fe-0.1C-0.4Cu, and the alloy did not show complete recovery even at high temperature at which other alloys show complete recovery. From these results, it is guessed that formation of copper clusters occurs during ion irradiation at 563K, and copper-vacancy complexes might act as the precursors of copper clusters. The copper clusters add nickel atoms at higher doses to show further growth and the resultant hardening.

The combination of positron annihilation, TEM and hardness measurement for model alloys irradiated with heavy ions suggests that the microstructural features that form during ion irradiation at 563K are vacancy clusters, interstitial loops, copper-vacancy complexes, and copper rich clusters. Their evolution processes can be basically expressed as the cluster equation. The ideal way to establish the mechanistic prediction is to solve the equation to estimate the size and number density of them under the interest

irradiation condition and material condition, and convert them to mechanical property change.

Formation of vacancy clusters is confirmed with positron annihilation experiment. The evolution process of vacancy clusters is highly affected by cascade-vacancy cluster formation and thermal emission of vacancies from a cluster. Both of them are not fully understood, therefore necessity and possibility of computer simulations and well-designed experiments are discussed for understanding and estimation of these necessary physical parameters.

Small dot images (~2nm) observed with TEM are believed to be interstitial loops in this experiment as well as in other studies on simple iron alloys irradiated with neutron or ions. The loops are thought to be the dominant hardening features at the higher doses for the model alloys. However there is no example that observes dislocation loops in irradiated complex RPV steels, maybe due to resolution limit of TEM. An extrapolation approach from simple alloy systems to complex steel systems are discussed for getting insight about interstitial loop evolution in practical steels.

Although no direct evidence of copper clustering is obtained in this study, copper affects hardening trends and positron parameters. Copper-vacancy complexes are thought to form according to the positron experiment, and it is possible for them to enhance the formation of copper rich clusters. Copper-vacancy cluster evolution expanded from vacancy cluster evolution is proposed and discussed.

Since there are many unknown parameters that affect the defect cluster evolution and the copper rich cluster evolution as well as uncertainty in barrier strengths and appropriate hardening superposition models, fully mechanistic prediction independent of data base limitation is currently impractical. However mechanistic understandings should be applied to the development of the empirical prediction methods with respect to abstraction of influential variables and determination of function forms from the mechanistic models. Well-designed experiments specific to the each problem are needed for further mechanistic understandings and evaluation of various physical parameters. The experimental methods attempted and discussed in this study can be expansively

applied to the specific experiments, and will contribute to establishing more mechanistic prediction methods.

Acknowledgments

At first the author wishes to thank Prof. Iwata, Prof. Sekimura and Prof. Ishino for their great instruction over a period of five years. I also thank Mr. Arai for his taking care of the overall experiments. I wish to appreciate all of the following cooperation. The specimen preparation was helped by Mr. Arai, Mr. Moroyama, Mr. Sato and Japan Steel Works Co. The ion irradiation experiments were helped by HIT staffs: Prof. Tagawa, Prof. Shibata, Mr. Narui, and Mr. Omata. Dr. Tsukamoto helped me when the irradiation chamber was out of order. The positron beam experiments were carried out by the group of Tsukuba University: Prof. Tanigawa, Dr. Uedono and Dr. Wei. Dr. Kawanishi instructed the author how to use TEM. Dr. Morishita and Dr. Kaneta instructed me how to use a work station. Mr. Kato, Mr. Masumura, Mr. Yanagisawa, and Mr. Yonamine collaborated with the author through their graduation works. Mr. Kato and Mr. Yonamine carried out the hardness measurement and the TEM observation with the author by the help of Dr. Kawanishi. Mr. Masumura analyzed the positron beam results. Mr. Yanagisawa helped the ion irradiation experiments and the attempt of low temperature ion irradiation followed by resistivity measurement.

I also thank other colleagues of the laboratory for their fruitful discussion, and the secretaries for their taking care of the official procedures. The author appreciates Prof. Odette, Prof. Lucas and their students for their kind care of me when I stayed at University of California at Santa Barbara.

This work is supported by Grant-in-Aid for Scientific Research from Monbusho (Ministry of Education, Science and Culture) and Research Fellowships of the Japan Society for the Promotion of Science for Young Scientists. The scholarship of the Nihon Ikuei Kai greatly supported my student life, too. The author is so thankful for the great supports.

Finally, I wish to thank all the people who have supported me in any aspects again.

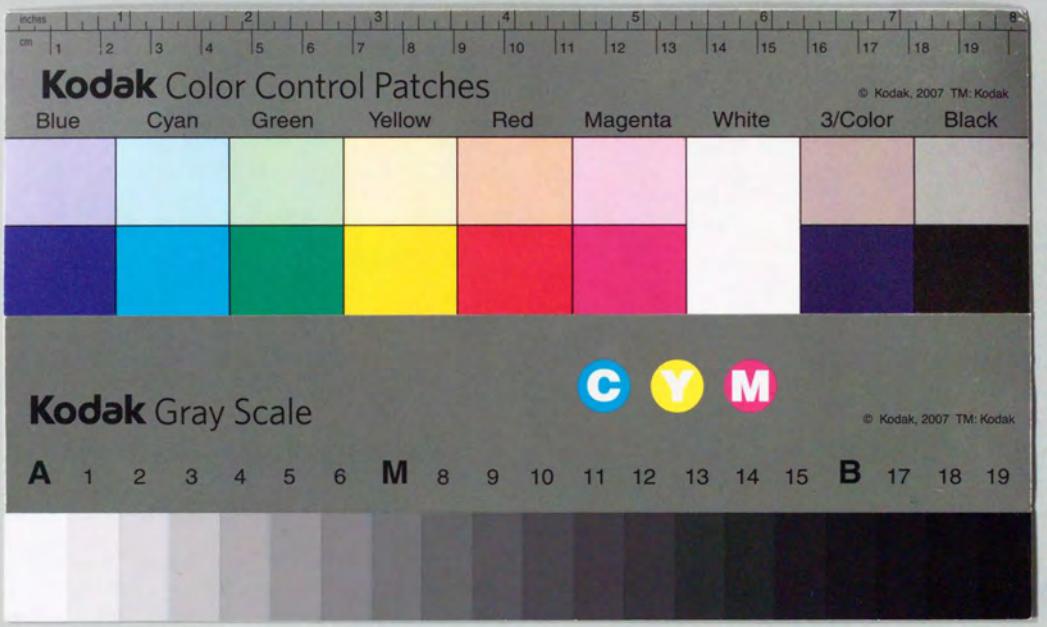
inches
cm
Kodak Color Control Patches
© Kodak, 2007 TM: Kodak
Blue
Cyan
Green
Yellow
Red
Magenta
White
3/Color
Black
Kodak Gray Scale
C
Y
M
© Kodak, 2007 TM: Kodak
A 1 2 3 4 5 6 M 8 9 10 11 12 13 14 15 B 17 18 19